Rare event searches with CUORE style TeO_2 bolometers

by

Nicholas Ivan Chott

Bachelor of Science
Illinois State University 2008

Submitted in Partial Fulfillment of the Requirements

for the Degree of Doctor of Philosophy in

Physics

College of Arts and Sciences

University of South Carolina

2016

Accepted by:

Frank T. Avignone III, Major Professor

Richard J. Creswick, Chair, Examining Committee

Jeffery Wilson, Committee Member

Paolo Gorla, Committee Member

Cheryl L. Addy, Vice Provost and Dean of the Graduate School

Dedication

To my family...

Acknowledgments

I would like to thank the many people that I have had the pleasure to work with over the course of my time in graduate school. First and foremost I would like to thank Dr. Avignone for inviting me to join his research group and giving me the opportunity to be a part of the CUORE collaboration. Frank always seems to see the best in people and I am grateful that he took the time to advise me throughout my PhD. He is understanding, encouraging, intelligent and full of experience, has an extremely good work ethic but knows how to enjoy life. He truly is am amazing person. I would also like to thank my committee members from the department, Dr. Creswick and Dr. Wilson, and also my external committee member, Dr. Gorla, for their continual support and guidance. To my friends at the University of South Carolina, at LNGS, and throughout the CUORE collaboration: Dawei, Jason, Chris, Rasha, Camilo, Travis, Gary, Clint, Nick, Rahman, Kevin, Johnny, Seth, Luigi, Salvatore, Carlo, Stefano, Luca, Claudia, Luca, Daria, Lucio, Laura, Margherita, Carmine, Juan Carlos, Chiara, Kyunguen, Jeremy, Sachi, Alexey, Tom and Tommy (and anyone I am forgetting), thank you! A special thanks to Luigi and Tommy for all their help onsite. And last but not least thank you to my family, without you support and encouragement over the years I would have never made it to this point.

Abstract

In this dissertation we report on the first search for solar axions from atomic transitions in the solar core. A search for the 14.4 keV axion from the ground state transition in ^{57}Fe in the sun was also performed, via the axioelectric effect in TeO_2 bolometers, in the CUORE-0 experiment. Both axion searches are performed in the scope of the DSFZ invisible axion model. An upper bound on the axion-electron coupling constant of $g_{ae} \leq 3.1 \times 10^{-11}$ (95% CL) is obtained with 62.7 $kg \cdot days$ of TeO_2 exposure from the CUORICINO experiment. The CUORE-0 data results in a upper bound on the product of the axion-electro and effective axion-nucleon of $|g_{ae} \times g_{aN}^{eff}| \leq 1.33 \times 10^{-17}$ (95% CL). Data from CUORE-0 was also used to place a bound on the half live for zero and two neutrino double beta decay of ^{130}Te. For CUORE-0 the zero neutrino double beta decay half life bound is $T_{\beta\beta}^{0\nu}$ (^{130}Te) $> 2.7 \times 10^{24}$ yr. When combined with the data from the earlier CUORICINO experiment the bound is $T_{\beta\beta}^{0\nu}$ (^{130}Te) $> 4.0 \times 10^{24}$ yr. The two neutrino double beta decay half life of CUORE-0 was measured to be $T_{\beta\beta}^{2\nu}$ (^{130}Te) $= 8.2 \pm 0.2$ (stat.) $\pm$ 0.6 (syst.) $\times 10^{20}$ yr.

Table of Contents

List of Tables

List of Figures

Chapter 1

Neutrino physics

1.1 The Standard Model

The Standard Model of particle physics is the best and most complete set of theories to describe particle interactions from three of the four fundamental forces. These forces are the electromagnetic, strong and the weak forces. The theory of Gravity has not yet found its way into the standard model but that is not for lack of effort. The Standard Model is composed of 17 known particles, including the newly discovered Higgs boson; it is divided into three types of particles: quarks, leptons, and bosons. A table of the current Standard Model of particle physics is shown in figure 1.1.

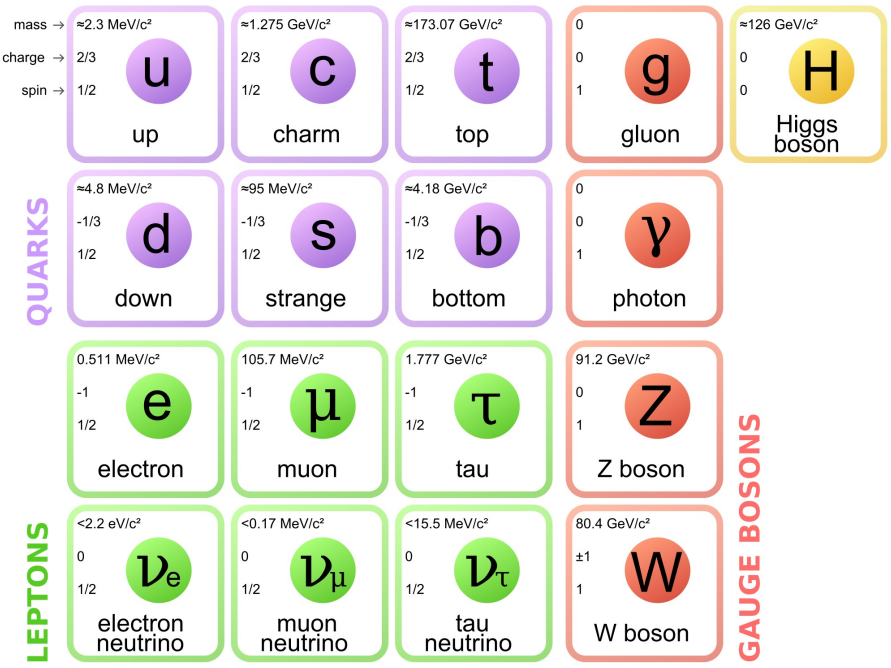

Figure 1.1: The current Standard Model of elementary particles [116].

Of the 17 fundamental particles in the Standard Model, 12 are fermions (spin $\frac{1}{2}\hbar$) and 5 are bosons (spin $1\hbar$). Fermions constitute all of the normal matter in the universe and are made up of two subgroups called quarks and leptons. Fermions are grouped into three generations of matter, as shown in the first three columns of figure 1.1. Each generation of matter has an "up"-type quark, a "down"-type quark, an electrically neutral neutrino, and a charged particle analogous to the electron. The three generations of matter share the same types of particles; the mass of each family of particles increases with each generation of matter. The neutrino's flavor in each generation is denoted by the subscript, which corresponds to the charged lepton in the same generation. In the first generation of matter, the charged lepton is the electron, so the corresponding first generation neutrino is the electron neutrino. The second and third generations contain the muon and tau neutrino respectively. Fermions belonging to the first generation are by far the most common types of matter, while the second and third generations make up the more exotic (short lived) particles. The gauge bosons are the interaction particles or force carriers for the electromagnetic, strong, and weak nuclear forces. The photon is the force carrier for electrodynamics, the gluon that of the strong force, and the remaining two (Z^0 and $W^{\pm}$) are the force carriers of the weak interaction.

In figure 1.1, the mass of each particle is given along with the electric charge and spin. It should be pointed out that in the case of the three neutrino flavors only upper bounds on the masses are given. Neutrino properties are still not completely understood and for that reason there are several dedicated experiments with the aim of further increasing our knowledge of neutrinos. The Standard Model is our best theory of how particles interact but it is not without its flaws; originally it predicted that neutrinos have no mass. Due to observed oscillations between flavor states, which requires neutrinos to have mass, today it is known that at least two of the three neutrinos have a non-zero mass. Evidence for solar neutrino oscillations dates back to

the 1960s with Ray Davis (Homestake experiment) [51] and to two additional chemical experiments; SAGE [3] and GALLEX [20] in the late 1980s. In 2001 the Sudbury Neutrino Observatory (SNO) [6] demonstrated that all the predicted ^8B neutrinos did arrive from the sun, but some oscillated to other flavors. Finally KAMLAND [59] showed that the large mixing angle solution was strongly favored. The existence of atmospheric neutrino oscillations was discovered by Super-Kamiokande in 1998 [67].

In addition, Quantum Chromodynamics (QCD), the part of the Standard Model that describes the theory of strong interactions, also has an issue called the Strong CP problem. The short explanation is that QCD predicts a value for the neutron electric dipole moment (NEDM), many orders of magnitude ($\sim 10^{10}$) larger than the current experimental bound. The strong CP problem will be discussed in chapter 4. However to its credit, the Standard Model is an amazing theory, correctly describing physical processes over several orders of magnitude. It even predicted close to half (seven) of the 16 particles prior to their discovery: charm, top, bottom, ν_τ, the gluon, Z^0, and $W^\pm$. Despite a few known issues the Standard Model is a robust and well established theory, and any modifications to this theory will not require massive changes.

1.2 Beta decay

Of all the types of radioactivity, beta decay is the most common. There are two ways one can think about beta decay; at the nucleon level (protons and neutrons) and the more fundamental quark level. The nucleon level is the easier to explain of the two and the quark level includes a more in-depth explanation using elementary particles from the Standard Model. Figure 1.2 is color coded to show the type of radioactive decay for various isotopes. The number of neutrons is plotted as a function of the number of protons. Beta decay is observed in isotopes of almost every element, excluding heavy nuclei. The orange regions denote β^+ decay and the blue regions denote β^- decay.

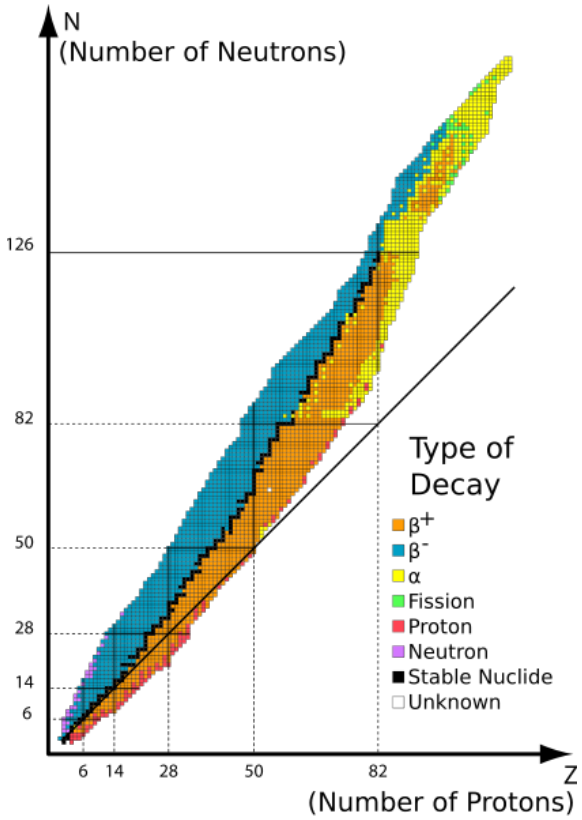

Figure 1.2: Type of radioactive decay for various isotopes [44].

At the nucleon level, beta decay is the decay of neutron into a proton or vice versa. For beta minus decay, the neutron decays into a proton, which changes the atomic number, and emits an electron and an electron-antineutrino ($(A, Z) \rightarrow (A, Z+1) + e^- + \bar{\nu}$). The mass of a neutron is 939.565378 MeV/c^2, and the mass of a proton is 938.272046 MeV/c^2. Since the neutron mass is larger by $\sim$ 1.3 MeV/c^2, it requires no additional energy to decay to a proton (beta minus decay). The electron and the anti-neutrino are necessary to ensure that electrical charge, baryon number, and lepton number are conserved throughout the reaction. On the left-hand side (LHS) of the reaction there is only a neutron, an electrically neutral baryon, of baryon 'charge' +1, and no lepton charge. Therefore the right-hand side (RHS) of the equation must have a total electrical charge of 0, a baryon number of +1, and lepton number of 0. On the RHS there is a proton, electron and anti-electron neutrino. The proton is a

baryon (+1) and has electrical charge +1. There must be an additional particle of negative electrical charge to sum to a net electrical charge of zero; the electron. If the electron was the only additional particle the electrical charge would be conserved but the presence of the electron gives the RHS a lepton number of +1, while the LHS has a lepton number of 0. This means that there needs to be a third particle with lepton number of -1 (an anti-particle) and neutral electrical charge. The neutrino is the only lepton with a neutral charge, so the third particle must be a anti-electron neutrino to get the total lepton number on the RHS to equal zero.

The reverse case (beta plus decay) where a proton decays into a neutron, positron, and electron neutrino is also possible ($(A, Z) \rightarrow (A, Z-1) + e^+ + \nu$). However additional energy is required due to the difference in (rest) mass between the neutron and the proton. In general, any reaction can be rearranged as long as the reaction is energetically possible and charge is conserved. A particle on one side can be move over to the other side of the reaction and replaced with its anti-particle. It should be noted that "beta decay" is a bit ambiguous as to which process is being referred to. From here on, we will use beta decay to refer to the process in which an electron is emitted unless otherwise noted by a $\pm$ to indicate the charge of the emitted beta particle (e^+/e^-). In addition to beta decay, another process that unstable atoms can use to become more stable is electron capture (EC). During electron capture, an electron in an atom's inner shell is drawn into the nucleus where it combines with a proton, forming a neutron and a neutrino; an electron neutrino is ejected from the nucleus.

As mentioned above, the quark level of beta decay is the true process as it involves only elementary particles. Nucleons, protons and neutrons, are composite particles made up quarks and gluons and described by three valence quarks. Protons and neutrons are combinations of the lightest quarks from the first generation of matter, the up and the down quark. The up quark has an electrical charge of +2/3 while

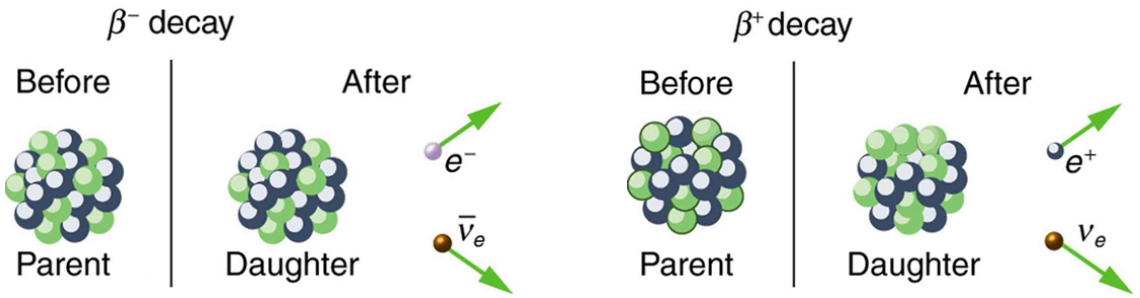

(a) (b)

Figure 1.3: Diagrams of (a) beta minus and (b) beta plus decay at the nucleon level [94].

the the down quark has a charge of -1/3. The quark charge is fractional, mainly for historical reasons, as the electron was discovered first and thought to be the smallest amount of charge. It is the smallest amount of free charge so fractional charge is not an issue. By considering charge units, it is easy to see that the neutron is composed of two down quarks and an up quark for a net charge of zero, and that a proton is two up quarks and a down quark for a net charge of +1.

One should notice that the sum of the masses of the quarks is only a fraction of the (rest) mass of the proton and neutron ($\sim$ 1 GeV). Much of the remaining mass comes from the gluons of the strong force holding the quarks together. Beta decay (β^-) occurs when a down-quark decays into an up-quark; the process is mediated by the W^- vector boson. W^- is very short lived and heavy, with half-life of $\sim$ 3x10^{-5} s, and decays into an electron and electron anti-neutrino. In the case of β^+ decay, W^+ is the mediator.

1.3 The discovery of the neutrino

Historically, beta decay was thought to be a two body problem, with the decay of a neutron into a proton and the emission of an electron ($(A, Z) \rightarrow (A, Z + 1) + e^-$). Only the energy of the emitted electron (and recoil of the nucleus) can be measured directly, as the neutrino is electrically neutral and only interacts via the weak force.

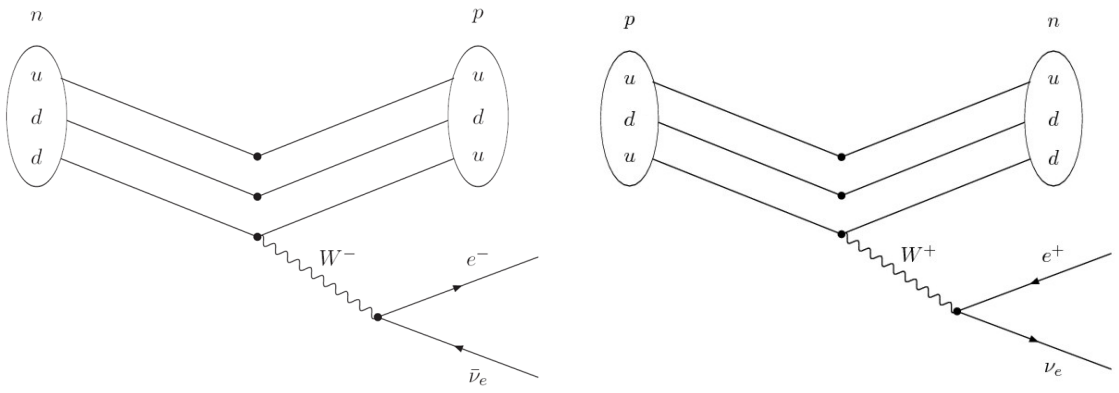

(a) β^- decay (b) β^+ decay

Figure 1.4: Feynman diagrams for (a) beta minus and (b) beta plus decay [45].

At first there was no reason to postulate an additional "invisible" particle. And for this reason it came as a surprise that the measured electron energy spectrum was a continuum rather than the expected mono-energetic value, with the spectrum dropping to zero just before the expected electron energy. The continuous beta spectrum was confirmed by L. Meitner and W. Orthmann in 1930 [89]. Furthermore, the expected spin did not match the theory. Beta decay appeared to violate the tried and true theory of conservation of energy, momentum, and angular momentum.

In 1930, in an attempt to rectify the conservation of energy and momentum, Pauli suggested a possible three body decay rather than the assumed two body decay. This new particle would have to be electrically neutral, with a spin $\frac{1}{2}$ $\hbar$, and have little to no mass. Knowing that this would be very difficult to verify experimentally, Pauli was famously quoted as saying "I have done a terrible thing. I have postulated a particle that cannot be detected." While there were many indirect proofs for the existence of an additional particle, and despite the success of Fermi's theory of nuclear beta decay, the neutrino had not yet been confirmed directly. Over a quarter of a century passed before the first experimental observation of the neutrino by Fredrick Reines and Clyde Cowan in 1956 at the South Carolina Savannah River P-Reactor [48, 49]

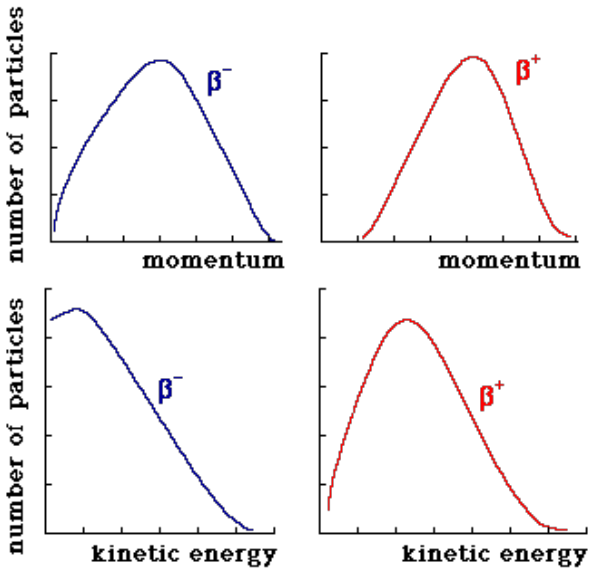

Figure 1.5: Continuous momentum and kinetic energy spectra of emitted beta particles (electron and positron) [114].

Reines and Cowan were able to directly detect the electron anti-neutrino through inverse beta decay ($\bar{\nu}_e + p \rightarrow n + e^+$). The emitted positron quickly finds an electron from a nearby atom and annihilates, which results is two detectable ~ 511 keV photons emitted back to back ($e^+ + e^- \rightarrow \gamma + \gamma$). Shortly after ($\sim 5$ μs) the electron-positron annihilation, the remaining neutron is captured by a cadmium atom and emits a gamma ray ($n + {}^{108}Cd \rightarrow {}^{109*}Cd \rightarrow {}^{109}Cd + \gamma$). The coincidence of the pair annihilation and neutron capture provides a unique signature for inverse beta decay. Reines and Cowan relied on the large flux of anti-neutrinos from the Savannah River P-Reactor. The detector was placed a distance of 11 m from the reactor, and 12 m underground to better shield it from cosmic rays; high energy charged particles consisting of mainly muons, but also electrons and even neutrons. The neutrino flux from the reactor was calculated to be approximately 10^{13} cm^{-2} s^{-1} at the location of the detector.

A diagram of the Reines and Cowan experimental setup is shown in figure 1.6. It consisted of three large tanks of organic scintillator (I, II, and III) with fifty-five 5-inch photomultiplier tubes (PMTs) mounted to each end of each tank. Sandwiched

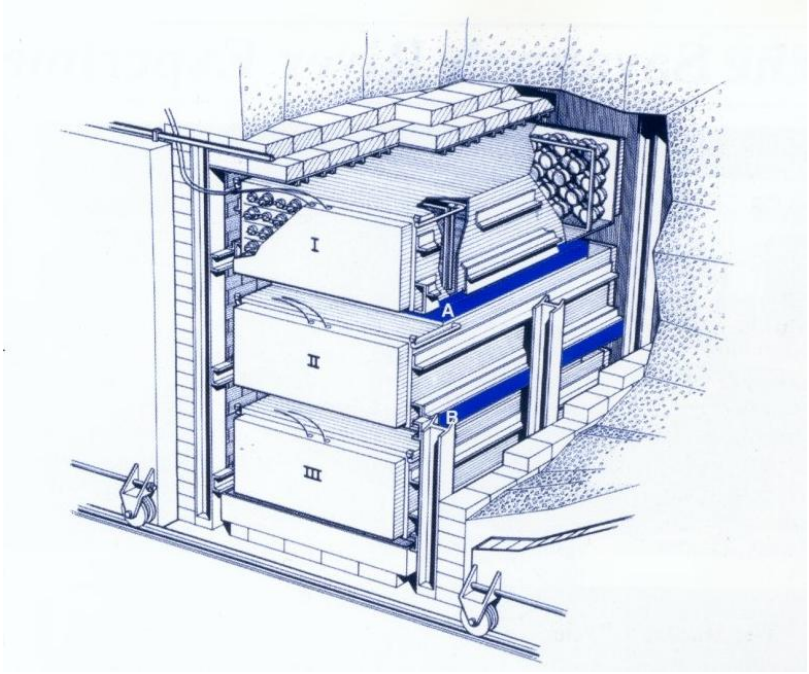

Figure 1.6: A diagram of the experimental setup for the Cowan and Reines Savannah River Experiment [95].

between these scintillators were two additional tanks (A and B), which contained water and dissolved cadmium chloride ($CdCl_2$), to served as the target for the expected reaction of inverse beta decay; where a neutrino interacted with a hydrogen nucleus. In total these tanks contained approximately 200 L of water and roughly 40 kg of $CdCl_2$. Since cadmium is a strong neutron absorber (used in control rods of nuclear reactors) it was added to the water to promote neutron capture; resulting in a detectable number of coincidence γ-rays. Following the 1956 experiment, a number of other neutrino experiments were performed by Reines' group.

1.4 Double beta decay

Double beta decay (DBD) is a rare spontaneous nuclear transition in which the nuclear charge changes by two units while the mass number remains constant. It was long recognized as valuable tool to study lepton conservation in general and neutrino properties specifically. A paper titled "Double Beta-Disintegration" [72] was pub-

lished in 1935 by M. Goppert-Mayer. Soon after, in 1937, E. Majorana proposed that the neutrino may be indistinguishable from the anti-neutrino [88]. In 1939, Wendell Furry suggested that double beta decay could be used to test Majorana's theory [68]. The observation of neutrino-less DBD would immediately establish that the neutrino is it's own antiparticle and that total lepton number is not a conserved quantity.

Only when (single) beta decay is energetically forbidden, or requires a large change in momentum, can double beta decay be observed. The initial nucleus must be less bound than the final nucleus, while the intermediate nucleus must be even less bound than the initial nucleus so it is energetically unfavorable. That is not to say that $\beta\beta$-decay cannot occur in nuclei that do not meet these requirements. However one would not expect to observe $\beta\beta$-decay in such an isotope experimentally as the signal would be overwhelmed by first order processes. Luckily these conditions are met naturally in a number of nuclei. The natural suppression of beta decay occurs in some elements, with an even mass number, A, due to the "pairing" interaction as described in the semi-empirical mass formula. Figure 1.7 is a generic mass parabola for an isobaric nuclei isobaric nuclei with an odd mass number and an even mass number, respectively. The pairing term, which differs for nuclei with an even-even number of neutrons and protons and an odd-odd number of neutrons and protons, naturally sets up conditions where either $\beta^-\beta^-$-decay or $\beta^+\beta^+$-decay is the energetically preferred decay mode.

$$m = Z \cdot m_p + N \cdot m_n - \frac{E_B}{c^2} \tag{1.1}$$

The mass of the bound nucleus (and atom in general when neglecting the mass of the electron) is the sum of protons and neutrons minus binding energy. The binding energy is a function of mass number and proton number; it includes a volume term, surface term, Coloumb term, asymmetry term and a pairing term.

$$E_B = a_V \cdot A - a_S \cdot A^{2/3} - a_C \frac{(A-2Z)^2}{A} + \delta(A,Z) \tag{1.2}$$

$$\delta(A,Z) = \begin{cases} +\delta_0, & \text{Z, N even (A even)} \\ 0, & \text{A odd} \\ -\delta_0, & \text{Z, N odd (A even)} \end{cases} \tag{1.3}$$

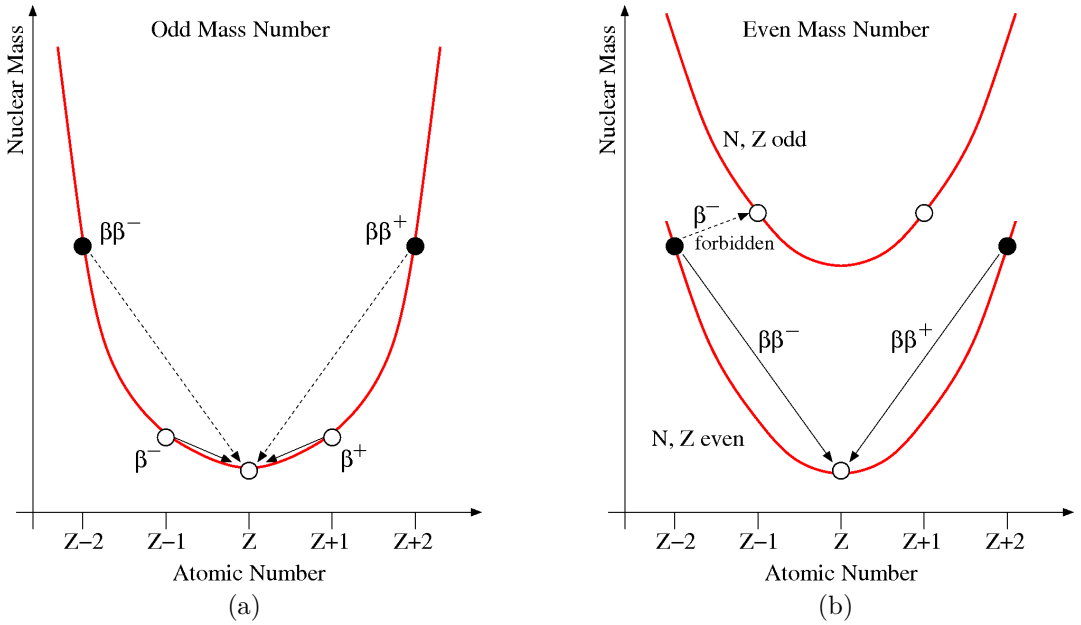

Figure 1.7: Generic mass parabola for isobaric nuclei with (a) an odd mass number and (b) an even mass number.

Two neutrino double beta ($2\nu\beta\beta$) decay is allowed by the Standard Model and has been observed experimentally in a number of isotopes. Table 1.1 gives the isotopic abundance and Q-value of various decay reactions double beta decay candidate isotopes. In theory it is possible to observe two neutrino double beta decay in over 60 isotopes. All $\beta\beta$-decay candidate nuclei are even-even and the process is not observed for a nucleus with an odd number of protons or neutrons. As this is the lepton number conserving mode of $\beta\beta$-decay, it involves the simultaneous emission of 2β particles and two anti-neutrinos. It is extremely rare, occurring among isobaric nuclei, with half-lives on the order of $\tau_{1/2} \sim 10^{18} - 10^{22}$ years. The extremely long lifetime of $\beta\beta$-decay makes experimental detection challenging. This process imposes

no requirements on neutrino properties and there are several decay modes possible as shown in equation 1.4.

$$\begin{aligned}
(A,Z) &\rightarrow (A,Z+2) + 2e^- + 2\bar{\nu}_e \qquad (\beta\beta^-) \\
(A,Z) &\rightarrow (A,Z-2) + 2e^+ + 2\nu_e \qquad (\beta\beta^+) \\
(A,Z) + 2e^- &\rightarrow (A,Z-2) + 2\nu_e \qquad (ECEC) \\
(A,Z) + e- &\rightarrow (A,Z-2) + e^+ + 2\nu_e \qquad (EC\beta^+)
\end{aligned} \tag{1.4}$$

Table 1.1: Isotopic abundance and Q-value of various double beta decay candidate isotopes.

$\beta\beta$ Decay Reaction	Isotopic Abundance [atomic %]	Q-value [keV]
^{48}Ca$\rightarrow^{48}$Ti	0.2	4274
^{76}Ge$\rightarrow^{76}$Se	7.6	2039
^{82}Se$\rightarrow^{82}$Kr	8.7	2996
^{96}Zr$\rightarrow^{96}$Mo	2.8	3348
^{100}Mo$\rightarrow^{100}$Ru	9.6	3034
^{116}Cd$\rightarrow^{116}$Sn	7.5	2814
^{124}Sn$\rightarrow^{124}$Te	5.8	2288
^{128}Te$\rightarrow^{128}$Xe	31.8	866
^{130}Te$\rightarrow^{130}$Xe	34.2	2528
^{136}Xe$\rightarrow^{136}$Ba	8.9	2458
^{150}Nd$\rightarrow^{150}$Sm	5.6	3368

Neutrinoless double beta decay, on the other hand, does impose some conditions on neutrino properties. It is not allowed in the standard model, as this process does not conserve lepton number (Δ L = 2). In addition it requires that neutrinos have a non-zero mass. This second constraint has to do with the handedness of the neutrino and anti-neutrino in nature. Neutrinos are left handed while anti-neutrinos are right handed. Handedness is defined by helicity, the projection of the spin onto the particle's momentum ($helicity \equiv \vec{S} \cdot \hat{p}$). If helicity is positive, the particle is said to be right-handed and if negative the particle is left-handed. Neutrino mass cannot be zero in order for $0\nu\beta\beta$ to occur, this is so the helicity of one $\bar{\nu}$ emitted can contain some component of opposite helicity and be absorbed as a ν. If the neutrino has

mass there exists a reference frame, obtained through a Lorentz boost, in which the helicity flips. Feynman diagrams for $0\nu\beta\beta$ and $2\nu\beta\beta$-decay are shown in figure 1.8.

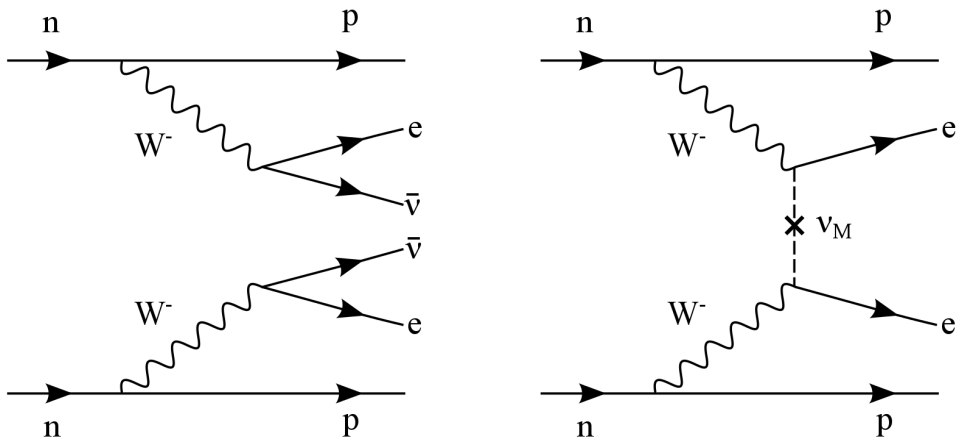

Figure 1.8: Feynman diagram of $2\nu\beta\beta$ decay and $0\nu\beta\beta$ decay [107].

1.5 Neutrino properties and neutrinoless double beta decay

There are three important questions pertaining to neutrino physics, and $0\nu\beta\beta$-decay experiments are positioned to play a unique role in addressing them. First, are neutrinos Majorana particles that differ from anti-neutrinos only by helicity? Second, what is the neutrino mass-scale? Third, is lepton number conservation violated? Neutrinoless double beta decay is a useful tool to study the properties of neutrinos, specifically to determine the nature of the neutrino and the measurement of the absolute mass scale. Detection of this rare nuclear process would confirm that the neutrino is its own anti-particle (Majorana), and measure or place a upper bound on the mass of the electron neutrino. In addition, lepton number violation would demonstrate physics beyond the standard model and could have impact on cosmology.

Single beta decay experiments and cosmological data both place constraints on the neutrino mass scale regardless of whether or not the the neutrino is a Dirac or Majorana particle. The Troitsk [42] and Mainz [86] ^{3}H (tritium) single beta decay experiments have placed an upper limit of 2.2 eV on the mass of the electron neutrino.

A scaled up ^{3}H experiment, currently in development, called the KATRIN experiment, is projected to have a sensitivity of 0.2 eV [58]. As for the importance of cosmological data; an upper limit on the sum of neutrino mass eigenvalues, $\Sigma \equiv m_1 + m_2 + m_3 \leq 0.75\ eV(90\%\ \text{CL})$, was derived by Barger el al. [39]. This limit was obtained using the data from the Sloan Digital Sky Survey (SDSS) [118], the 2-degree FieldGalaxy RedShift Survey (2dFGRS) [50] and the WMAP data [43].

The current picture of neutrinos, as implied by neutrino oscillation data, is that there are three neutrino flavors, connected to three neutrino mass eigenstates by a unitary transformation as shown in equation 1.5. Neutrino oscillations prove that at least two out of three neutrino flavors have a non-zero mass and that lepton flavor is not conserved. Flavor eigenstates are superpositions of the three neutrino mass eigenstates; analogous to the QCD quark mixing matrix.

$$|\nu_l\rangle = \sum_j^3 |U_{lj}^L| e^{i\delta_j} |\nu_i\rangle \tag{1.5}$$

In equation 1.5 the subscript l denotes the lepton flavor eigenstate ($l = e, \mu, \tau$) and the subscript j denotes mass eigenstate ($j = 1, 2, 3$). The factor $e^{i\delta_j}$ is a CP violating phase, taking the value ± 1 when CP is conserved. These transformations are written in matrix form as follows:

$$\begin{aligned} U &= \begin{pmatrix} U_{e1} & U_{e2} & U_{e3} \\ U_{\mu 1} & U_{\mu 2} & U_{\mu 3} \\ U_{\tau 1} & U_{\tau 2} & U_{\tau 3} \end{pmatrix} \\ &= \begin{pmatrix} c_{12}c_{13} & s_{12}c_{13} & s_{13}e^{-i\delta} \\ -s_{12}c_{23} - c_{12}s_{23}s_{13}e^{i\delta} & c_{12}c_{23} - s_{12}s_{23}s_{13}e^{i\delta} & s_{23}c_{13} \\ s_{12}s_{23} - c_{12}c_{23}s_{13}e^{i\delta} & -c_{12}s_{23} - s_{12}s_{23}s_{13}e^{i\delta} & s_{23}c_{13} \end{pmatrix}, \end{aligned} \tag{1.6}$$

where c_{ij} and s_{ij} are defined as the sine and cosine of the mixing angle between the two mass eigenstates denoted in the subscript (e.g. $c_{13} \equiv Cos(\theta_{13})$).

The rate of decay for the $0\nu\beta\beta$-decay mode, driven by the exchange of a massive Majorana neutrino, is approximated by:

$$(T^{0\nu}_{1/2})^{-1} = G^{0\nu}(E_0, Z) \left| \frac{m_{\beta\beta}}{m_e} \right|^2 \left| M^{0\nu}_f - (g_A/g_V)^2 M^{0\nu}_{GT} \right|^2, \tag{1.7}$$

where $G^{0\nu}$ is a phase space factor including couplings, m_e is the mass of an electron, and $m_{\beta\beta}$ is the effective Majorana mass of the electron neutrino. In equation 1.7, $M^{0\nu}_f$ and $M^{0\nu}_{GT}$ are the Fermi and Gamow-Teller nuclear matrix elements (NMEs), respectively, and g_A and g_V are the relative axial-vector and vector weak coupling constants, respectively. The phase space factor, NMEs, and coupling constants can be expressed as a single nuclear structure factor F_N defined as:

$$F_N = G^{0\nu} \left| M^{0\nu}_f - (g_A/g_V)^2 M^{0\nu}_{GT} \right|^2, \tag{1.8}$$

and equation 1.7 can be arranged to express the effective Majorana mass in terms of the half-life to become:

$$m_{\beta\beta} = \frac{m_e}{\sqrt{F_N T^{0\nu}_{1/2}}}. \tag{1.9}$$

After multiplication by a diagonal matrix of Majorana phases, $m_{\beta\beta}$ is expressed in terms of the first row (electron flavor row) of the 3×3 matrix of equation 1.5 as given by:

$$m_{\beta\beta} \equiv \left| \left(U^L_{e1}\right)^2 m_1 + \left(U^L_{e2}\right)^2 m_2 \cdot e^{i\phi_2} + \left(U^L_{e3}\right)^2 m_3 \cdot e^{i(\phi_3+\delta)} \right|, \tag{1.10}$$

where $e^{i\phi_2}$ and $e^{i\phi_3}$ are the Majorana CP phases. They take on the values ± 1 in the case that CP is conserved in the lepton sector.

Neutrino oscillation experiments have measured the mixing angles, which are directly related to the coefficients U^L_{lj} as shown in equation 1.6. Knowing the experimental values of these coefficients, one can express equation 1.10 solely in terms of the neutrino masses and the CP and Majorana phases. Precise oscillation parameter measurements are important, but there there are still two missing pieces to the

neutrino puzzle, namely understanding of the nature of the mass term (Dirac or Majorana) and the measurement of the absolute mass scale. Majorana phases do not appear in the neutrino oscillation expression and therefore have no bearing on this process; it is only the phase δ that affects neutrino oscillations. The information gained from solar and atmospheric neutrino experiments yields only the mass square differences $\delta^2_{ij} = \left|m^2_i - m^2_j\right|$; it cannot distinguish between the two mass patterns, or hierarchies, of the neutrino mass eigenstates. Solar neutrino experiments include SNO and SuperKamioande, while the reactor neutrino experiments include CHOOZ [21], Palo Verde [46], and KamLAND [22, 59, 60].

There are three possible hierarchies for neutrino masses: the quasi-degenerate, the inverted, and the normal hierarchy. The quasi-degenerate mass hierarchy scenario predicts that the three neutrino masses are all roughly the same compared to the absolute mass scale. The quasi-degenerate mass hierarchy is currently being investigated by current $\beta\beta$-decay experiments using different nuclei and varying techniques. Figure 1.9 shows the normal and inverted mass hierarchy. The normal hierarchy is the case in which $\delta^2_{solar} = m^2_2 - m^2_1$ and $m_1 \simeq m_2 << m_3$, while for the inverted hierarchy $\delta^2_{solar} = m^2_2 - m^2_1$ and $m_2 \simeq m_1 >> m3$. In both cases the approximation $\delta^2_{AT} \simeq m^2_3 - m^2_1$ is made. Oscillation experiments give only the difference of the squared mass eigenvalues. The inverted and normal hierarchies allow for ranges of effective Majorana mass of the electron neutrino of $\sim$ (10 - 50) meV and $\sim$ (0.1 - 5) meV respectively.

Three popular isotopes for $0\nu\beta\beta$ searches are ^{76}Ge, ^{130}Te, and ^{136}Xe. The most sensitive limits on $0\nu\beta\beta$-decay, until very recently, came from germanium experiments with detectors enriched with ^{76}Ge. The two notable experiments are the Heidleberg-Moscow experiment: $(T^{0\nu}_{1/2}(^{76}Ge) \geq 1.9\times10^{25}\text{y})$[41], and the IGEX $0\nu\beta\beta$-decay experiment: $(T^{0\nu}_{1/2}(^{76}Ge) \geq 1.6\times10^{25}\text{y})$[1]. These results imply that the upper bound on the effective Majorana mass of the electron neutrino, $m_{\beta\beta}$ ranges from $\sim$0.3 to $\sim$1.0 eV.

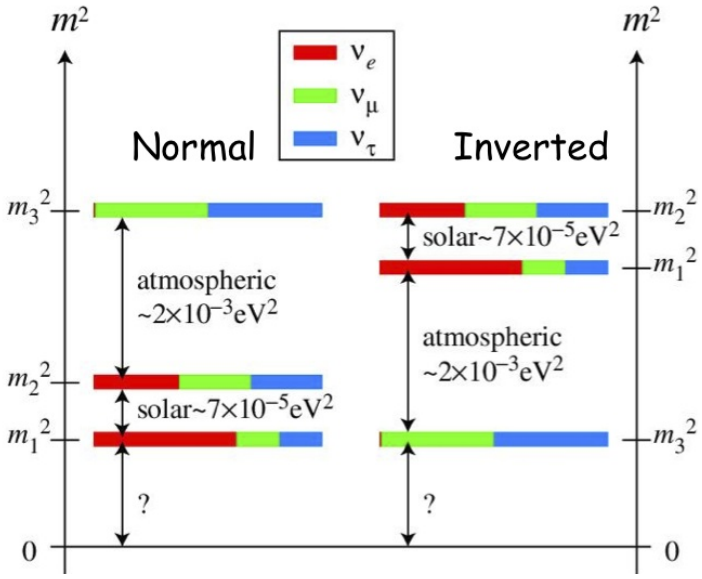

Figure 1.9: Normal and inverted neutrino mass hierarchy [121].

The effective mass depends on the choice of nuclear matrix elements used in the analysis. Figure 1.10 shows the spread in NME calculations for various $\beta\beta$-decay isotopes as they relate to the expected $0\nu\beta\beta$ half-life for neutrino of mass $m_{\beta\beta} = 50\ meV$. There was a claim of $0\nu\beta\beta$-decay by Klapdor-Kiengrothaus et al [81, 82, 83, 84], a subset of the Heidleberg-Moscow collaboration, but it has not been confirmed [2, 64, 122] and is very much open to debate. The most recent ^{76}Ge result from the GERDA collaboration: $T^{0\nu}_{1/2}(^{76}Ge) \geq 2.1 \times 10^{25}$y (90% CL), was combined with the data from IGEX and Heidelberg-Moscow data to obtain ($T^{0\nu}_{1/2}(^{76}Ge) \geq 3.0 \times 10^{25}$y) [5]. The xenon based $\beta\beta$-decay experiments, EXO-200: ($T^{0\nu}_{1/2}(^{136}Xe) \geq 1.6 \times 10^{25}$y)[7, 33] and KamLAND-Zen: ($T^{0\nu}_{1/2}(^{136}Xe) \geq 1.07 \times 10^{26}$y) [32, 69, 70], claim stronger bounds on the effective Majorana mass of the electron neutrino but, because of the large uncertainties in the nuclear mixing elements, it is difficult to compare results from different isotopes. The limits from EXO-200 imply that the effective Majorana mass of the electron neutrino $m_{\beta\beta}$ is less than 0.38-eV. In the case of Te detectors, the limit obtained from the combination of CUORICINO and CUORE-0 data on the $0\nu\beta\beta$-decay of ^{130}Te is $T^{0\nu}_{1/2}(^{130}Te) \geq 4.0 \times 10^{24}$ y [16].

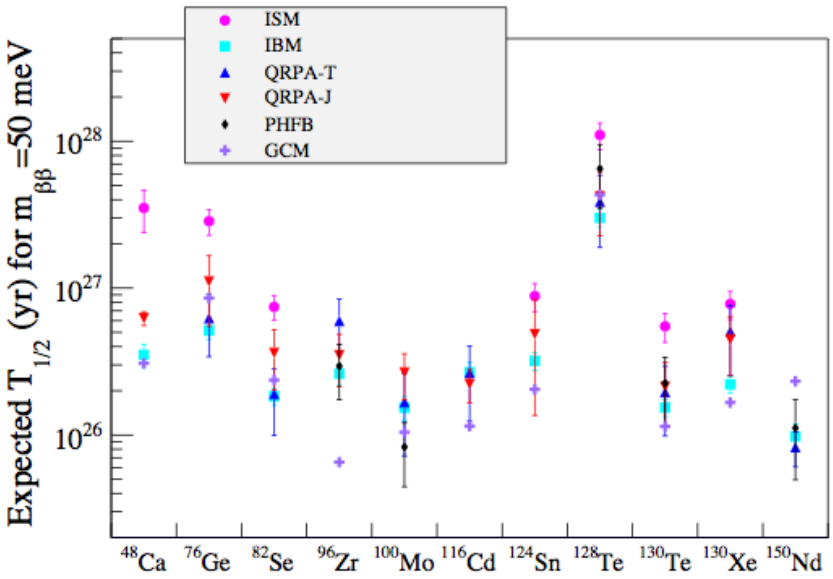

Figure 1.10: Expected $0\nu\beta\beta$ half-life for neutrino of mass $m_{\beta\beta} = 50\ meV$ for common DBD isotopes; several nuclear matrix element (NME) models are considered.

The CUORE experiment aims to probe the beginning of the inverted hierarchy using TeO_2 bolometric detectors. The TeO_2 bolometric technique was developed and studied over a long period of time and will play a crucial role in the next generation experiments. The CUORE detector was successfully installed and is currently in the (initial) phase of detector commissioning and is expected to begin taking data in early 2017. It will be the first $\beta\beta$-decay experiment at the $\sim$ 1 ton scale (741 kg of TeO_2). The expected sensitivity in neutrino mass is supposed to be better than $\sim$ 50 meV.

The previous single tower TeO_2 $\beta\beta$-decay experiment, CUORICINO, was built in 2003 and ran through 2008. It demonstrated the feasibility of CUORE and set, at the time, the best current limit for the neutrinoless double beta decay half-life in ^{130}Te. A final prototype of CUORE, CUORE-0 (a single CUORE tower) has just completed data taking at the Gran Sasso National Laboratory of INFN (Istituto Nazionale di Fisica Nucleare). This zeroth tower, hence the name, was built on the same tower assembly line and was operated as a standalone $0\nu\beta\beta$ decay experiment while CUORE was being built. The next generation experiment after CUORE, CUPID (CUORE

Using Particle IDentification), is projected to cover the inverted neutrino hierarchy mass region, and begin to probe the higher mass regions of the normal hierarchy.

The work reported in this dissertation has been performed in the framework of the CUORE (Cryogenic Underground Observatory for Rare Events) project, a tellurium dioxide array of 988 bolometers with the aim to search for neutrinoless double beta decay. In the last 6 years, significant time was spent onsite at LNGS; roughly 2-3 months each summer while taking classes then the better part of two years after passing the PhD qualifying exam. This included assisting with the assembly, instillation, and commissioning of CUORE-0, along with R&D for future projects. After being sent to LNGS full time, my research activity focused mainly on the construction and commissioning of the CUORE cryostat. At that time, CUORE-0 was taking data and CUORE was under construction. The plan was to help get CUORE running and then use the CUORE-0 data to search for interesting physics.

Chapter 2

Bolometers and the bolometric technique

2.1 Development of TeO_2 Bolometers

A bolometer is a low temperature detector that converts the energy of particle interactions into a measurable increase of the detector's baseline operating temperature. The idea to use large bolometric detectors for rare event physics, e.g. neutrinoless double beta ($0\nu\beta\beta$) decay searches, was first suggested by Fiorini and Niinikoski [65] in 1984. Ettore Fiorini and his group at the University of Milano Bicocca pioneered the bolometric technique; making considerable advancements in a short period of time. They started with single 73 g TeO_2 detector in 1992 [9]; first increasing in size to ∼340 g [10] and then successfully mounting them into a 4-detector array [11]. Building on the idea of a 4-detector array, literally and figuratively, the Mi-Beta experiment [98] was constructed; a five level array consisting of 20 TeO_2 detectors for a total mass of 6.8 kg. Following Mi-Beta, techniques for increasing the individual size of TeO_2 crystals were developed. The mass of individual crystals were more than doubled to 790 g with dimensions of 5×5×5 cm^3. These advancements in research and development culminated in 2003 with the CUORICINO experiment [17, 28], a 62 TeO_2 array with at total mass of 40.7 kg. It is impressive that in roughly a decade the detector mass achievable with TeO_2 bolometers had increased over two orders of magnitude, as seen in figure 2.1.

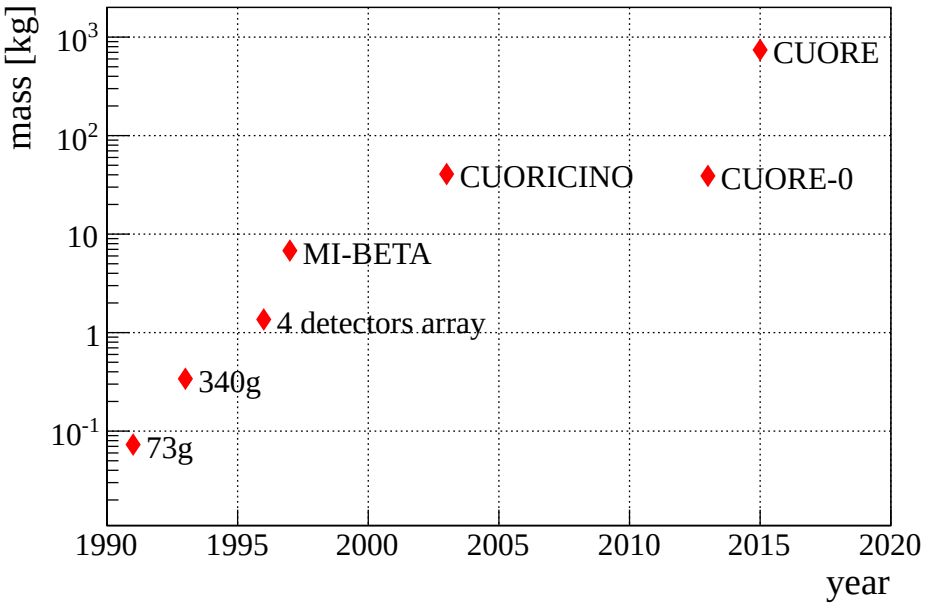

Figure 2.1: Advancements in TeO_2 detector mass over the last 25 years.

2.2 The bolometric technique

A bolometer is a thermal detector used to measure energy of particle interactions and acts like a calorimeter. This type of detector consists of two main components: the energy absorber and the sensor. The energy absorber, as the name implies, is the part of the detector where interaction energy is deposited. In general, the absorber has a heat capacity C and is connected to a heat sink, held at constant temperature T_0, through a weak thermal conductance G. A temperature sensor is attached directly to the crystal that converts the heat from phonon excitations from the deposited energy in the detector into an electrical signal. Figure 2.2 shows a sketch of a single TeO_2 crystal as well as a photo of a mounted CUORE bolometer, with important components labeled.

The bolometric technique relies on thermal physics of phonons (vibrational modes) in pure single crystals. When a particle interaction takes place inside the energy absorber athermal phonons (out of equilibrium) are produced. Athermal phonons

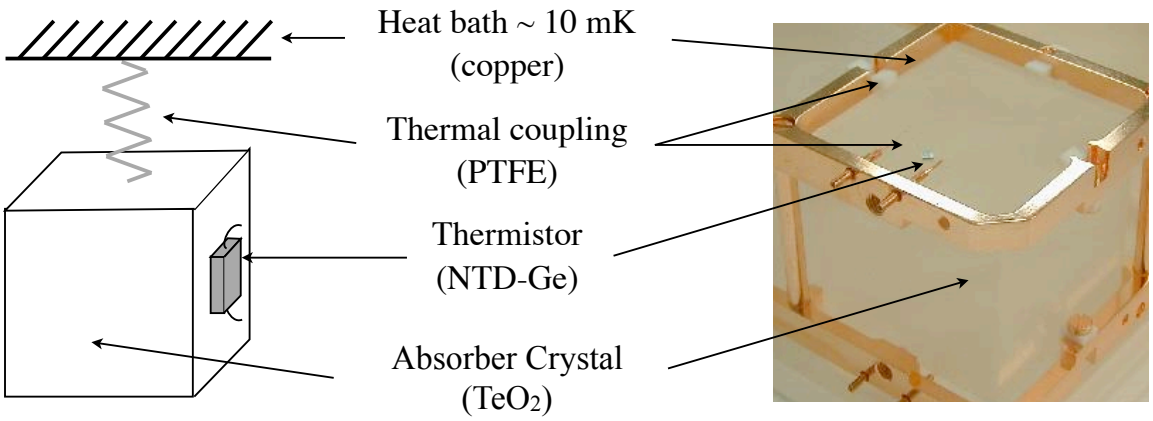

Figure 2.2: TeO_2 bolometer diagram (left) and picture (right) with components labeled.

interact and degrade in energy, eventually relaxing to a new equilibrium, resulting in an increase in the absorber's temperature. These degraded/relaxed phonons are called thermal phonons. As they are sensitive to phonons, bolometers can be broadly categorized as phonon mediated particle detectors (PMDs). There are two types of PMDs which are classified as fast or slow, depending on the response time of the thermal sensor. Fast detectors, have a response time on the order of microseconds and are sensitive to athermal phonons. If the phonon sensor response time is larger than the time needed for athermal phonons to thermalize (100s of milliseconds), the PMD is considered slow. Bolometers belong to the latter of the two PMD types and are therefore only sensitive to thermal phonons. The sensor simply takes the role of a thermometer and the bolometer works like a perfect calorimeter; losing no energy to undetectable channels.

Other low temperature detectors (which are not sensitive to phonons) rely on techniques like scintillation and ionization to measure energy deposition. However the measured energy through these channels is only a fraction of the total energy deposited in the absorber so the energy loss is high. Much of the energy deposited remains in the absorber, converted into phonon excitations, which are not detectable in ionization detectors, such as germanium detectors operated at ~80 K. This en-

ergy loss, together with the comparatively high-energy value necessary for an atomic excitation or ionization (the elementary detected event), increases the statistical fluctuations of the number of elementary excitations, thus making the intrinsic energy resolution of such detecting techniques poor [73]. Since bolometers measure phonon excitations, in addition to ionization, which results in phonons, these detectors have a low energy loss and excellent energy resolution.

Both the thermal signal amplitude and the signal decay constant depend on the heat capacity, C, of the absorber material. The temperature increase of the bolometer is given by $\Delta T = T - T_0 = \frac{E}{c_V(T)}$ the ratio of the energy E deposited, and the specific heat $c_V(T)$ of the absorber material. Of course, since the absorber is coupled to a heat sink, its temperature increase will decay exponentially with time. The time constant $\tau = \frac{C}{G}$ of the signal is given by the ratio of heat capacity C of the absorber and the thermal conductance G of the thermal link to the heat sink. The smaller the heat capacity, the larger the amplitude, and the faster the signal becomes. It is for this reason that bolometers are operated at very low temperatures, and dedicated cryogenic setups are required. The heat capacity contains all the contribution of the elements that comprise the detector; lattice heat capacity of the absorber and electronic and lattice heat capacity of the sensor. The heat capacity of the thermal conductance is considered to be negligible. When the difference between the absorber temperature and the heat sink is much less than the thermal bath, C and G can be treated as constants. Requiring that the absorber have a low heat capacity at its operating temperature was previously thought allow a wide range in absorber materials [73]. However producing absorbers, which means in most cases reproducibly growing crystals with the same properties, is easier said than done.

At low temperature ($T << T_D$) the specific heat of the absorber material follows the Debye model:

$$c_V(T) = \alpha \left(\frac{T}{T_D}\right)^3 + \gamma \left(\frac{T}{T_D}\right) \tag{2.1}$$

where T is the absorber temperature and T_D is the Debye temperature of the absorber material. The first term with a $\sim T^3$ dependence is due to lattice vibrations and the second term with the $\sim T$ dependence is due conduction electrons. In the case of CUORE bolometers, the absorber material is TeO_2, which is both a dielectric and diamagnetic material. Being a dielectric, the second term of equation 2.1 can be ignored and the absorber specific heat has only a $\sim T^3$ dependence. The fact that the absorber is diamagnetic means that there is no temperature dependence on the the magnetic susceptibility. Therefore the specific heat can be expressed as:

$$c_V(T) \propto \left(\frac{T}{T_D}\right)^3. \tag{2.2}$$

2.3 CUORE BOLOMETERS

A CUORE bolometer is a TeO_2 absorber, with a neutron transmutation doped (NTD) germanium thermistor coupled to it. CUORE bolometers are slow PMDs and are operated as calorimeters, allowing for energy deposited in the crystals to be sensed through measurable increases in temperature. The NTD measures the temperature rise of the TeO_2 crystal when energy is released in the absorber. The PTFE mounts hold the TeO_2 crystals in place, and act as a weak thermal couplings, with conductance G, between the crystals and the copper frame. The copper frame of the tower acts as both the support of the detectors and the thermal-heat bath maintained at a temperature of ∼10 mK. For a typical CUORE TeO_2 bolometer of mass 750 g, at a temperature of 10 mK, the time constant is on the order of one second. The heat capacity is roughly $C \approx 2 \times 10^{-9}\ J/K$, and the conductance is roughly $G \approx 2 \times 10^{-9}\ W/K$. For a deposited energy on the order of 1 MeV the temperature increase in on the order of 100 μK. A signal pulse of the voltage verses time is shown in figure 2.3.

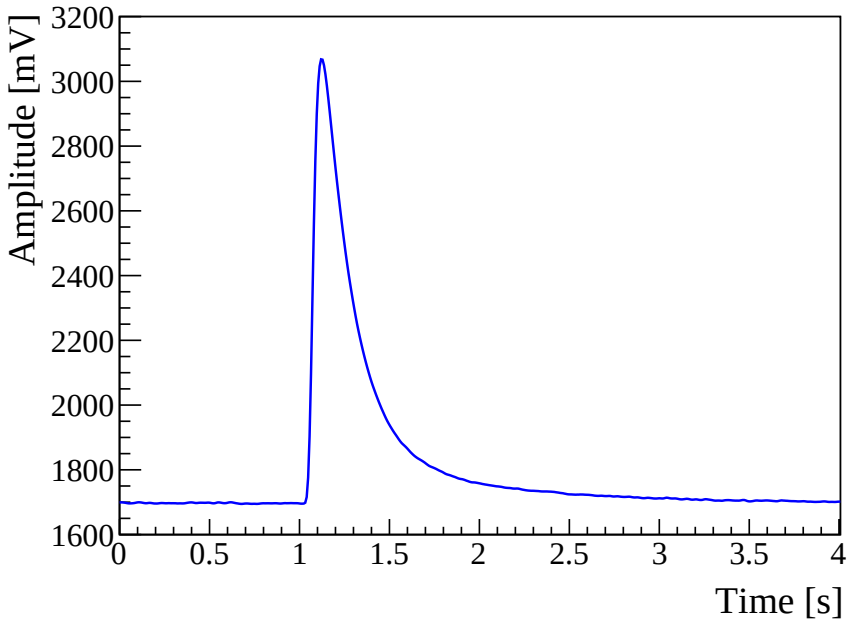

Figure 2.3: Signal for $\sim 1\ MeV$ deposited energy in CUORE TeO_2 bolometer.

The temperature is read out using a biased temperature sensor made from a Neutron Transmutation Doped Germanium (NTD-Ge) wafer. The energy heats up the bolometer which is coupled directly to the NTD thermistor. At very low temperatures the NTD resistance changes very dramatically, so that even small amounts of energy deposited change the resistance by a measurable amount. In the thermistor model, the resistance is a function of temperature given by eq 2.3:

$$R(T) = R_0\ exp\left(\sqrt{\frac{T_0}{T}}\right). \tag{2.3}$$

The NTDs are produced in batches and have similar characteristics. Common values for the NTD resistance at $T \approx 10\ mK$, where $T_0 \approx 3-4\ K$ and $R_0 \sim 0.9-1.2\ \Omega$, is $R \approx 100\ M\Omega$.

Using a biased temperature sensor the voltage read out can be directly related to the temperature, and therefore the energy deposited in the crystal. The thermal links which connect the absorber crystal to the copper frame are the PTFE (Teflon) supports and 25 μm diameter gold wire connecting the NTD to the wire strips, which

are also connected to the tower frame. The copper supports of each tower are coupled directly to the cryostat mixing chamber plate and are heat sinks for the deposited energy. As the absorber is weakly coupled thermally to the 10 mK heat bath, the temperature increases and therefore the voltage increases rapidly as the NTD and absorber are directly coupled, which then decays over the next few seconds back to the detector operating temperature of 10 mK. The time delay is due to the weak-thermal coupling. As the detector response time is very slow, the bolometric technique is not applicable when there are frequent events in each crystal; which would cause pile up in the detector.

CUORE-style bolometers are low temperature TeO_2 detectors in which the source and detector are one and the same. The absorber material, TeO_2, was chosen to exploit the "source = detector" technique to search for $0\nu\beta\beta$ decay in ^{130}Te. This technique ensures a high detector efficiency which is useful when searching for rare events. Tellurium is selected for both element specific and isotope specific reasons. Not only does it have (figure 2.4) a large natural abundance of the double beta decay isotope ^{130}Te ($\sim$34%) [63] with high $\beta\beta$-decay Q-value of 2527.518(13) keV [103, 106, 110], it also has a favorable nuclear factor of merit (figure 1.10). Having a large natural isotropic abundance (the largest in fact) means that, for the present generation DBD experiments, no enrichment is necessary. Enrichment is a costly process that is a necessity for all other candidate DBD nuclei. These reasons, along with the fact that large mass, high purity, and highly reproducible detectors can be made with TeO_2, makes tellurium a good choice when searching for $0\nu\beta\beta$ decay. As a side note, ^{128}Te has a large natural isotopic abundance as well, so natural tellurium is some what of a 2-for-1 DBD candidate, but ^{128}Te possesses a relatively low Q-value which makes ^{130}Te the preferred isotope of the two.

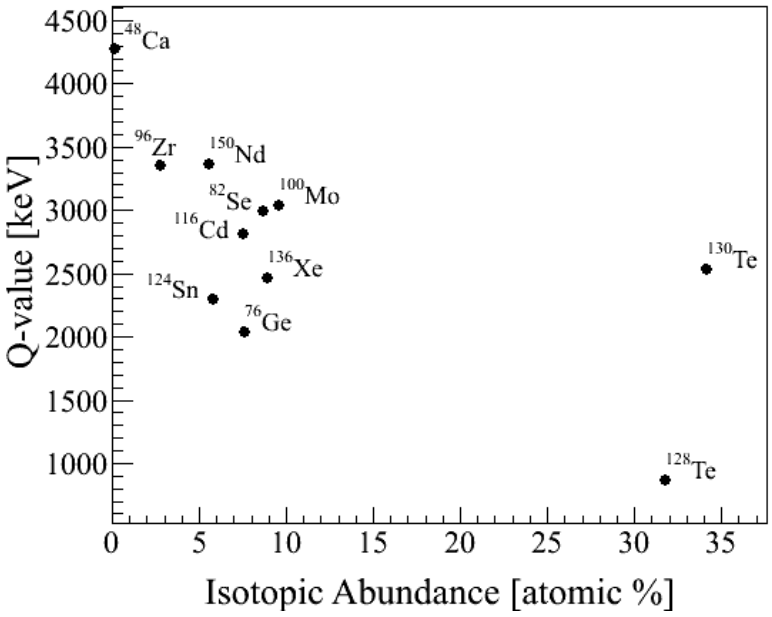

Figure 2.4: Expected Q-values for common $0\nu\beta\beta$ decay candidate isotopes versus isotopic abundance.

2.4 Going from CUORICINO to CUORE

The CUORICINO detector was a thirteen level modular array of 62 TeO_2 bolometers of varying size and levels of enrichment. There were 44 crystals with a mass of 790 g and dimensions of 5×5×5 cm^3, and 18 smaller crystals with a mass of 330 g and dimensions of 3×3×6 cm^3. The tower height was approximately 85 cm. The small crystals were repurposed Mi-DBD crystals whose surfaces had been lapped, so the masses were reduced. The larger crystals were all produced with natural tellurium and mounted in 11 modules of four crystals each. The smaller crystals were mounted in a three by three modular array of nine crystals each. Most of the smaller crystals (14) were made with natural tellurium, but of the remaining four, two were enriched in ^{128}Te to an isotopic abundance of 82.3% and two were enriched in ^{130}Te to an isotopic abundance of 75%. The total mass of ^{130}Te in the detector was 11.3 kg.

The CUORE experiment [23], or Cryogenic Underground Observatory for Rare Events, is the next step after the success of the CUORICINO experiment. It utilizes

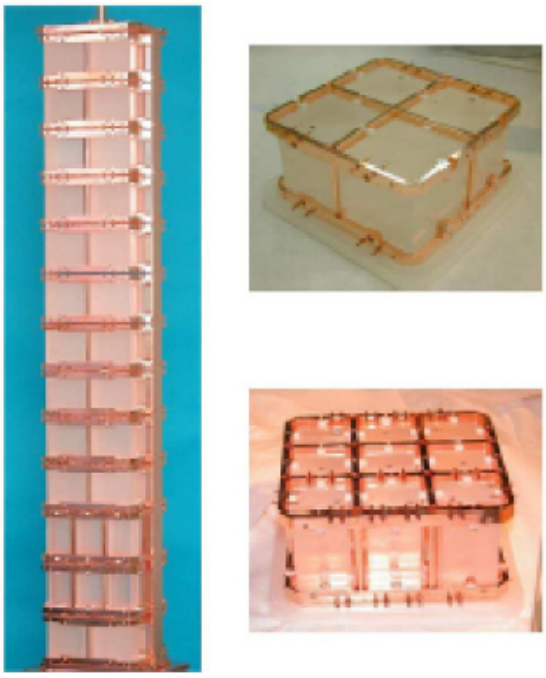

Figure 2.5: Photographs of the CUORICINO tower (left), a single plane of four $5\times5\times5$ cm^3 TeO_2 bolometers (upper right) and one plane of $3\times3\times6$ cm^3 bolometers [75].

multiple CUORICINO-sized towers to further increase detector mass by a factor of nineteen. A single CUORE tower will consist of 13 planes of the $5\times5\times5$ cm^3 bolometers. The geometry of the CUORE detector array is a tightly packed, approximately cylindrical, structure of 19 towers as seen in figure 2.6. There are 13 modules in each tower, consisting of four $5\times5\times5$ cm^3 TeO_2 crystals (750 g each). In total there are 988 crystals with a total mass of 741 kg of TeO_2 (206 kg of ^{130}Te). An entirely new building, the CUORE hut, was constructed to assemble and operate the detector. As a first step, and to demonstrate the feasibility of this ambitious project, a single CUORE tower named CUORE-0, was constructed according to the exact same procedure. This single tower contained 52, $5\times5\times5$ cm^3 TeO_2 crystals for a total mass of 11 kg of ^{130}Te. After assembly, CUORE-0 was transported from the CUORE hut to the adjacent CUORICINO hut and installed in the CUORICINO cryostat. Some some modifications were made to the cryostat to make it more CUORE-like.

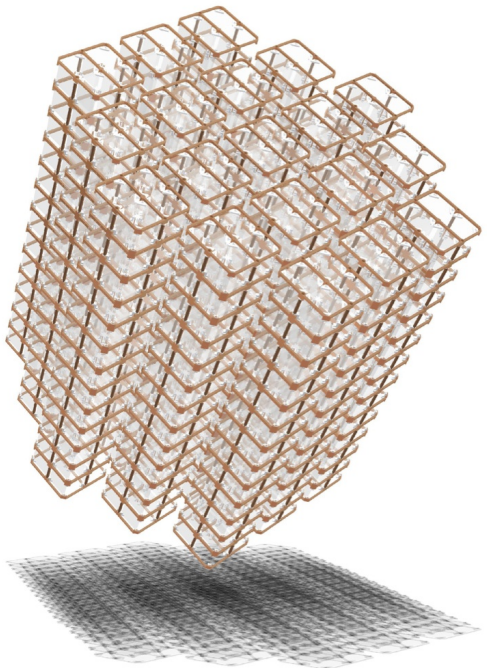

Figure 2.6: Artist rendering of the CUORE detector.

The experimental sensitivity to detect $0\nu\beta\beta$-decay as it relates to the experimental parameters is given by equation 2.4,

$$T^{0\nu}_{1/2} \propto a \cdot \epsilon \sqrt{\frac{M \cdot t}{b \cdot \Delta E}}, \qquad b \neq 0, \tag{2.4}$$

were ϵ is the detector efficiency, a is the isotopic abundance, M is the total active mass (in kg), t is the time in years, b is the background (counts/kg/keV/y) and ΔE is the energy resolution (keV) in the $0\nu\beta\beta$ decay region of interest (ROI). The parameters under the square root are crucial to the design of the CUORE experiment to maximize experimental sensitivity.

One way to increase experimental sensitivity is to build a larger detector to increase the number of ^{130}Te nuclei. The CUORE detector is 741 kg of TeO_2 (206 kg ^{130}Te). The dimensions of the experimental space required is 0.9 m in diameter and 1.385 m high. In order to contain such a large detector, a dedicated cryostat was constructed with the outermost (300 K) vessel 3.1 m high and 1.687 m in diameter. The cryostat is required to be powerful enough to cool down a large mass to a stable

temperature of 10 mK and account for the thermal radiation of the shields.

The background, especially in the $0\nu\beta\beta$ decay ROI, should be as low as possible. The CUORE target background is < 0.01 counts/keV/kg/year. Hall A of LNGS has an average depth of 3650 m.w.e with a μ flux of (2.85 $\pm$ 0.3) x 10^{-8} μ/s/cm^2, a neutron flux ($<$ 10 MeV) of 4x10^{-6} n/s/cm^2 and a γ-ray flux ($<$ 3 meV): of 0.73 γ/s/cm^2. In addition to operating CUORE underground, a strict selection of low-radioactive materials is used for cryostat construction. To protect the detector from radioactive contamination of materials within the cryostat that cannot be excluded, $\sim$10 tons of lead shielding (Lead + Copper OFE supports) are contained inside the cryogenic space and maintained at temperatures of 4 K or less.

Detector-energy resolution is crucial in order to see the 0ν peak over the 2ν continuum. Bolometers have very good energy resolution of $\sim$5 keV FWHM at the ^{208}Tl peak (2615 keV) [31]. This peak is less than 100 keV away from the $0\nu\beta\beta$ decay Q value of ^{130}Te ($\sim$2527 keV). In order to maintain this energy resolution in CUORE, the cryostat will need to have a stable operating temperature of 10 mK to ensure optimal performance of the TeO_2 crystals and the NTDs. In addition, NTDs have a very high impedance so the level of vibrations transmitted to the detector must be on the order of the energy resolution, roughly 1 keV ($\sim 10^{-16}$ J), to avoid micro-phonic noise. Sources of vibrational noise include pumps, compressors, pulse tubes and the dilution unit.

CUORE will run for at least 5 years, and during this time the cryostat must be stable and relatively service-free to maximize live time. The CUORE-0 cryostat has a main bath that needs to be refilled every two days with liquid helium; this reduces live time by $\sim$7% (roughly 3 hours every 2 days). The CUORE-0 cryostat also contained a 1 K pot which introduced noise in the baseline of the detectors from the evaporation of helium. In light of this past experience, the CUORE cryostat was designed to be cryogen free, to improve live time and reduce noise.

Chapter 3

The CUORE-0 experiment and results

3.1 The CUORE Project

The CUORE experiment is in the final stages of construction at LNGS of INFN, with the detector installation completed August 26^{th}, 2016. Its primary purpose is to search for $0\nu\beta\beta$ decay in ^{130}Te using an, approximately one tonne, array of 988 TeO_2 bolometers operated near absolute zero ($\sim$ 10 mK). So far $0\nu\beta\beta$ decay has not been observed in ^{130}Te or any other double beta decay candidate isotopes. Searching for this hypothetical process has become the focus of intense experimental effort utilizing a broad range of technologies [8]. A number of experiments, using different isotopes, have placed experimental upper limits on the $0\nu\beta\beta$ half-life for ^{76}Ge [5] and ^{136}Xe [33, 69]. The candidate isotope ^{130}Te was chosen due to the large and accurately known Q-value [103, 106, 110] as well as the large natural abundance (34.2 %) [63].

The detector is composed of 19 towers, for a total detector mass is 741 kg of TeO_2. Since the bolometers are made with natural Te this translates to a total mass of 206 kg of ^{130}Te. Each tower contains 52 TeO_2 5×5×5 cm^3 crystals ($\sim$750 g each), with four TeO_2 crystals (2×2 configuration) per floor supported by a copper frame. Crystals are mounted directly to the copper frame using carefully designed PTFE brackets, which also serve as a weak thermal link between the crystals and the copper frame. A single neutron transmutation doped (NTD) germanium thermistor is attached to each crystal for the signal readout. A silicon resistor (joule heater) is also fixed to each crystal, to deliver a reference energy pulse which is used to stabilize

gain of bolometers to correct for temperature variations. The CUORE project builds on experience gained from CUORICINO, a previous single tower experiment made up of 62 bolometers for a mass of ∼40 kg of TeO_2. CUORICINO collected data from 2003 to 2008 and until recently held the best lower limits of the $0\nu\beta\beta$ decay half-life of ^{130}Te at $T^{0\nu}_{1/2} > 3.0 \times 10^{24}$ y (90% C.L.) [28].

In progressing from CUORICINO to CUORE, to increase the sensitivity to observe $0\nu\beta\beta$ decay, the active mass of the detector was increased by a factor of 19 and the experimental background decreased by an order of magnitude. Rather than proceed directly from CUORICINO to CUORE, an intermediate experiment called CUORE-0 was proposed as a way to validate background reduction techniques. It was designed to run as a standalone experiment, but also serve as a crucial test to validate the CUORE detector design, to commission the tower assembly line, as well as to develop and test DAQ and analysis framework (on a smaller scale); all while CUORE was being built. CUORE-0 was the first tower to be produced with the CUORE tower assembly procedure, and has an active mass comparable to CUORICINO; TeO_2 mass of 39.1 kg, which translates to 10.9 kg of ^{130}Te.

The selection and handling of the detector materials was done with the objective of minimizing the background contamination in CUORE-0. TeO_2 crystals were grown by the Shanghai Institute of Ceramics of the Chinese Academy of Sciences (SICCAS). A radio-purity control protocol [27] was developed in collaboration with SICCAS to limit the bulk and surface crystal contamination as a result of the production process. Only materials certified for radio-purity were used to grow the crystals. To limit the the cosmogenic activation of the crystals, each batch was transported to LNGS by sea. Upon arrival, each crystal shipment was stored underground in the parts storage area (PSA) where they were vacuum sealed and stored in a nitrogen flushed environment until tower assembly. To minimize the exposure of the detector to radon, tower construction was carried out inside nitrogen-flushed glove boxes, within the CUORE

(class 1000) clean room.

As a quality assurance test for each batch, referred to as a CUORE Crystal Validation Run (CCVR), four crystals were selected at random and operated as bolometers in a R&D cryostat located in Hall C of LNGS. For the ^{238}U decay chain, the measured bulk and surface contaminations were less than 6.7×10^{-7} Bq/kg and 8.9×10^{-9} Bq/cm^2 at 90% C.L., respectively [12]. Similarly, for the ^{232}Th decay chain the measured bulk and surface contaminations were less than 8.4×10^{-7} Bq/kg and 2.0×10^{-9} Bq/cm^2 at 90% C.L., respectively [12]. Material screening data of the small parts indicate that their radioactive content contributes less than 10% of the total background in the $0\nu\beta\beta$ region of interest (ROI). The definition of small parts includes the NTD thermistors and silicon heaters that are glued directly to the surface of the TeO_2 crystals.

From the experience gained from the CUORICINO experiment, the most significant background contributions are expected to be from the radiopure electrolytic tough-pitch copper (Cu-ETP) of both the tower frame and surrounding thermal shields. To reduce the background contribution from the frame, the copper pieces were redesigned to reduced the total mass and surface area by a factor of 2.3 and 1.8, respectively. To further mitigate the surface contamination of the copper structure, three surface treatment techniques [15] were tested; a series of tumbling, electropolishing, chemical etching, and magnetron plasma etching were chosen for the surface treatment. The upper limit on of the surface contamination of the cleaned copper was measured in R&D bolometers to be 1.3×10^{-7} Bq/cm^2 (90% C.L.) for both ^{238}U and ^{232}Th [15].

To house a tonne scale bolometric detector a very large experimental volume (on the order of a cubic meter) is needed, which translates to an even larger cryostat. A three story building, called the CUORE hut (figure 3.1), was constructed underground at LNGS to house the cryostat (figure 3.2) and to construct the detector. The ground

Figure 3.1: Photograph of (left) the CUORE hut and (right) the CUORICINO/CUORE-0 hut.

floor of the CUORE hut is divided in to two parts. One half is dedicated to the cryostat vessel storage and external lead shield. The other half is where all the pumps, compressors, and the dilution unit gas handling system are located. The hut was designed in this way to remove vibrational noise of pumps by placing them far from the cryostat. The test cryostat was also located at the ground flood during independent commissioning of the dilution unit. The fast cooling system is also located on the ground floor. The entire first floor is the CUORE clean room (CR), a class 1000 clean room made up of five distinct rooms. The detector assembly procedure is designed to minimize the recontamination of clean components, and every step of detector assembly took place in a nitrogen flushed glovebox to minimize the exposure to radon. In the initial (4 K) cryostat commissioning phase, the section of the clean room containing the cryostat was isolated from the rest of the clean room. It was not a clean room during this part of cryostat commissioning. Once

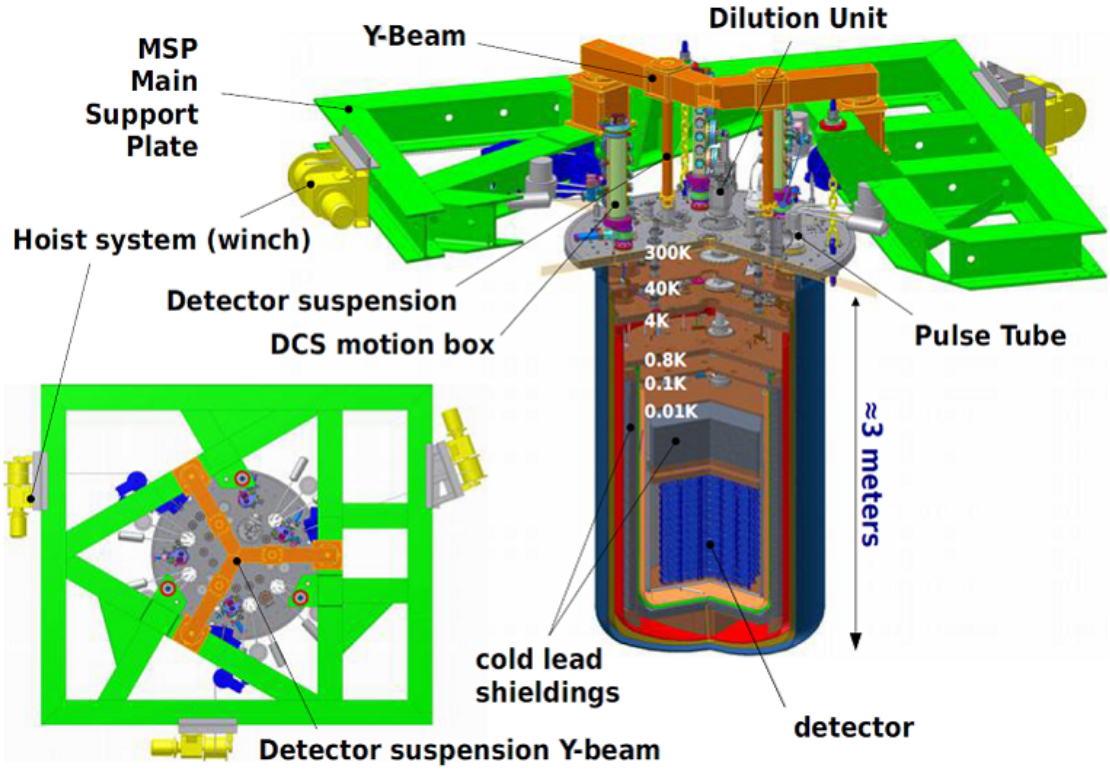

Figure 3.2: Sketch of CUORE cryostat from the top (left) top view and (right) side view, with relevant components labeled.

the dilution unit (DU) and cryostat were merged and vessels closed, this area (CR5) was throughly cleaned and regained its cleanroom status. The second floor allows for access to the top 300 K flange of the cryostat, as well as access to the suspensions and hoist system. Additionally the electronic racks, data acquisition system (DAQ), cryostat control programs and shifter workspace are on the second floor.

3.2 The CUORE tower assembly line

The detector assembly procedure is designed to minimize the recontamination of clean components and took place underground in the class 1000 clean room inside the CUORE hut (figure 3.3). The CUORE clean room (CCR) is located on the first floor of the hut, but after assembly the CUORE-0 detector had to be transported to the nearby CUORICINO hut. Every step of detector assembly took place in nitrogen

flushed glove boxes, to minimize the exposure to radon, and all tools used inside these glove boxes were cleaned and certified for radio purity. The rooms of the CR are intuitively numbered in the order that detector components enter the clean room, are assembled, stored, and installed in the cryostat. The first room, with access to the outside, is divided into two sections separated by a metal bench and a clear plastic sheet. The area that one enters first, from outside, is called CR0, and contains lockers and shelves with the required clean room attire. This includes clean room suits, hoods/hairnets, foot covers, as well as clean room safety shoes for cryostat work. Dressing takes place in the CR0; clean room attire was required in all areas beyond the clear plastic sheet. Cleanroom cleaning supplies, rubber gloves, important phone numbers, the LNGS shuttle schedule, and containers for the disposal of clean room refuse are found in CR1.

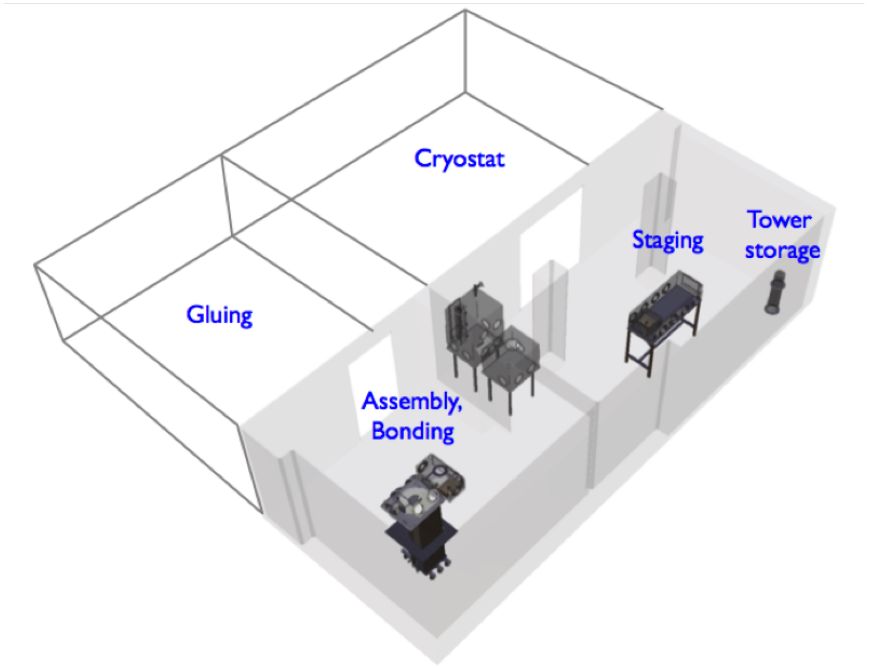

Figure 3.3: Sketch of the first floor (clean room) of the CUORE hut, with relevant tower assembly activities for each room labeled. Note: the entrance/dressing room is not shown in this figure.

The first step in the CUORE tower assembly line (CTAL), carried out in CR2, is the gluing of the NTD-Ge thermistor and heater to each TeO_2 crystal. This operation is done in a nitrogen flushed glove box, (figure 3.4) to reduce the radon contamination. The constant flow of nitrogen prevents radon from settling on to the surface of the crystals, which results in a higher α-decay background. The actual gluing process is fully automated, which minimizes human interaction with parts, and results in highly reproducible glue spot deposition. Knowledgeable technicians and shift personnel (shifters) were needed to oversee the gluing procedure to ensure correct procedure and operation, as well as load/unload the naked/glued crystals from the glove box. Glued crystals were placed back in rubber vacuum boxes and returned to the parts storage area (PSA) where they were stored under nitrogen, with all remaining unassembled detector components, until needed.

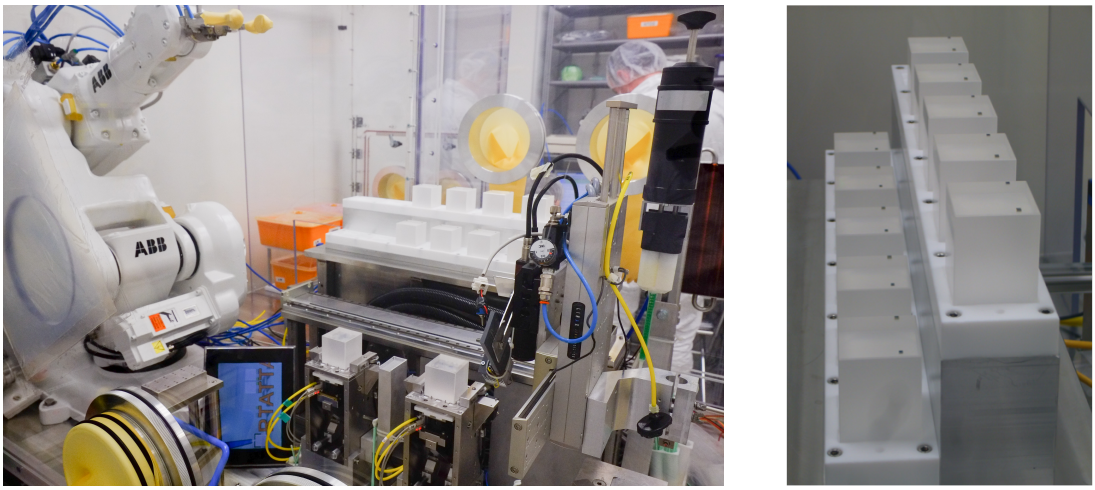

(a) (b)

Figure 3.4: View inside the glovebox in CR2 (a), used to glue a NTD-Ge thermistor and heater to each of the TeO_2 crystals, and (b) a close up view of glued crystals drying in the glovebox.

The next step of the CUORE tower assembly line, tower construction and wire bonding, was performed in CR3. Glued crystals and detector components, such as the ultra-cleaned copper and PTFE parts, were transferred under vacuum to the tower

assembly glove box in CR3, where they were unpacked and inspected. Following this quality assurance check, tower construction could proceed. Towers were built from the ground up, in a modular floor-by-floor fashion, with the crystals mounted in the PTFE holders as the frame was assembled. As each module was completed, the tower was lowered in to a sealable, nitrogen-flushed, storage garage; this allowed the assembly team to work at the same height inside the glovebox. Additionally, the tower garage was designed to safely store the tower being assembled in the event that the top of glove box needed to be removed, or in the event of contamination.

Once all 13 levels of the tower were complete, the next step was to attach a set of flexible printed circuit boards (PCBs) with copper traces [18, 47] to the copper frame of the tower; starting at the base of the frame and ending at the top (figure 3.5). The remaining length of the PBCs remained carefully rolled up inside a cylindrical

Figure 3.5: Photograph of the top of the CUORE-0 tower, zoomed in to see one of the flexible PCB strips that runs along the length of the tower.

PTFE container, that resembles a hair roller. There are two per tower, one for each side of the tower with the flexible PCBs attached, and they remained at the top of the frame until detector installation. Once installed, the upper length of the flexible PCBs were removed from the container, unrolled after which they were connected

to another custom made flexible PCB on the 10 mK plate of the cryostat. Next, a vertical bonding machine (figure 3.6) with auxiliary X-Y motion was used to connect thermistors and heaters to the crystals, and to the copper pads of the PCB strips fixed to the frame, via 25 μm diameter gold wires. After bonding, the final step in tower assembly is to place protective covers over the detector wire strips, to prevent damaging the 25 μm diameter gold wire connections.

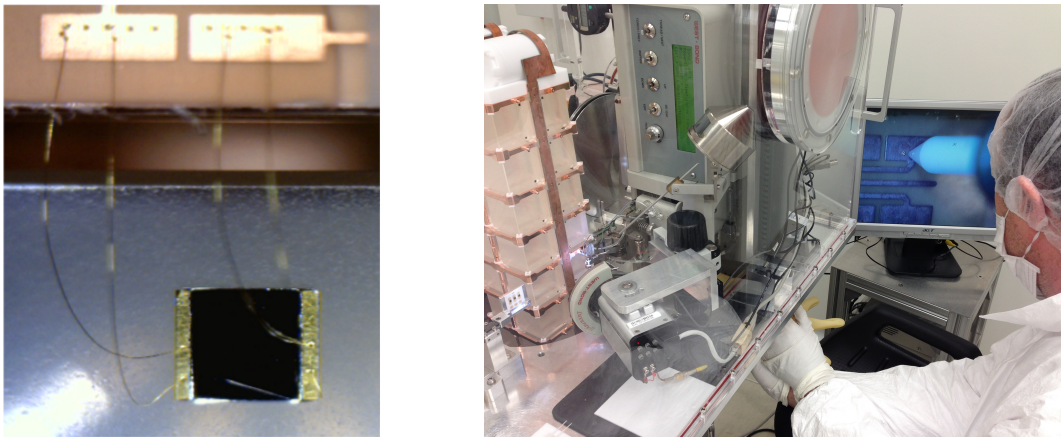

(a) (b)

Figure 3.6: Close up photograph (a) taken during wiring bonding, and photograph of a bonding shifter (b) operating the bonding machine.

Once the assembly of CUORE-0 was complete (figure 3.7), the tower was placed into a cylindrical 10 mK thermal shield, made of copper, and then into and a storage container. From there the detector was transported, from the first floor of the CUORE hut to the first floor of the CUORICINO hut, for installation in the CUORICINO cryostat. The detector was transported from CR3, by four people, through CR4 to the external doors in CR5, where it was securely fastened to the tines of a fully extended fork lift. The forklift slowly backed out of the CR5 doorway and proceeded to carefully lower the detector to the ground. The tower was then transported a short distance, maybe 10 meters, to the front of the CUORICINO hut, where it was raised up and placed onto the first floor of the CUORICINO hut, then finally moved into the CUORICINO clean room. Mounting of the tower to the cryostat was

done in the CUORICINO clean room to minimize environmental exposure, and was flushed with nitrogen for as long as possible. The successful operation of CUORE-0 demonstrated the validity of the CUORE tower assembly line and of the CUORE cleaning procedures.

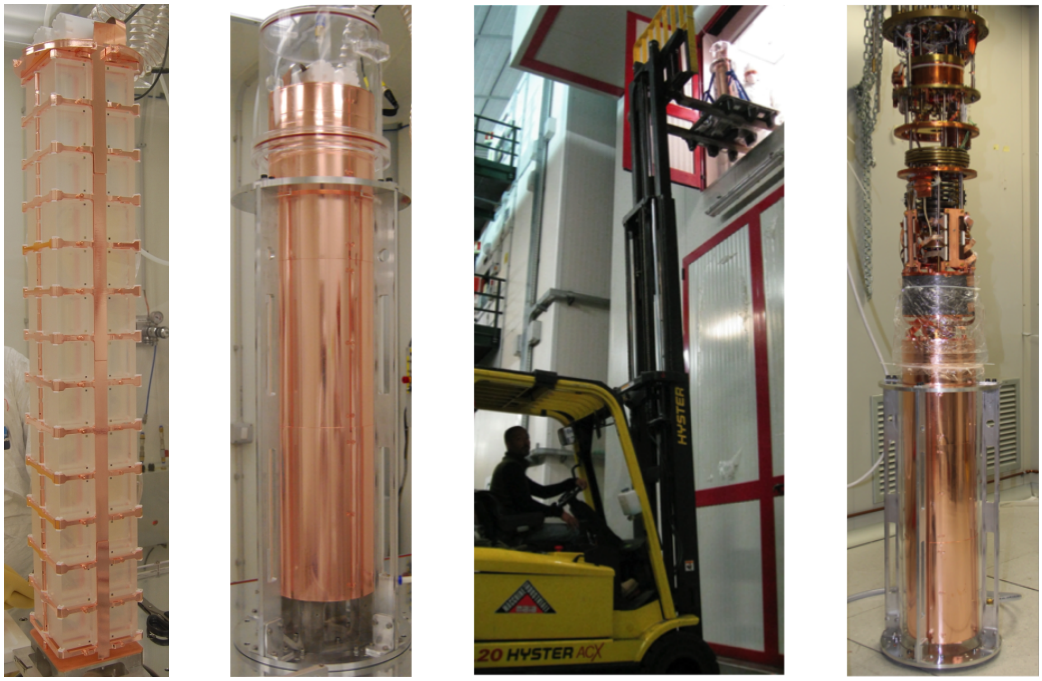

(a) (b) (c) (d)

Figure 3.7: Photographs of the CUORE-0 tower (a) in glove box after completion, (b) closed inside the 10 mK thermal shield, (c) being transported to the CUORICINO hut, and (d) mounted to the CUORE-0 cryostat.

After assembly, the 19 CUORE towers were placed in a clear, cylindrical, container and moved into CR4 for storage (figure 3.8). Towers were continuously flushed with nitrogen, until they were needed for installation. Once the cryostat commissioning was completed the towers were moved from CR4, the storage area, to CR5 which houses the inner part of the cryostat. During detector installation, a custom-built cart was used to position the tower under the cryostat for mounting (figure 3.9). When a tower was not being installed, the detectors were stored in a nitrogen-filled protective bag and monitored remotely by off-site shifters, in contact with people

onsite, in the event anything goes awry. Figure 3.10 is a photograph of all 19 CUORE towers suspended from the CUORE cryostat.

Figure 3.8: Completed CUORE towers were stored in CR4, in special containers constantly flushed with nitrogen, until they were ready to be mounted to the cryostat.

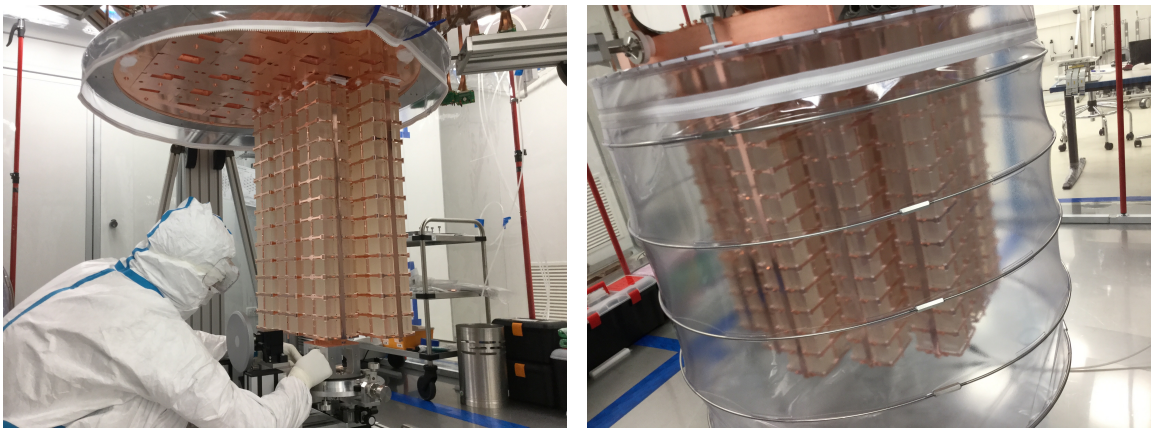

(a) (b)

Figure 3.9: During detector installation, a custom-built cart (a) was used to position CUORE towers under the cryostat for mounting/installation. When tower installation was not taking place, the mounted towers were stored (b) in a nitrogen-filled protective bag.

3.3 CUORE-0 experimental setup and infrastructure

As mentioned previously, CUORE-0 was built in the CUORE clean room using the new tower assembly approach, but relied entirely on the existing infrastructure and resources of the CUORICINO experiment. This includes the cryostat, the external lead and borated-polyethylene neutron shielding, and the faraday cage [17, 28]. A

(a) (b)

Figure 3.10: Side view (a) and bottom view (b) of all 19 towers of CUORE suspended from the cryostat.

sketch of the cryostat and shielding used for CUORE-0 and CUORICINO (not to scale) is shown in figure 3.11(b), along with photos of both detectors. The indicated radioactivities of the lead shields refer to the decay of ^{210}Pb. Since CUORE-0 used the same infrastructure, and was operated in the same cryostat as its predecessor, the contribution to the background from these components was expected to remain unchanged.

Unlike the previous experiment, both CUORE-0 and CUORE use flexible PCB cables and in situ wire bonding for the electrical wiring of each tower. This is one of the major upgrades to improved the robustness of the bolometer readout wiring over the previous design. A set of flexible PCB cables with copper traces [18, 47] were attached to the copper frame of the tower starting at the base of the tower to the top. Thermistors and heaters are connected to the PCB via 25 μm diameter gold wires. The upper end of the PCB cables are connected to another custom made flexible PCB on the 10 mK plate; from there a set of Manganin twisted pair flat ribbon cables run uninterrupted through feedthrough tubes on the top plate of the cryostat. The front end electronics [26, 29, 30] and data acquisition hardware were also identical to the ones used for CUORICINO.

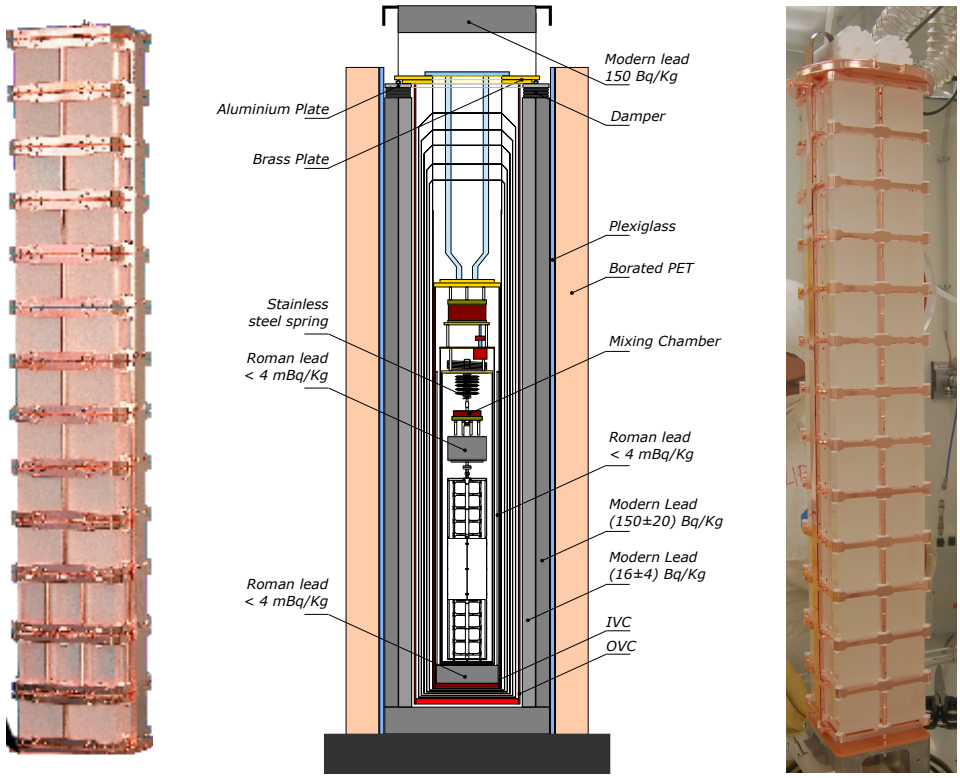

(a) (b) (c)

Figure 3.11: Diagram of the (b) cryostat used to operate the (a) CUORICINO and (c) CUORE-0 detectors; located in Hall A of the LNGS underground facility.

3.4 Data collection

The CUORE-0 detector construction was completed in March 2012 and was cooled down for the first time in August 2012. Following detector installation and commissioning, data collection began the following year in March 2013. Out of the 52 total bolometers, CUORE-0 only had three (6%) that were not fully operational. In the assembly of CUORE-0, one NTD and one heater could not be bonded. When the detector was cooled down, a second heater was lost. Once a bolometer loses the connection to the thermistor, it is a dead channel and is of no use. The two remaining heater-less bolometers that lost the connection to the heater, but still have a working thermistor, can still potentially be of some use in future non-standard analysis without thermal gain correction.

NTDs are biased using two low noise load resistors. The output voltage is measured with a specially designed low-noise (room temperature) preamplifier, a programmable gain amplifier, and a six-pole Thomson-Bessel low pass filter with a programmable cutoff frequency set to 12 Hz. The data acquisition (DAQ) continuously sampled each waveform at 125 Hz with ±10.5 V dynamic range and 18 bit resolution [8]. Software was used to scan the continuous data stream. Triggered events were stored in a 5 second window; one second before the signal. Typical rise times of pulses from particles depositing energy in the crystal are 0.05 seconds. The signal had two decay components, one fast and one slow. The fast decay time is determined from heat capacity of crystal and thermal conductivity to the tower frame that acts as a heat sink and is roughly 0.2 seconds. The slow decay time is determined by the heat capacity of the PTFE spacers and other auxiliary components and is 1.5 seconds. The rise time is determined primarily by the roll-off of the Bessel filter[8]. Typical trigger threshold energies of bolometers vary between 30 keV to 120 keV. To study the noise behavior, the detector waveforms were recorded for 5 seconds at intervals of 200s. Detector noise sampling was done without the signal trigger and simultaneously for every channel (so the 5 second interval was the same time for every channel).

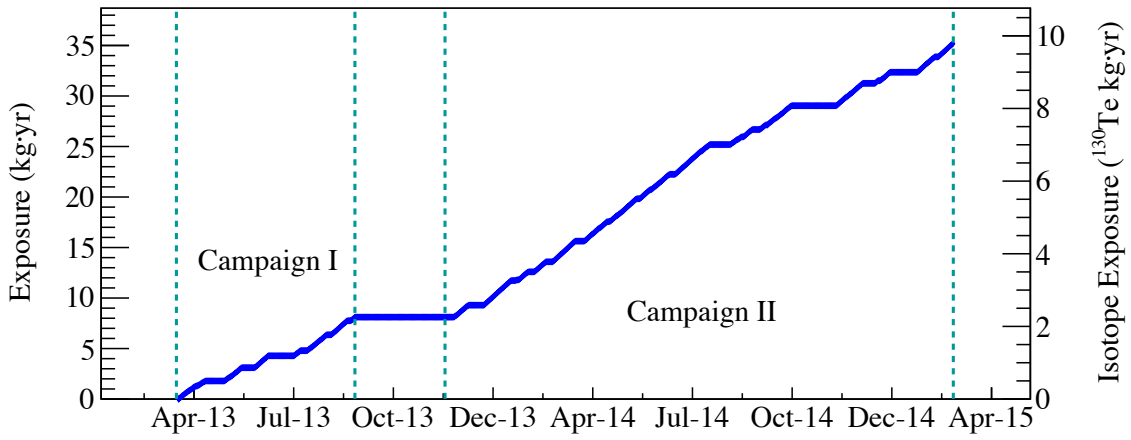

Figure 3.12: Plot of the accumulated CUORE-0 data over time. The left vertical axis refer to total TeO_2 exposure, while the right refers to ^{130}Te exposure.

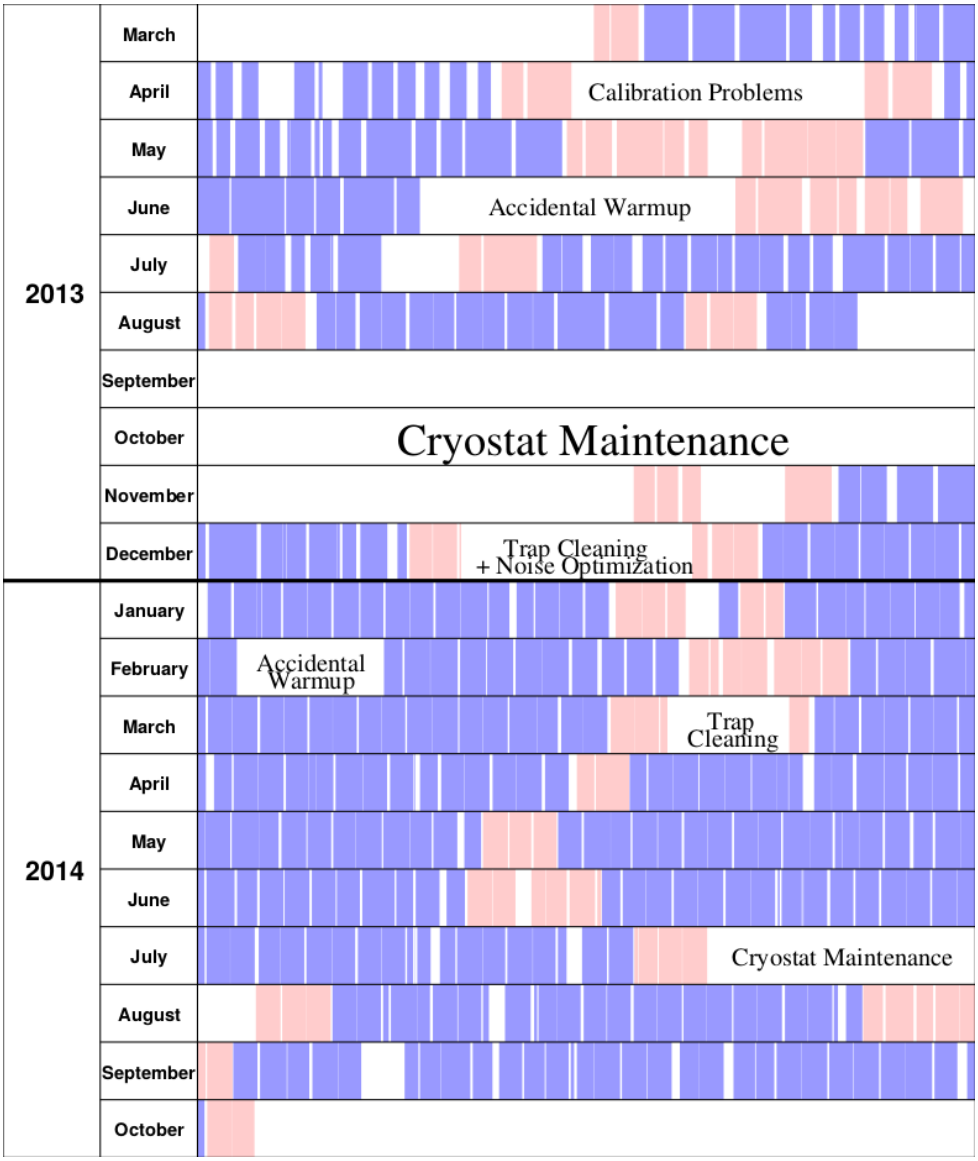

Figure 3.13: Timeline break down of the CUORE-0 data taking. The blue intervals represent physics data taking, red/pink intervals represent calibration data taking, and white represents detector down time.

Data collection is broken into two phases, separated by a roughly three month period of cryostat maintenance (see figure 3.13). Phase I was the data collected between March 2013 - September 2013, resulting in 8.5 kg yr of TeO_2 exposure (2.0 $kg \cdot yr$ of ^{130}Te). Phase II was the data collected between November 2013 - March 2015, resulting 26.7 $kg \cdot yr$ of TeO_2 exposure (7.8 $kg \cdot yr$ of ^{130}Te). Combining the data of Phase I and Phase II, a total exposure of 35.2 $kg \cdot yr$ of TeO_2 (9.8 $kg \cdot yr$ of

^{130}Te) was obtained. A visual representation of periods when CUORE-0 was taking data is shown in figure 3.13. The blue shaded regions represent periods where the detector was collecting useful physics data, while the red/pink shaded regions were intervals when detector was being calibrated. White sections represent periods of detector down time. The reoccurring, short, intervals of down time was when the ^{4}He in main bath of the cryostat needed to be refilled, which occurred roughly every two days. It takes roughly an hour to preform the refill and wait for the detector baselines to return to their previous values. For the prolonged periods of detector down time, comments summarizing the various reason are recorded; typically these fall into two categories: cryostat maintenance and accidental warms.

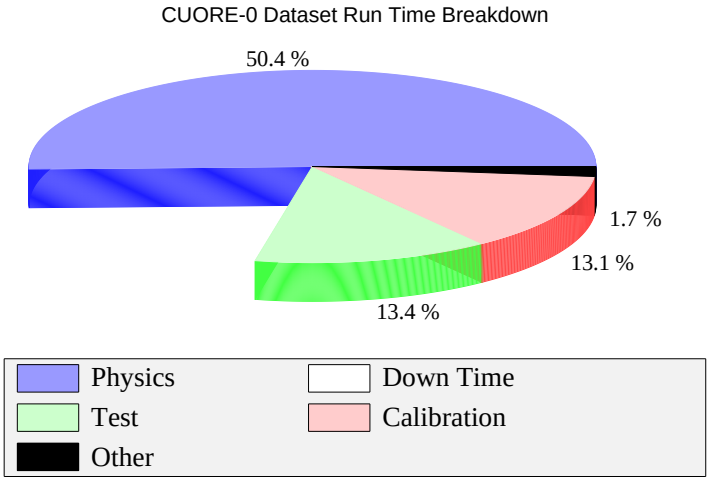

Figure 3.14: Breakdown of CUORE-0 measurement types, including down time.

The data acquired with CUORE-0 are grouped into 20 data sets; each data set consists of a set of initial calibration runs, a series of physics runs, and a set of final calibration runs. Calibration data refer to the sum of all calibration runs, while physics data refer to the sum of all physics runs to search for $0\nu\beta\beta$ decay. The signal rates of each bolometer for the calibration and physics data are 60-70 and 0.5-1.0 mHz, respectively. Physics data were collected in intervals of roughly one day, called runs, which are interrupted for 2 - 3 hours every 48 hours in order to refill the main bath of the cryostat with liquid helium. During calibration runs, the detector was

irradiated with two thoriated tungsten wires, each with a ^{232}Th activity of 50 Bq. The wires were inserted into two vertical tubes, on opposite sides of the tower that run between the outer vacuum chamber and the external lead shielding. Each channel was calibrated using γ-rays from daughter nuclei of ^{232}Th in the energy range from 511 to 2615 keV, as shown in figure 3.15. Data collected in between calibration runs are combined into datasets. A data set is roughly three weeks of physics data sandwiched between calibration runs.

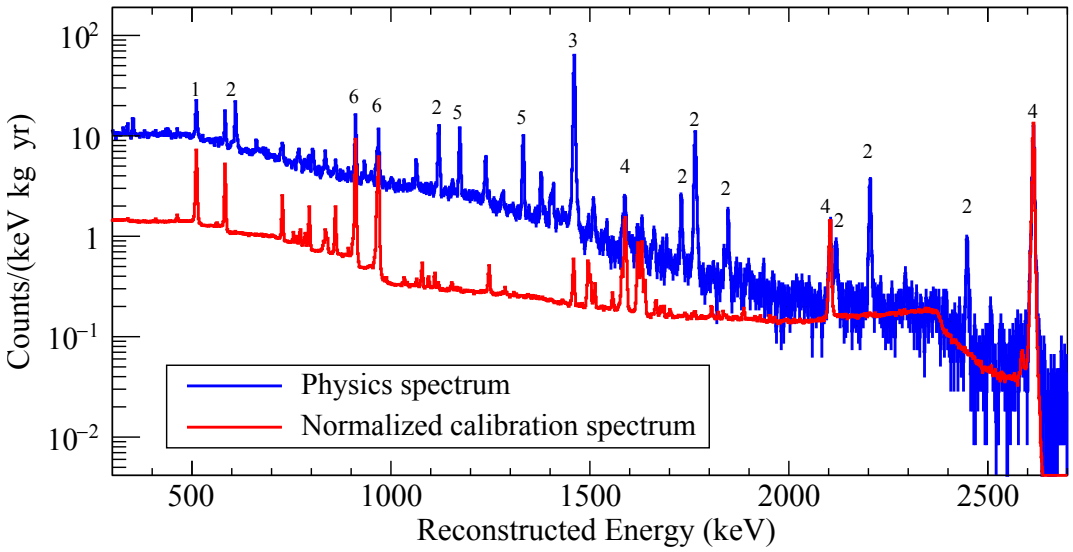

Figure 3.15: Energy spectra of physics (blue) and calibration (red) data; the latter is normalized relative to the former at 2615 keV. The peaks are identified as (1) electron-positron annihilation, (2) ^{214}Bi, (3) ^{40}K, (4) ^{208}Tl, (5) ^{60}Co, and (6) ^{228}Ac.

3.5 Data processing and analysis techniques

Data processing and analysis techniques are focused on the correct reconstruction of each triggered event energy (optimum filtering technique) and eventually to the creation of a calibrated energy spectrum that will be used in higher level analysis. To account for temporary degraded performances on each individual bolometer due to large baseline excursions, or elevated noise levels, low-quality data intervals are rejected on a channel-by-channel basis (reject bad intervals filter). The total expo-

sure is obtained by summing the individual exposures of each bolometer. CUORE-0 data analysis follows the same procedure that was used for CUORICINO [17]. This includes the amplitude evaluation, gain correction, energy calibration, and time coincidence analysis among the bolometers.

Pulse amplitude is evaluated by first maximizing the signal-to-noise ratio (SNR) with an optimum filter. Fourier components of each pulse are weighted at each frequency by the expected SNR, which is calculated for each channel with an average pulse of 2615 keV γ rays, and the average power spectra of the noise events. For the gain correction of each bolometer, the amplitudes of pulser events are compared to their baseline voltages to determine the gain dependence on temperature. The gain due to the temperature dependence is removed for each signal pulse. For the energy calibration a third order polynomial fit was used in the energy range form 0 to 3.9 MeV since the relationship between energy and stabilized amplitude is found to be slightly nonlinear. The deviation from a linear fit is less than 10 keV at the 2615 keV peak. If any two or more crystals register signal pulses within 100 ms of each other, the events are tagged as coincidence events. These multi-crystal events are mostly attributed to backgrounds such as Compton-scattered γ rays or an α decay near the surface of one crystal that is facing an adjacent crystal.

The event selection criteria can be categorized as follows: basic data quality, pile-up, pulse shape, and anti-coincidence. The basic data quality cut rejects events within low-quality data intervals that occur when the detectors are too noisy, there are DAQ timing problems or the baselines of the detectors change too dramatically. The pile-up cut requires that only one pulse exists in a 7.1 second window around the measured trigger time. Due to the relativity long rise and decay times of a pulse, and the negligible pulse shape dependence on energy at energies above 1 MeV, the pulse shape of the possible ^{130}Te $0\nu\beta\beta$ decay signal is expected to be similar to that obtained from the 2615 keV γ-ray peaks. Therefore, the pulse shape cut requires

that the signal shape is comparable to that obtained from the average pulse recorded with 2615 keV γ-ray events, and that the pre-trigger baseline slope is smaller that 0.1mV/Sample. The anti-coincidence cut requires that no other pulse is recorded anywhere else in the tower within a 100 ms interval. The obtained $0\nu\beta\beta$ decay detection efficiency is 92.9±1.8%. The efficiency after all cuts, except for the anti-coincidence cut, was obtained from the 2615 keV γ-ray peak. This efficiency was then multiplied by the efficiency of the anti-coincidence cut; obtained from the 1462 keV peak after applying the other cuts.

When considering only single crystal events, the confinement efficiency must be included. Confinement efficiency is the probability that both $0\nu\beta\beta$ decay electrons are contained inside a single crystal, and has been computed by MC simulation to be 87.4±1.1% [17]. Taking into account the 99.00±0.01% signal trigger efficiency, which is evaluated with pulsar events, the total $0\nu\beta\beta$ decay detection efficiency of CUORE-0 is 80.4±1.9%. This result is compatible with the value obtained from CUORICINO, which was found to be 82.8±1.1% [17].

A new automated bias voltage scanning algorithm was implemented to locate the optimal working point that maximizes the signal-to-noise ratio. The bolometer signals are amplified and then filtered with six-pole Bessel low-pass filters. Signals were digitized by two 32-channel National Instrument PXI analog-to digital converters with a 125 S/s sampling rate, 18-bit resolution, and 21 V full scale. All samples are stored continuously on disk. Afterwards, a constant fraction analysis trigger identifies triggered pulses with 626 sampling points (5.008 s), including a pre-trigger segment of 125 samples. Each bolometer had an independent trigger threshold ranging from 50 to 100 keV. In addition to the signal triggers, each bolometer was pulsed periodically at 300 second intervals with a fixed and known energy through the heater. The "pulser" events are used to monitor and correct the gain of the bolometers [25].

The event energy is estimated by modeling the time-waveform $v_i(t) = B_i \cdot s_i(t) +$

$n_i(t)$, of each bolometer, i, as sum of known detector response function $s_i(t)$ and unknown noise term $n_i(t)$; B_i is the signal response amplitude. To a close approximation, the signal response amplitude can be separated in to a temperature dependent bolometer gain factor and an energy dependent factor: $B_i = G_i(T) \cdot A_i(E)$. The following steps were performed on each wave form to get the deposited energy. First, measure B_i, while minimizing the effect of the noise term. This is done to maximize the energy resolution (pulse amplitude evaluation). Second, stabilize the temperature dependent gain term $G_i(T)$ versus the temperature drifts of the detector (thermal gain stabilization). Third, determine an energy calibration that models the form of $A_i(E)$. From these steps, the event energy can be extracted (energy calibration). Finally, blind the energy spectrum in the $0\nu\beta\beta$ region of interest. See reference [8] for a more detailed explanation of the CUORE-0 data processing procedure.

While CUORE-0 was running, a method of data blinding was implemented for the data in the $0\nu\beta\beta$ decay ROI. The blinding method was a form of data salting; where we randomly exchange a blinded fraction of events within ± 10 keV of the 2615 keV γ-ray peak with events within ± 10 keV of the $0\nu\beta\beta$ decay Q-value. The exchange probability varies between 1 and 3% and is randomized on a run by run basis. Since the number of 2615 keV γ-ray events is much larger than that of possible $0\nu\beta\beta$-decay events, the blinding algorithm produces an artificial peak at the decay Q-value and blinds the real $0\nu\beta\beta$ decay rate of ^{130}Te. This method of blinding the data preserves the integrity of the possible $0\nu\beta\beta$ decay events while maintaining the spectral characteristics with measured energy resolution and introducing no discontinuities in the spectrum.

The procedure of data blinding and unblinding was established prior to unblinding of real data. In order to get a head start on analysis, data from CUORE-0 was unblinded in two stages. Initially the first 17 (of 20 total) datasets were unblinded for $\beta\beta$-decay analysis, while the remaining three datasets were collected. The last

three datasets followed the same procedure as the previous 17 datasets, only they were unblinded as each dataset was processed. That is not to say that these data did not go through the same blinding procedure during collection. Even though the blinding/unblinding procedure was checked with mock data prior to ensure it could correctly reconstruct the true energy spectrum, a cross check to the blinding procedure was done with the real CUORE-0 data. All CUORE-0 data were reprocessed without the added step of blinding to show no changes in the final spectrum (when compared to the blinded and then unblinded energy spectrum). This validates the technique of blinding which will be used for CUORE.

3.6 CUORE-0 background and ^{130}Te $0\nu\beta\beta$ decay search results

The background rate in the neutrinoless double beta decay region of interest (ROI), 2.47 to 2.57 MeV, was measured to be 0.071 ± 0.011 $counts/(keV \cdot kg \cdot y)$. In the 2.70 to 3.90 MeV region, where the background is dominated by α particles, the measured background rate was 0.019 ± 0.002 $counts/(keV \cdot kg \cdot y)$ [31]. It is important to note that the background rate in the α dominated region has been reduced by a factor of 6 from that of CUORICINO[31]. This result appears to verify our understanding of background sources present in CUORE-0. Understanding the background sources in the detector is important because a similar background model is used to extrapolate the expected background in CUORE.

The background rate in the region of interest was evaluated using the blinded spectrum in the energy range 2470-2570 keV. This region includes the ^{60}Co sum-peak at 2506 keV and the salted peak at the $0\nu\beta\beta$ decay Q-value. An unbinned maximum likelihood fit was used to estimate the background rate in the region of interest. The likelihood function consists of the sum of a ^{60}Co gaussian peak, a salted $0\nu\beta\beta$-decay peak, and a flat background. In the fit, the mean of the ^{60}Co sum peak is initialized to 2506 keV and the mean of the salted $0\nu\beta\beta$ decay peak at 2528 keV. The

FWHM of both peaks is fixed to the detector resolution of 5.7 keV. The fit reveals that the overall background rate in the ROI is 0.071±0.011 (stat) $counts/keV/kg/y$. For comparison, the background rate of the CUORICINO crystals with the same dimension is 0.153±0.006 $counts/keV/kg/y$. Systematic uncertainties arising from background shape are studied by comparing constant and linear background models, and are found to be less than 3%. The systematic contribution from the uncertainty in energy calibration is less than 1%.

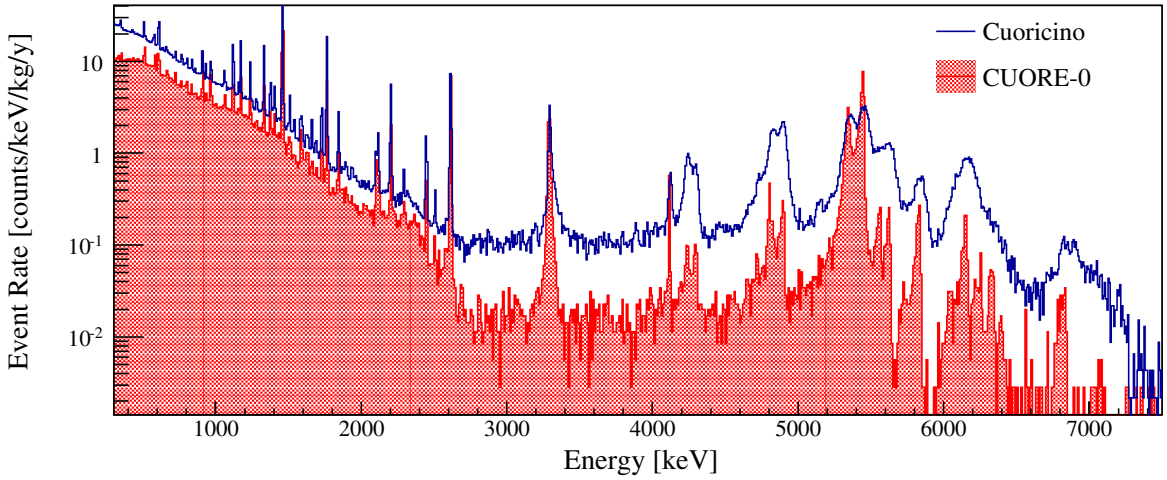

Figure 3.16: Spectrum of events with energy between 300 keV and 7500 keV measured in CUORICINO (blue/line) and CUORE-0 (red/solid).

The two major sources of background in the region of interest are degraded α particles from surface contamination on the detector components and γ-rays that originate from the cryostat. Degraded α particles with a decay energy of 4 to 8 MeV can deposit part of their energy in the $0\nu\beta\beta$-decay region of interest. These α events form a continuous energy spectrum extending from their decay energy to well below $0\nu\beta\beta$ decay region. The α background rate in the ROI is estimated by counting events in the α flat continuum region, defined to be from 2.7 to 3.9 MeV (excluding the ^{190}Pt peak region from 3.1 to 3.4 MeV). This energy range is above almost all naturally occurring γ-rays from ^{208}Tl decay. The measured rate for CUORE-0 is 0.019±0.002 $counts/keV/kg/y$, which improves on the CUORICINO

result of $(0.110 \pm 0.001 counts/keV/kg/y)$ by a factor of 6. The γ-ray background in the region of interest is predominantly from Compton-scattered 2615 keV γ-rays originating from ^{232}Th in the cryostat. Since CUORE-0 is hosted in the same cryostat used for CUORICINO, the γ-ray background is expected to be similar. The γ-ray background is estimated as the difference between overall background in the region of interest and the degraded α background in the continuum. The measured γ-ray backgrounds of CUORE-0 and CUORICINO are indeed comparable [17], consistent with the hypothesis that the background in the region of interest is composed of γ-rays from the cryostat and degraded α particles.

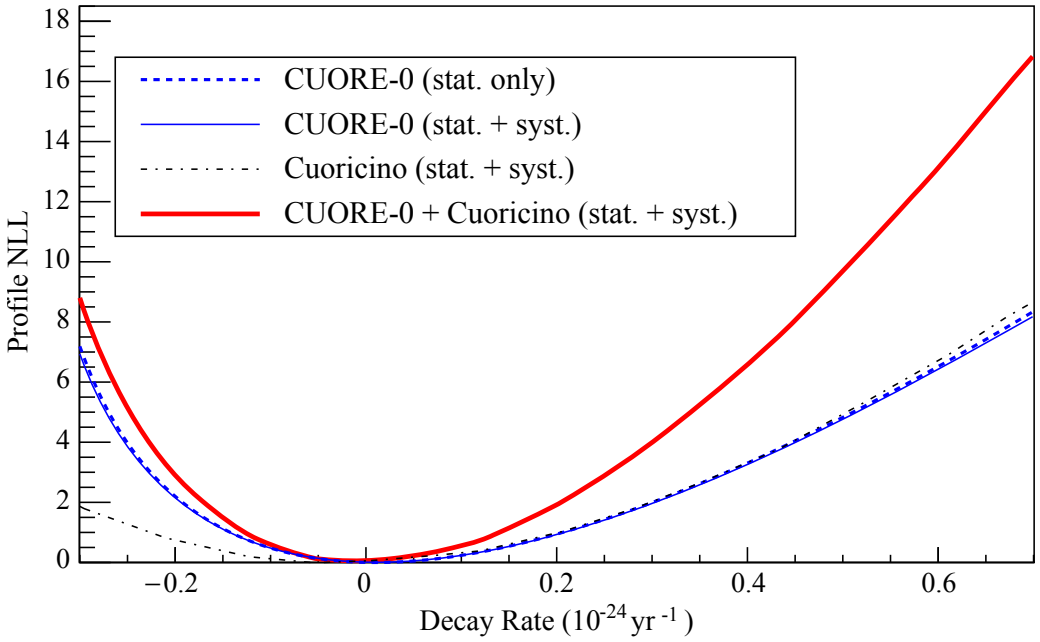

Figure 3.17: Profile negative log-likelihood (NLL) curves for CUORE-0, CUORICINO, and their combination [16].

After unblinding the data, the number of candidate events, in the $0\nu\beta\beta$ ROI (2470-2570 keV) were determined using an un-binned extended maximum likelihood (UEML) fit. A total of 223 candidate events were found with an experimental exposure of 35.2 kg $\cdot$ yr of natural TeO_2 (9.8 kg $\cdot$ yr of ^{130}Te). The best fit of the $0\nu\beta\beta$ decay rate is $\Gamma_{0\nu} = 0.01 \pm 0.12(\text{stat.}) \pm 0.01(\text{syst.}) \times 10^{-24}$ yr^{-1}. The best

fit of the background in the $0\nu\beta\beta$ ROI is: B = 0.058 ± 0.004(stat.) ± 0.002(syst.) c/keV/kg/y. No evidence was found for a signal and a 90% CL lower limit set from the profile likelihood: $T^{0\nu}_{1/2} > 2.7 \times 10^{24}$ yr. Combining the CUORE-0 result with the existing 19.75 kg · yr of ^{130}Te exposure from CUORICINO: $T^{0\nu}_{1/2} > 4.0 \times 10^{24}$ yr. This is the most stringent limit on this half life. Combined half-life limits yield a limit on the effective Majorana neutrino mass: $m_{\beta\beta} <$ (270-650) meV.

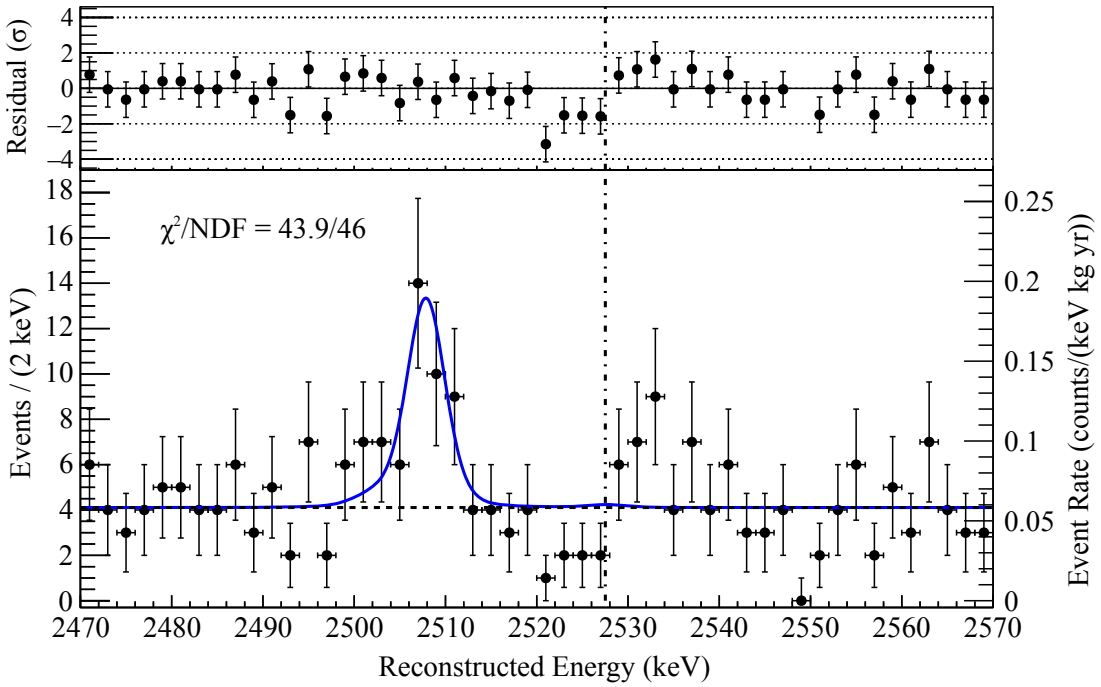

Figure 3.18: Bottom: The best-fit model from the UEML fit (solid blue line) overlaid on the spectrum of $0\nu\beta\beta$ decay candidates in CUORE-0 (data points). The dashed black line is the continuum background component of the best-fit model. Top: The normalized residuals of the best-fit model and the binned data. The vertical dot-dashed black line indicates the position of $Q_{\beta\beta}$ of ^{130}Te.

3.7 Conclusion

Projected sensitivity of CUORE: Using the measured background rate and energy resolution of the 2615 keV γ-ray peak, we obtain the CUORE-0 sensitivity with the approach outlined in [14]. With the excellent energy resolution, we construct a

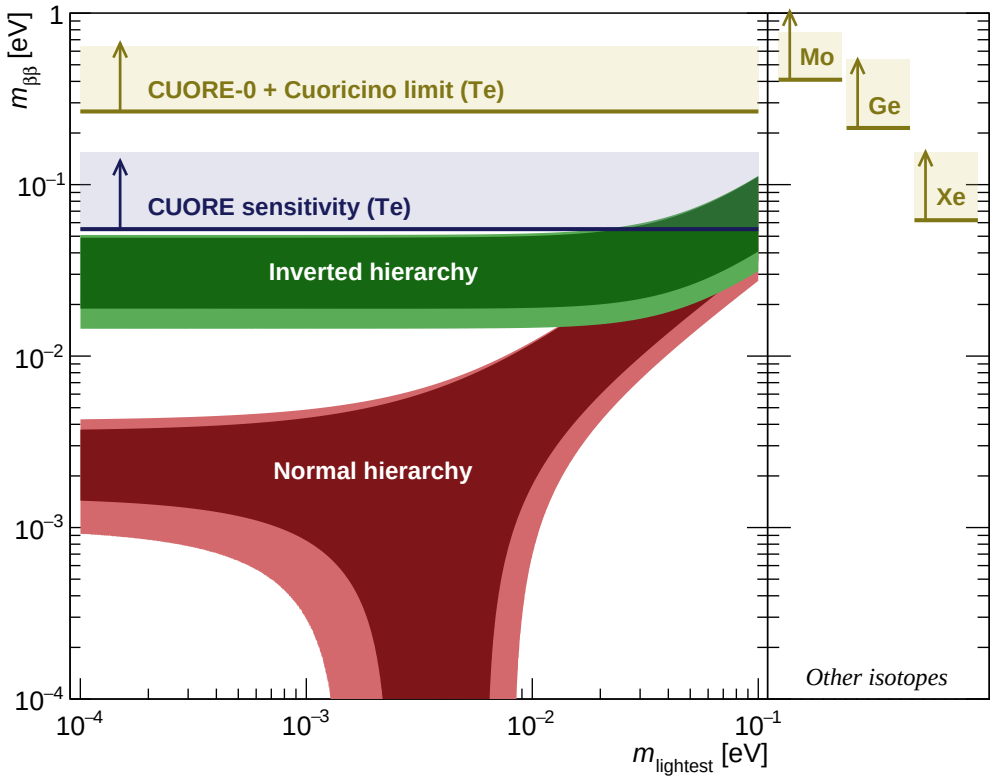

Figure 3.19: CUORE-0 sensitivity to $m_{\beta\beta}$, with projected CUORE sensitivity. Sensitivities obtained with other DBD isotopes are also included.

single-bin counting experiment with a 5.7 keV bin centered at the $0\nu\beta\beta$ decay Q-value. The sensitivity is obtained by comparing the expected number of signal events with Poisson fluctuations from the expected background rate in this bin.

Summary and outlook: The measured 5.7 keV FWHM in the $0\nu\beta\beta$ decay region of interest represents a slight improvement over CUORICINO and validates the CUORE-0 wiring scheme and assembly procedure. The background rates have been measured to be 0.071±0.011 counts/(keV·kg·y) in the ROI and 0.019±0.002 counts/(keV·kg·y) in the α continuum region, respectively. These results are a factor of 2 and 6 improvement, respectively, when compared to CUORICINO and were achieved through a more rigorous copper surface treatment, improved crystal production and treatment protocols, and more stringent assembly procedure in the clean environment.

As a technical prototype for CUORE, CUORE-0 demonstrates the feasibility of instrumenting an ultra pure ton scale bolometer array with 988 channels. By enhancing the procedure of the on-going CUORE assembly, we have improved assembly success rate close to 100%, which is a crucial achievement for large arrays such as CUORE. We have started implementing the noise decorrelation algorithms into the CUORE-0/CUORE data analysis package, with the aim of further improving energy resolution. CUORE-0 reconfirms the effectiveness of the copper cleaning technique and clean assembly procedure developed for CUORE. Compared to CUORE-0, the large array of CUORE affords more powerful time coincidence analysis and more effective self-shielding from external backgrounds, particularly those originating from the copper thermal shields or cryostat. With this stronger background rejection and the already demonstrated reduction of surface contamination, the CUORE background goal of 0.01counts/(keV·kg·y) is expected to be within reach. The projected half life sensitivity to ^{130}Te $0\nu\beta\beta$ is 9.5×10^{25} y (90% C.L.) with 5 years live time [14], reaching an effective Majorana neutrino mass sensitivity of 0.05 to 0.13 eV [38, 61, 62, 85, 90, 104, 109, 117]. Combining the 9.8 kg years of exposure of CUORE-0 with the 19.75 kg year of exposure from CUORICINO we obtain a bound of 4.0 $>10^{24}$ (90% CL bayesian). This is the most stringent limit to date on this half life. Using a range of nuclear matrix element estimates we interpret this limit on the efficiency Majorana $m_{\beta\beta}$ mass of 270-760 meV.

Chapter 4

Axion phenomenology

Apart from rare event searches involving neutrino-less double beta decay, experimental searches for axions and axion-like particles (ALPs) are also of current interest. The most concise explanation of what an axion is, but perhaps not the simplest, is that it is a hypothetical pseudo-Nambu Goldstone boson that comes about from the Peccei-Quinn solution to the strong CP problem in quantum chromodynamics (QCD).

4.1 The strong CP problem

The theory of Quantum Chromodynamics (QCD) is the best and most widely accepted theory of strong interactions. The strong force is responsible for the confinement of quarks into particles called hadrons; composite particles containing gluons and quarks. According to the quark model, the properties of hadrons are primarily determined by their valence quarks. The two families of hadrons are mesons and baryons. Mesons are composed of one quark and one anti-quark (e.g. pion) and baryons (e.g neutron) contain three valence quarks. There are also anti-baryons made up of three anti-quarks. Hadrons contain more than just valence quarks as is evident when comparing the mass of a hadron compared to the sum of the composite valence quarks. In fact, the mass of a hadron has little to do with the mass of its valence quarks. The majority of mass comes from the large amount of energy associated with the strong interaction; gluons morph into quark antiquark pairs and back to gluons making up a (virtual) sea of quarks and gluons.

QCD can predict with amazing accuracy physical processes over a large energy range, but contains a flaw known as the strong CP problem. The strong CP problem involves a discrepancy of many orders of magnitude between the theoretically predicted value for the neutron electric-dipole moment (NEDM) and its experimental upper bound. The full explanation is a bit more complicated and involves symmetries of charge conjugation, parity, and time reversal. Charge conjugation (C) is described as the reversal of electric charge and all internal quantum numbers. Parity (P) space inversion is the reversal of spacial coordinates, but of not time, and Time reversal (T) replaces t with -t, which also reverses time-derivatives like translation and angular momentum. More often than not, these individual symmetries (table 4.1) are conserved, but there are occasions when one or more of these symmetries do not hold. While the individual symmetries may not always be conserved, the product of CPT remains unchanged for any physically observable process ($H = H^*$). In other words, by simultaneously inverting charge, parity and time, physical laws retain their initial form. Typically these symmetries are discussed in terms of CP and T, so that if CP is conserved in some physical process then T is also conserved.

Table 4.1: Properties of C, P, and T symmetry.

Symmetry	Properties
Charge conjugation (C)	C $\rightarrow$ C*
Parity inversion (P)	$\mathbf{r} \rightarrow$ -$\mathbf{r}$, t $\rightarrow$ t
Time reversal (T)	$\mathbf{r} \rightarrow \mathbf{r}$, t $\rightarrow$ -t

The QCD Lagrangian naturally contains the following term that violates CP:

$$\mathcal{L}_\Theta = \Theta \frac{g_s^2}{32\pi^2} G_a^{\mu\nu} \tilde{G}_{a\mu\nu}, \tag{4.1}$$

where $G_a^{\mu\nu}$ is the gluon field strength tensor, $\tilde{G}^{a\mu\nu}$ is the dual tensor, g_s is the strong force coupling constant, and Θ is the QCD vacuum angle parameter. Since Θ is a strong interaction parameter it would naturally be of order unity. The neutron consists of three valance quarks, two down quarks ($q_d = -1/3$) and an up quark

($q_u = +2/3$) for a net charge of zero. The displacement of these charged quarks results in a non-zero neutron electric dipole moment which violates both Parity (P) and Time reversal (T) symmetry (and therefore CP) as shown in figure 4.1. The neutron electron dipole moment as predicted by QCD is approximately: $|d_n| \approx \Theta \times 10^{-16}\ e{\cdot}cm$.

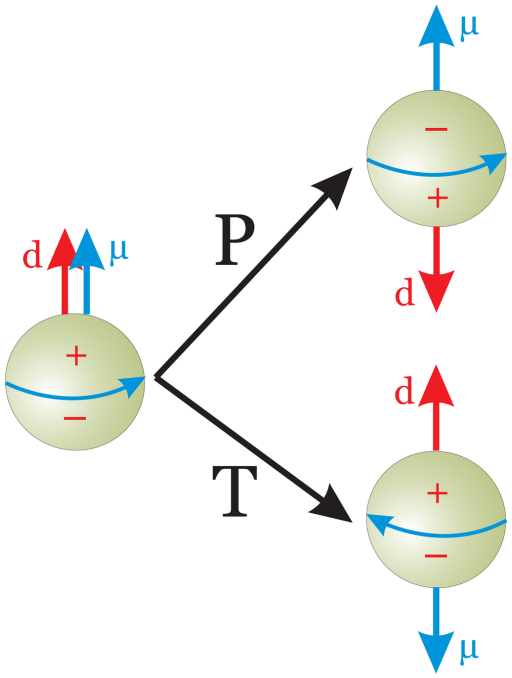

Figure 4.1: The neutron electric dipole moment (NEDM) violates both Parity (P) and Time reversal (T) symmetry (and therefore CP) [93].

The first experiment to measure the NEDM was preformed by Smith, Purcell, and Ramsey in 1951 (published 1957) in which they obtained a limit of $|d_n| < 5 \times 10^{-20}\ e \cdot cm$ [113]. These results clearly showed that the NEDM, and therefore Θ, is several orders of magnitude less than predicted by QCD, something Frank Wilczek called the strong CP problem. Over the next 50 years, the experimental bound on the NEDM has continued to decrease, roughly six orders of magnitude, as seen in figure 4.2. The current bound on the NEDM is $|d_n| \leq 1.9 \times 10^{-26} e \cdot cm$ [37]. In order for the theoretical predictions to match the current experimental upper limit on the NEDM, the value of Θ must be fine-tuned to an extremely small value $\Theta \leq 10^{-10}$.

The question then becomes, why exactly is this value so unnaturally small? Just to reiterate, the issue is not that the strong force violates CP, but rather the degree to which CP is violated in QCD.

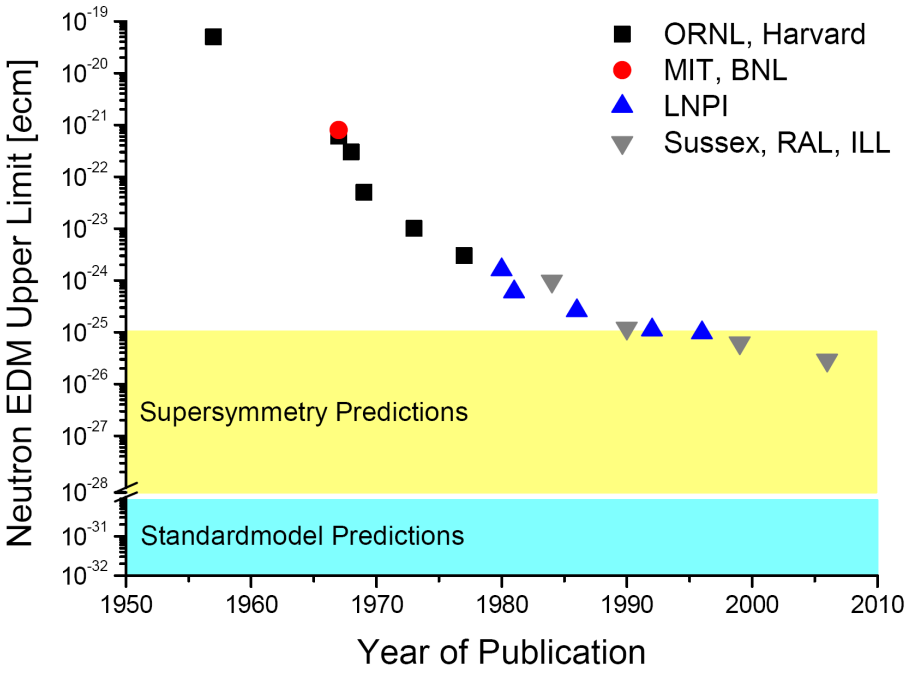

Figure 4.2: Experimental bounds on the neutron EDM verses publication year [93].

4.2 The Peccei-Quinn solution and the axion

While there are a handful of proposed solutions to the strong CP problem, the one proposed by Roberto Peccei and Helen Quinn remains the most appealing to date. Their solution assumes an additional global U(1) chiral symmetry, $U(1)_{PQ}$, in the QCD Lagrangian, that is spontaneously broken at large energy scale f_a [96, 97]. This mechanism generates an additional term that cancels the CP violating term, but also requires the existence of a new pseudo-scalar Goldstone boson; the axion (see eq 4.2). An interesting historical note, Frank Wilczek called the new Goldstone boson the axion after a dish soap that shares the same name because the PQ approach "cleans up" the strong CP problem [108].

After $U(1)_{PQ}$ is spontaneously broken, the CP violating part of the QCD Lagrangian becomes:

$$\mathcal{L}_\Theta = \left(\Theta - \frac{a}{f_a}\right) \frac{g_s^2}{32\pi^2} G_a^{\mu\nu} \tilde{G}_{a\mu\nu}, \tag{4.2}$$

where a is a pseudo-scalar field and f_a is the Peccei-Quinn symmetry breaking scale. Non-perturbative effects induce a potential on the field a, with a minimum at $a = f_a\Theta$, causing the two CP violating terms to exactly cancel. Accordingly, the Peccei-Quinn solution leads to the existence of a pseudo-scalar particle with nonzero mass [54]. The spontaneous symmetry breaking generates a pseudo-Nambu Goldstone boson (pNGB), the axion, as pointed out independently by Weinberg [119] and Wilczek [120] in 1978.

In addition to spontaneous symmetry breaking, $U(1)_{PQ}$ is also explicitly broken at low energy by instanton effects, which results in the axion acquiring a mass. The axion's mass is inversely proportional to the Peccei-Quinn symmetry breaking scale f_a, and is given in terms of π^0 properties as follows:

$$m_a = \left(\frac{z}{(1+z+w)(1+z)}\right)^{1/2} \frac{f_\pi m_\pi}{f_a} = 6[eV] \left(\frac{10^6}{f_a[GeV]}\right), \tag{4.3}$$

where $z = \frac{m_u}{m_d} \simeq 0.56$ is the ratio of up quark and down quark masses, $w = \frac{m_u}{m_s} \simeq 0.029$ is the ratio of up quark and strange quark masses. The mass of the pion is m_π = 135 MeV, and the pion decay constant is $f_\pi \approx 92$ MeV.

In general, the axion couples to hadrons, photons, and leptons with interaction strengths inversely proportional to f_a. For the Peccei-Quinn (PQ) axion model, there are theoretical predictions for axion couplings with photons, electrons and nucleons $g_{a\gamma}$, g_{ae}, and g_{aN} [54]. Note that the mass and coupling are related by equation 4.3; once the PQ symmetry breaking scale is fixed the axion mass is also fixed. The Standard Model PQ axion, in which $f_a \approx f_{EW} \approx 250\ GeV$, was excluded by a series of early experiments (radioactive sources, reactors, and accelerators) [108]. We are

motivated to search for axions because their discovery would validate the Peccei-Quinn solution to the strong CP problem.

4.3 Invisible axion models

After the Standard Model Peccei-Quinn axion was ruled out experimentally, invisible (or very light-mass) axion models were formulated where the global $U(1)_{PQ}$ symmetry is broken at a much higher energy ($f_a >> 250\ GeV$) [57, 79, 80, 111, 123]. Invisible axion models are appealing because they maintain the theoretically elegant solution to the strong CP problem but the trade-off is that, because of the higher symmetry breaking scale, the axion mass and couplings become extremely small; much weaker than the weak scale. The couplings are so small that detection will be very challenging; implying that these particles are effectively 'invisible". These models are still relevant because they can also account for some the dark matter in the universe [4, 52, 56, 99]. The axion mass for invisible axion models is also given in terms of π^0 properties just like the standard PQ axion; however, f_a is no longer a fixed value. Invisible axion models have no predicted values for f_a, and therefore no restrictions on the axion mass or couplings, except that they do obey equation 4.3. The mass remains inversely proportional to f_a but the parameters of axion couplings to leptons, photons, and nucleons (quarks and gluons) are now model dependent.

There are two (benchmark) invisible axion models that keep the axion in the form required for the solution of the strong CP-violation problem while suppressing its interaction with matter: the Kim, Shiftman, Vainstein and Zakharov (KSVZ) model and the Dine, Fischler, Sredniki and Zhitnitski (DFSZ) model. The KSVZ model is called the hadronic axion model [80, 111] and the axion-electron coupling does not exist at tree level. In this particular model the axion couples to quarks and photons at the tree level while the axion-electron coupling is through a higher loop. The DFSZ model is a grand unified theory axion model [57, 123]. It is a

more generic/non-hadronic axion model where axions couple to quarks, photons, and electrons at tree level. In the context of axion phenomenology both the KSVZ and DFSZ models will be discussed.

4.4 The axion-photon interaction

The axion has a generic property of a two photon interaction because its properties are closely related to those of neutral pions. Particles such as pions and axions, via a two-photon vertex, can transform into photons in an external electric or magnetic field via the Primakoff effect [100]. This two photon interaction is often exploited to search for axions. The Lagrangian describing the axion photon interaction is given by the following equation:

$$\mathcal{L}_{a\gamma} = \frac{1}{4} g_{a\gamma} F_{\nu\mu} \tilde{F}^{\nu\mu} a = -g_{a\gamma} \vec{E} \cdot \vec{B} a, \tag{4.4}$$

where F is the electromagnetic field strength tensor, $\tilde{F}$ is the duel of the field strength tensor, $g_{a\gamma}$ is the axion-photon coupling constant, a is the axion field and the electric and magnetic fields are $\vec{E}$ and $\vec{B}$, respectively. The coupling constant $g_{a\gamma}$ is given by:

$$g_{a\gamma} = \frac{\alpha}{2\pi f_a} \left(\frac{E}{N} - \frac{2}{3} \frac{4+z}{1+z} \right) = \frac{\alpha}{2\pi} \left(\frac{E}{N} - \frac{2}{3} \frac{4+z}{1+z} \right) \frac{1+z}{\sqrt{z}} \frac{m_a}{m_\pi f_\pi}, \tag{4.5}$$

where E and N are the electromagnetic and color anomaly parameters of the axial current associated with the axion field. In the DFSZ model [123, 57], $E/N = 8/3$, and in KSVZ [80, 111] $E/N = 0$, but in general the value of E/N is not known and the so there is a range of values that $g_{a\gamma}$ can take once the PQ symmetry breaking scale f_a is fixed. The axion line in the m_a-$g_{a\gamma}$ plane is defined by taking the taking the model-dependent factors to be of order unity.

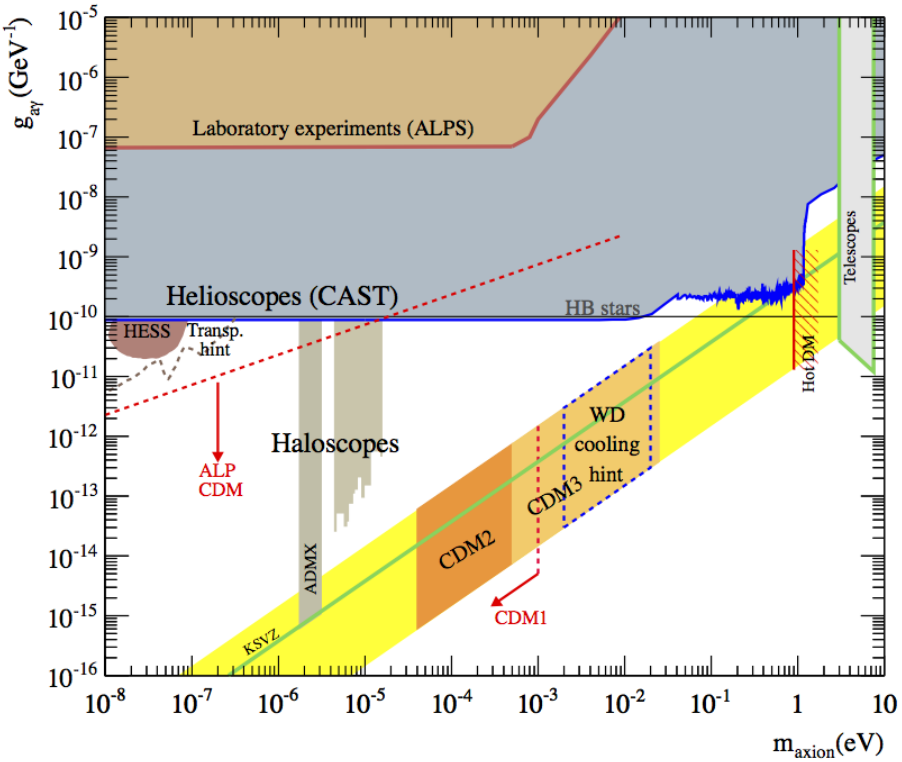

Figure 4.3: Exclusion plot for axion-photon coupling vs axion mass [77].

4.5 Axion-electron interaction

Apart from the more generic interaction of axions with photons, axions also interact with fermions, Ψ, by a derivative interaction of the form:

$$\mathcal{L} = \frac{C}{2f_a}\bar{\Psi}\gamma_5\gamma_\mu\Psi\partial^\mu a, \tag{4.6}$$

or the pseudoscalar form:

$$\mathcal{L} = -i\frac{Cm}{f_a}\bar{\Psi}\gamma_5\Psi a, \tag{4.7}$$

where C is a model dependent numerical factor and m is the mass of the fermion being considered. The derivative and pseudo scalar forms of the Lagrangian are equivalent only when a single axion is attached to the fermion line in a Feynman diagram. The pseudo scalar form expresses the axion-fermion interaction in terms of a dimensionless Yukawa coupling $g = C\ m/f_a$ and associated axion fine structure constant $\alpha_a =$

$g^2/4\pi = \frac{C^2 m^2}{f_a^2 4\pi}$. From astrophysical bounds $\alpha_a \lesssim 1.0 \times 10^{-22}$ [102]. Specifically, for the coupling of axions to electrons, the dimensionless coupling constant is related to the electron mass and the PQ symmetry breaking scale:

$$g_{ae} = \frac{C_e \cdot m_e}{f_a}. \tag{4.8}$$

In the KSVZ model the axion does not couple to the electron at tree level. However, there is an induced coupling between the axion and electron at the one loop level. The axion electron coupling in the KSVZ is given by the following expression:

$$g_{ae} = \frac{3\alpha^2 N m_e}{2\pi f_a}\left(\frac{E}{N}\ln\frac{f_a}{m_e} - \frac{2}{3}\frac{4+z+w}{1+z+w}\ln\frac{\Lambda}{m_e}\right) \tag{4.9}$$

where $\Lambda \simeq 1$GeV is the QCD confinement scale cutoff [115].

In the DFSZ axion model the axion-electron coupling depends on a parameter $\cos\beta^2$, defined as the ratio of two Higgs vacuum expectation values (VEVs) [78, 115]. The parameter C_e is expressed as:

$$C_e = \frac{\cos\beta^2}{3}, \tag{4.10}$$

assuming there are three families of fermions. Often, the value $\cos\beta = 1$ is used, since β is an arbitrary angle, the expression for the axion electron coupling becomes:

$$g_{ae} = \frac{m_e}{3 \cdot f_a}. \tag{4.11}$$

4.6 Axion-nucleon coupling

The formalism for axion production, as a branch competing with M1 electromagnetic transitions, was developed by Haxton to analyze data from a laboratory search for axions from an M1 transition from a 35 kCi source of ^{65}Zn [35]. The axion-nucleon interaction Lagrangian is as follows:

$$\mathcal{L} = a\bar{\psi}\gamma_5\left(g_{aN}^0\beta + g_{aN}^3\tau_3\right), \tag{4.12}$$

and contains two axion-nucleon coupling constants g_{aN}^0 and g_{aN}^3, the iso-scalar and iso-vector axion-nucleon coupling strengths respectively, β which is a nuclear structure dependent ratio, and τ_3 a Pauli matrix. When considering the flux of solar axions produced via the 14.4 keV M1 transition from the first excited state of ^{57}Fe in the sun; the branching ratio of the decay is given by [35, 74]:

$$\frac{\Gamma_a}{\Gamma_\gamma} = \left(\frac{k_a}{k_\gamma}\right)^3 \frac{1}{2\pi\alpha} \frac{1}{1+\delta^2} \left[\frac{g_{aN}^0\beta + g_{aN}^3}{(\mu_0 - 1/2)\beta + \mu_3 - \eta}\right]^2, \tag{4.13}$$

where μ_0 and μ_3 are the iso-scalar and iso-vector nuclear magnetic moments, δ is the E2/M1 multipole mixing ratio, and η is another nuclear structure dependent ratio. The nuclear structure-dependent quantities parameters η and β are calculated in [35]; $\beta \approx +1$ for an unpaired proton and $\beta \approx -1$ for an unpaired neutron.

In the case of the 14.4 keV de-excitation process of thermally excited ^{57}Fe in the solar core, these values are: $\mu_0 = 0.88$, $\mu_3 = 4.71$, $\delta = 0.002$, $\beta = -1.19$ and $\eta = 0.8$ [74]. The branching ratio at 14.4 keV then becomes:

$$\frac{\Gamma_a}{\Gamma_\gamma} = \left(\frac{k_a}{k_\gamma}\right)^3 1.82\left(-1.19 g_{aN}^0 + g_{aN}^3\right), \tag{4.14}$$

where an effective axion nucleon coupling constant can be defined as:

$$g_{aN}^{eff} \equiv -1.19 g_{aN}^0 + g_{aN}^3. \tag{4.15}$$

The iso-scalar and iso-vector axion-nucleon coupling constants, and therefore the effective axion-nucleon coupling, depends on the invisible axion model being considered. The effective axion nucleon coupling depends on ratios of u-, d-, and s-quark masses, invariant matrix elements for the axial currents of the pion-nucleon couplings, F and D, and a poorly constrained flavor singlet coupling S. The effective axion-nucleon coupling constant, g_{aN}^{eff}, is considered within the constraints of the DFSZ and KSVZ invisible axion models for the standard values: F = 0.48, D = 0.77, S = 0.5, and z = 0.56.

For the KSVZ model, the iso-scalar and iso-vector axion-nucleon couplings are given by eq 4.16 and eq 4.17, respectively. The effective axion-nucleon coupling in the KSVZ model is given in eq 4.18.

$$g_{aN}^{0} = -7.8 \times 10^{-8} \left(\frac{6.2 \times 10^{6}\ GeV}{f_a} \right) \left(\frac{3F - D + 2S}{3} \right) \tag{4.16}$$

$$g_{aN}^{3} = -7.8 \times 10^{-8} \left(\frac{6.2 \times 10^{6}\ GeV}{f_a} \right) \left((D + F) \frac{1 - z}{1 + z} \right) \tag{4.17}$$

$$\begin{aligned} g_{aN}^{eff} &= -1.19 \left(\frac{-2.69 \times 10^{-1}\ GeV}{f_a} \right) + \left(\frac{-1.71 \times 10^{-1}\ GeV}{f_a} \right) \\ &= \left(\frac{1.49 \times 10^{-1}\ GeV}{f_a} \right) \end{aligned} \tag{4.18}$$

In the DFSZ axion model, the axion-nucleon couplings are given by equation 4.19 and equation 4.20, where X_u and X_d are the Peccei-Quinn charges of the up and down quark. These charges have the constraint that the charge values must be positive and obey the relation: $X_u + X_d = 1$. For the qualitative analysis the values of the Peccei-Quinn quark charges are usually taken to be $X_d = 1$ and $X_u = 0$. The effective axion-nucleon coupling in the DFSZ model is given in equation 4.21.

$$\begin{aligned} g_{aN}^{0} &= 5.2 \times 10^{-8} \left(\frac{6.2 \times 10^{6}\ GeV}{f_a} \right) \\ &\times \left(\frac{(3F - D)(X_u - X_d - 3)}{6} + \frac{S(X_u + 2X_d - 3)}{3} \right) \end{aligned} \tag{4.19}$$

$$g_{aN}^{3} = 5.2 \times 10^{-8} \left(\frac{6.2 \times 10^{6}\ GeV}{f_a} \right) \left(\frac{D + F}{2} \right) \left(X_u - X_d - 3 \left(\frac{1 - z}{1 + z} \right) \right) \tag{4.20}$$

$$\begin{aligned} g_{aN}^{eff} &= -1.19 \left(\frac{-1.98 \times 10^{-1}\ GeV}{f_a} \right) + \left(\frac{-3.72 \times 10^{-1}\ GeV}{f_a} \right) \\ g_{aN}^{eff} &= \left(\frac{-1.36 \times 10^{-1}\ GeV}{f_a} \right) \end{aligned} \tag{4.21}$$

4.7 Solar axions

If axions exist, they are copiously produced in the solar plasma through a number of processes. These processes include Primakoff, axio-deexcitation, axio-recombination (in atoms), Bremstrahlung, Compton, and low-lying nuclear magnetic dipole transitions. The Feynman diagrams for the Primakoff and Atomic-Bremstrahlung-Compton (ABC) reactions, from reference [105], are shown in figure 4.4.

The Primakoff process depends on the strength of axion-photon coupling $g_{a\gamma}$, while the ABC reactions depend on the strength of the axion-electron coupling g_{ae}. The probability to generate and detect axions depends on the degree to which axions couple to normal matter; namely the coupling to photons, electrons, and nucleons (quarks and gluons). The rate at which axions are produced is proportional to the square of the axion coupling involved in the process. In other words, the flux of the axions created from ABC reactions a proportional to g_{ae}^2 while the flux of the axions generated from the Primakoff process in proportional to $g_{a\gamma}^2$.

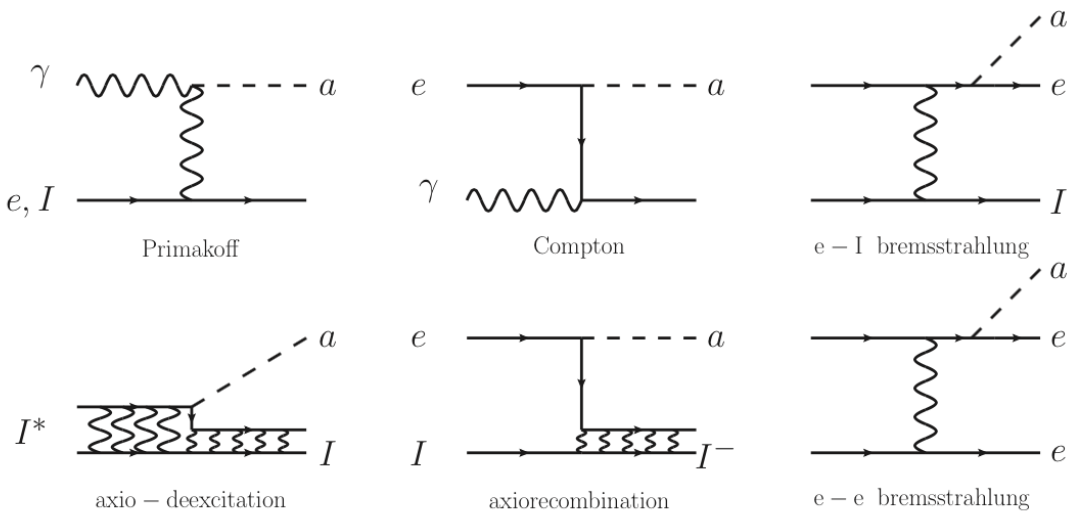

Figure 4.4: Feynman diagrams of Primakoff and Atomic-Bremstrahlung-Compton (ABC) reactions [105].

The axion flux on the surface of the Earth from the Primakoff process is based on a standard solar model, and approximated in [102]:

$$\frac{d\phi_a}{dE} = g_{10}^2 \cdot 6.0 \times 10^{10}\ cm^{-2}\ s^{-1}\ keV^{-1}\ E^{2.481} e^{-E/1.205} \tag{4.22}$$

where E is the energy in keV and $g_{10} \equiv g_{a\gamma}/(10^{-10}\ GeV^{-1})$. The distribution of the Primakoff flux has a maximum value at 3.0 keV and an average energy of 4.2 keV.

Often solar axions produced via the Primakoff process are searched for using the axion helioscope technique [112]. This technique relies on the inverse Primakoff technique where an axion converts into a photon in a macroscopic magnetic field, and is detected at the far end of the detector (out of the magnetic field). Early helioscope searches were performed in Brookhaven [87] and Tokyo [76, 91], but the best experimental bound on axion and axion like particles (ALPs) coupling to photons is provided by the results of the CAST experiment [34].

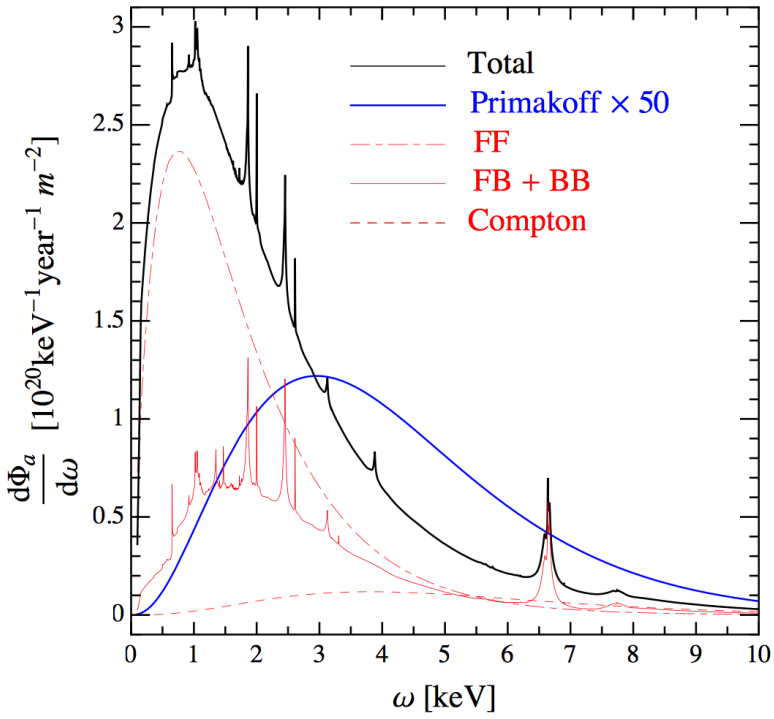

Figure 4.5: Solar axion flux calculated from Primakoff and Atomic-Bremstrahlung-Compton (ABC) reactions [105].

Table 4.2: Relevant X-ray energies for solar axions.

Element	$K_{\alpha 2}$ [eV]	$K_{\alpha 1}$ [eV]
Si	1739.394(34)	1739.985(19)
P	2012.70(48)	2013.68(48)
S	2306.700(38)	2307.885(34)
Cl	2620.846(39)	2622.440(39)
K	3311.1956(60)	3313.9476(50)
Ca	3688.128(49)	3691.719(49)
Fe	6391.0264(99)	6404.0062(99)

The expected flux of solar axions produced via ABC reactions were calculated by Javier Redondo [105] from available libraries of monochromatic photon radiative opacities. His calculated fluxes are ∼30% larger than previous estimates due to atomic re-combination and de-excitation. Figure 4.5 shows the total expected flux of axions in the 0 - 10 keV range for an assumed dimensionless axion-electron coupling of $g_{ae} = 10^{-13}$ and an assumed axion-photon coupling of $g_{a\gamma} = 10^{-12}\ GeV^{-1}$. The predicted solar axion flux is only significant at low energies, on the order of a few keV. The flux rises quickly, peaking at $\sim$ 1 keV, and then drops rapidly over the following 2 -3 keV interval. While the total flux from all production mechanisms is considerable, the axio-deexcitation and axio-recombination contribution is of particular interest as it adds structure in the otherwise smooth spectrum. The most relevant X-ray energies that contribute to the solar axion flux are given in table 4.2.

4.8 Axioelectric effect and absorption cross section

The axioelectric effect is the analog of the photoelectric effect in which an axion interacts with an electron and is absorbed (axioelectric absorption), $A+Z \rightarrow Z^{*}+e^{-}$. In our case, the interaction energy of this process is absorbed by, and measured with, a TeO_2 bolometer. As the process is analogous to the photoelectric effect, the axioelectric absorption cross section $\sigma_{ae}(E)$ is not only a function of energy E, but proportional to photoelectric cross section $\sigma_{pe}(E)$, and described by the general

formula in equation 4.23 [53, 54]:

$$\sigma_{ae}(E) = \frac{g_{ae}^2}{\beta} \frac{3E^2}{16\pi\alpha m_e^2 c^4} \left(1 - \frac{\beta^{2/3}}{3}\right) \sigma_{pe}(E), \tag{4.23}$$

where g_{ae} is the axion-electron coupling constant, α is the fine-structure constant, β is the axion velocity relative to the speed of light c, and m_e is the mass of an electron. In the relativistic limit ($\beta \to 1$), the axioelectric cross section, equation (4.24) becomes:

$$\sigma_{ae}(E) = g_{ae}^2 E^2 (2.09 \times 10^{-5}) \sigma_{pe}(E). \tag{4.24}$$

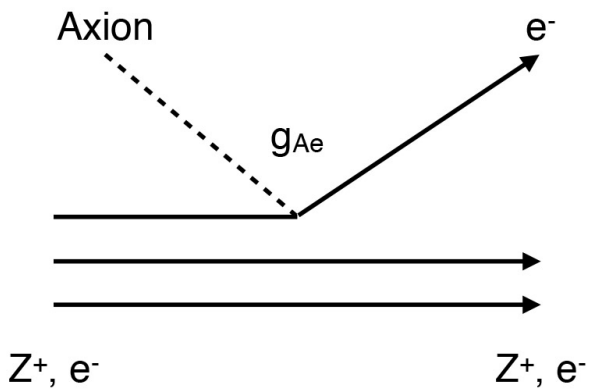

Figure 4.6: Diagram of the axio-electric effect (analog of the photoelectric effect) where an axion interacts with a bound electron, is absorbed, and ejects an electron [36].

Chapter 5

Experimental search for solar axions

5.1 Introduction

In the following analysis, CUORE style TeO_2 bolometers are used to search for a solar axion signal at an energy of 6.4 keV, via the axioelectric effect, produced from the atomic de-excitation of Fe atoms in the sun. The energy of this X-ray is given in table 4.2. The axioelectric effect is also used to search for an axion signal generated from the 14.4 keV M1 transition of thermally excited ^{57}Fe atom in the solar plasma. Unfortunately, CUORE-0 has a higher energy threshold than expected, around 10 keV, so data from the CUORICINO experiment, as well as CUORE Crystal Validation Run 2 (CCVR2), were analyzed in the search for solar axion at 6.4 keV while the data from CUORE-0 was used to search for the 14.4 keV axion. As the detection technique for both axion searches relies on the axion-electron coupling, only the DFSZ axion model will be considered, since in this model the axion couples to electron at the tree level.

The motivation of the work discussed in this chapter was to study the interaction of axions produced in the sun, using an array of TeO_2 bolometers operated underground at a temperature of $\sim 10\ mK$. Two different mechanisms of solar axion production are considered; both axion searches rely on the axioelectric effect in TeO_2 bolometers for detection. These bolometers are $5 \times 5 \times 5\ cm^3$ in dimension and operated in $^3He/^4He$ dilution refrigerator at $\sim 10\ mK$. It should be pointed out, however, that a few of the CUORICINO crystals were of smaller dimensions. Each of the CUORE

crystal validation runs (CCVR) were operated in the CUORE R&D cryostat in Hall C of LNGS. The other two experiments, CUORICINO and CUORE-0, were operated in a similar dilution refrigerator with a slightly larger experimental chamber in Hall A of LNGS. A total of 43.65 $kg \cdot days$ of CCVR2 data were analyzed using the newly developed (at the time) low-energy trigger optimized to lower the energy threshold of the experiment [13]. A peak of unknown origin was observed in the low-energy CCVR2 spectrum at 4.7 keV. This peak has not yet been identified as one from a known decay. Since CCVR2 was the first experiment implementing the optimum trigger, the final month or so of raw data from the CUORICINO experiment was reprocessed with the optimum trigger to check if the unidentified 4.7 keV peak was also present. It was, and the event rate was observed to be constant with time.

Two different axion searches were carried out using three different sets of low-energy data. What makes these data different from the standard data is that they are processed by an additional software trigger, called CUORE Optimum Trigger (OT), developed to lower the energy threshold [55]. The trigger is based on the matched filter algorithm [71, 101] and also provides a pulse shape parameter to suppress false signals generated by detector vibrations and noise from the electronics. The general idea was to search the available experimental data for a peak at expected solar axion energies of 6.4 keV and 14.4 keV. While the physical processes that produce these two axion lines are very different, as discussed in chapter 4, the analysis is rather straight forward and essentially identical. The procedure is as follows: determine the local detector energy resolution, fit each spectrum with a background function, and then search for a gaussian peak at the expected axion energy.

5.2 Low-Energy Spectra

The low-energy data from three experiments were used to search for solar axions: CUORE Crystal Validation Run (CCVR) 2, CUORICINO, and CUORE-0. Each

CCVR experiment was a short-time, four bolometer experiment performed as a quality assurance test for each shipment of TeO_2 crystals delivered to LNGS. The four crystals were selected at random, mounted, and tested in the CUORE R&D cryostat in Hall C. The total TeO_2 exposure of the CCVR2 experiment was 43.65 $kg \cdot days$, while the CUORICINO data had a total TeO_2 exposure of 62.7 $kg \cdot days$. The total exposure and detector threshold, for each experiment, is given in table 5.1.

Table 5.1: Total exposure of TeO_2 in $[kg \cdot d]$ and detector energy threshold in $[keV]$ by experiment.

Data set	Exposure [kg d]	Threshold [keV]
CCVR2	43.65	3.0
CUORICINO	62.7	3.0
Combined	106.35	3.0
CUORE-0 (11 Chs.)	1825.0	10.0
CUORE-0 (22 Chs.)	3376.25	10.0

The low energy spectra of CCVR2 and CUORICINO are very similar from the threshold of the detector (∼3 keV) to ∼28 keV. The number of counts is substantial near the detector threshold energy (∼3 keV) but decreases rapidly over the next few keV. A physical peak in both spectra can be seen from approximately 4 keV to 5.5 keV, with the peak centered at approximately 4.7 keV. Above the peak at 4.7 keV, both spectra continue to slowly and smoothly decrease from 5.5 keV to 40 keV. Over the entire energy range, (3 - 40)-keV, both the CCVR2 (figure 5.1) and CUORICINO (5.2) spectra appear to follow an exponentially decreasing function with a gaussian peak at approximately 4.7 keV. The peak at 30.49 keV in the CCVR2 spectrum is an Sb X-ray due to cosmogenic activation of tellurium atoms during shipment to LNGS. The region between detector threshold and this peak is a window large enough to search for solar axions at the expected energies of 6.4 keV and 14.4 keV. The low energy detector threshold for CUORE-0 is 10 keV, higher than CCVR2 and CUORICINO, making the 6.4 keV axion search impossible. Therefore, since the exposure is low compared to CUORE-0, to obtain the best possible bound on

the 6.4 keV axion peak, the CCVR2 and CUORICINO spectra are combined for a total TeO_2 exposure of 106.35 $kg \cdot days$. The CCVR2, CUORICINO, and combined CCVR2 and CUORICINO spectra are shown in figure 5.3. In figure 5.4 all three spectra are plotted together for comparison.

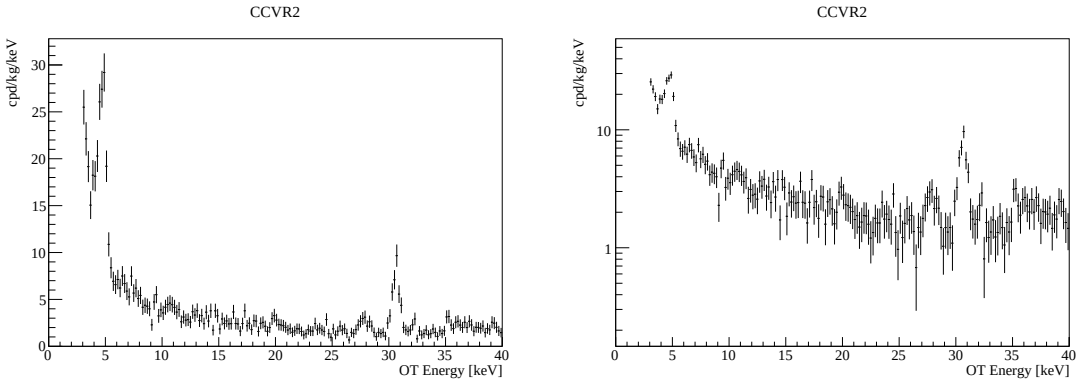

(a) Linear (b) Semi-Log

Figure 5.1: CCVR2 low-energy spectrum from 0 - 40 keV in [c/d/kg/keV].

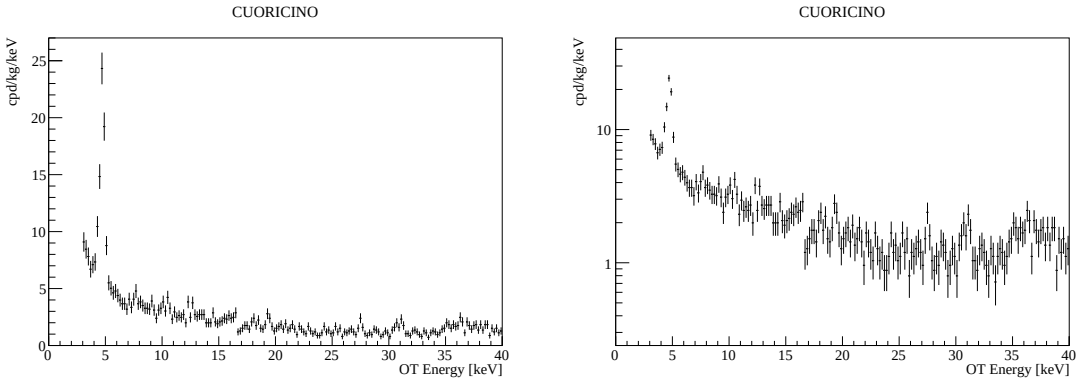

(a) Linear (b) Semi-Log

Figure 5.2: CUORICINO low-energy spectrum from 0 - 40 keV in [c/d/kg/keV].

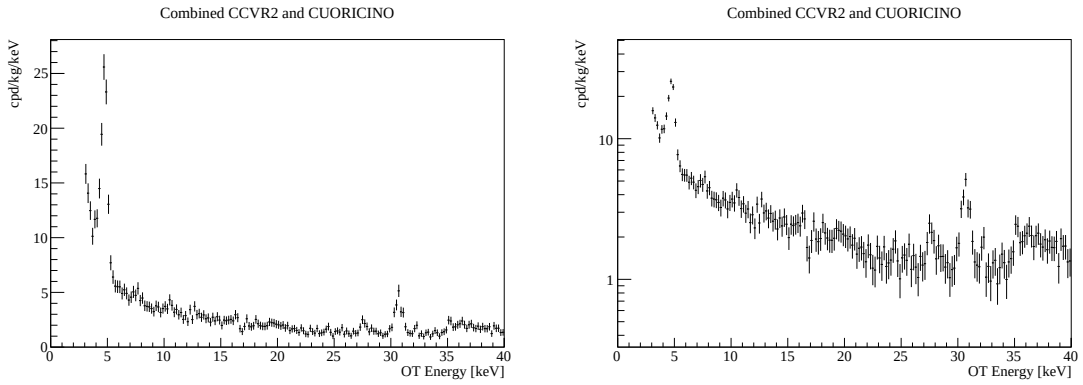

(a) Linear (b) Semi-Log

Figure 5.3: Combined CCVR2 and CUORICINO low-energy spectra from 0 - 40 keV in [c/d/kg/keV].

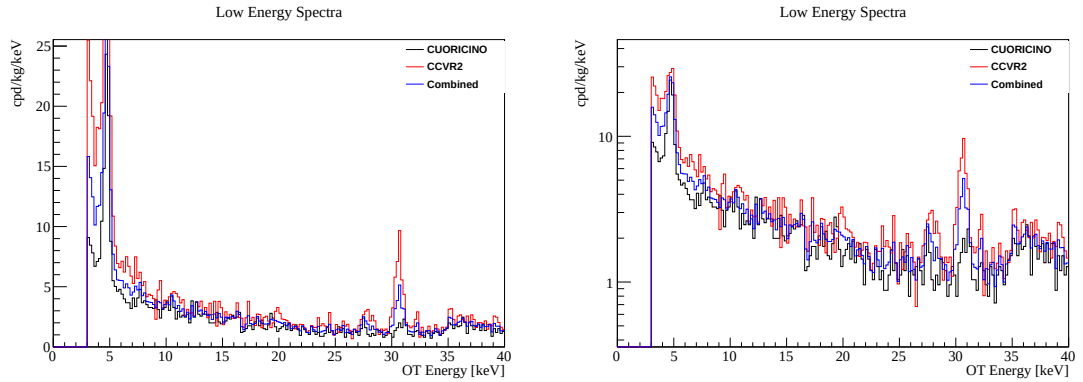

(a) Linear (b) Semi-Log

Figure 5.4: CCVR2, CUORICINO, and the combined low-energy spectra from 0 - 40 keV in [c/d/kg/keV].

For CUORE-0, two different data sets are used, one with 22 channels and one with 11 channels, the only difference being the total exposure of TeO_2. The CUORE-0 low energy spectra, shown in figure 5.5, have exposures of 9.25 $kg \cdot y$ of TeO_2 and 5.0 $kg \cdot y$ of TeO_2 for the 22-channel and 11-channel data sets respectively. Above 10 keV, the background rate of CUORE-0 was lower than that of CUORICINO and CCVR2. Below this energy, the event rate of CUORE-0 increases and over takes the rates of the previous experiments, hiding the peak at 4.7 keV.

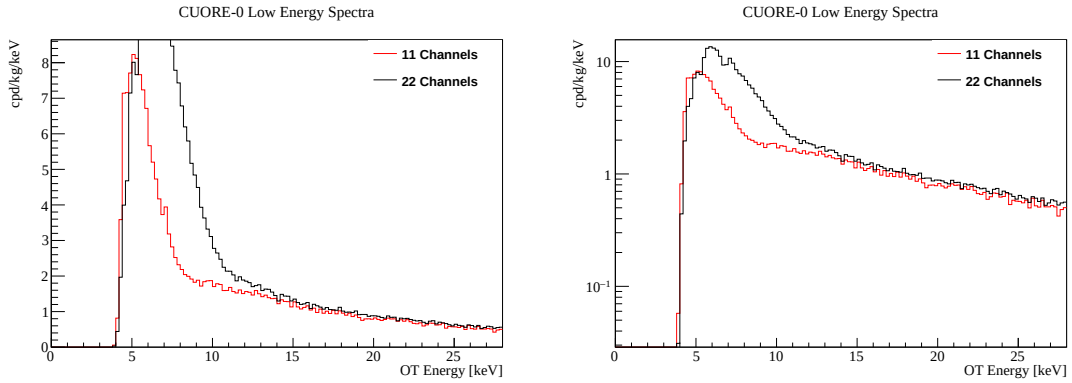

(a) Linear (b) Semi-Log

Figure 5.5: CUORE-0 11-channel and 22-channel low-energy spectra from 0 - 28 keV in [c/d/kg/keV].

5.3 The determination of the local energy resolution

The first step of the analysis was to determine the local energy resolution for each spectrum. As mentioned previously, the 4.7 keV peak is the most prominent feature in the low-energy spectra of the CCVR2 and CUORICINO data. While the origin of this peak is still unknown, we take advantage of its existence by using it to establish the (local) energy resolution of the detector. An exponential function and a gaussian, with mean energy at approximately 4.7 keV, are used to fit the spectrum in the range of 4.7 ± 1 keV. This model is used for all experimental data to obtain the exact location of the gaussian, $\mathrm{E}_{4.7keV}$, and the standard deviation, σ. A common method to compare the energy resolutions of two different detectors is to measure the full width of the gaussian at half the maximum amplitude, also known as full width at half max (FWHM). The full width at half max is directly related to the standard deviation σ of the gaussian fit given by the following expression: $FWHM = 2\sqrt{2\ln 2}\ \sigma \approx 2.355\ \sigma$. The fit of the 4.7 keV peak for both the CCVR2 and CUORICINO spectra is shown in figures 5.6 and 5.7 respectively. The combined CCVR2 and CUORICINO fit of the 4.7 keV peak is shown in figure 5.8. Table 5.2 contains the energy, standard deviation, and the FWHM of the 4.7 keV peak for each data set.

Table 5.2: Results of the fits of the 4.7 keV peak for CCVR2, CUORICINO, and their combined spectra

Data set	Energy [keV]	Std. Dev. [keV]	FWHM [keV]
CCVR2	4.73373	0.33152	0.780729
CUORICINO	4.72948	0.212171	0.499662
Combined	4.73358	0.261139	0.614983

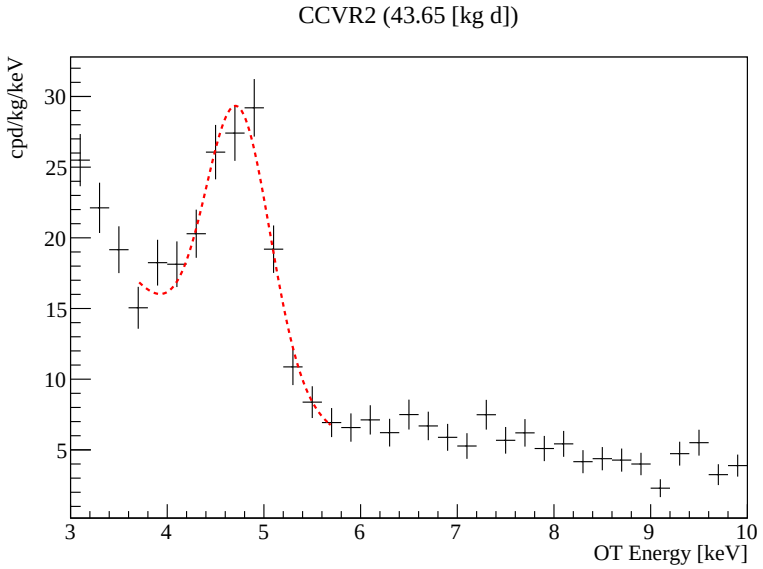

Figure 5.6: Result of the fit of the 4.7 keV peak in the CCVR2 spectrum.

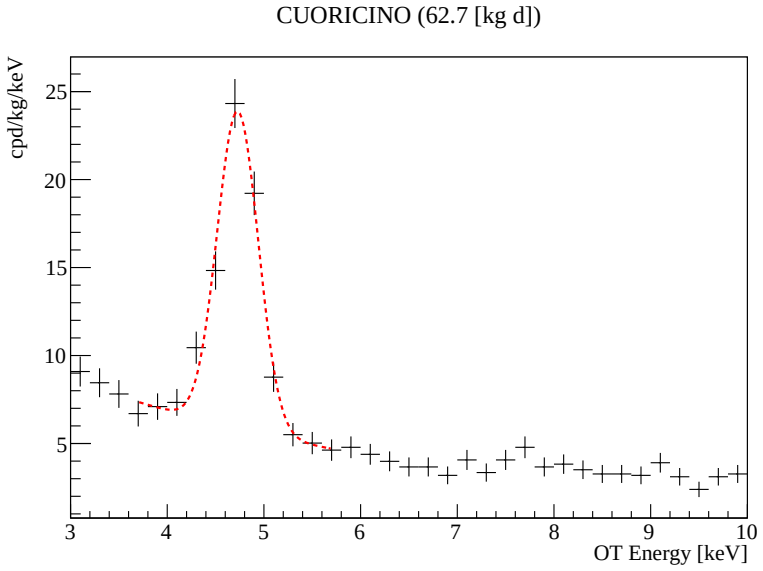

Figure 5.7: Result of the fit of the 4.7 keV peak in the CUORICINO spectrum.

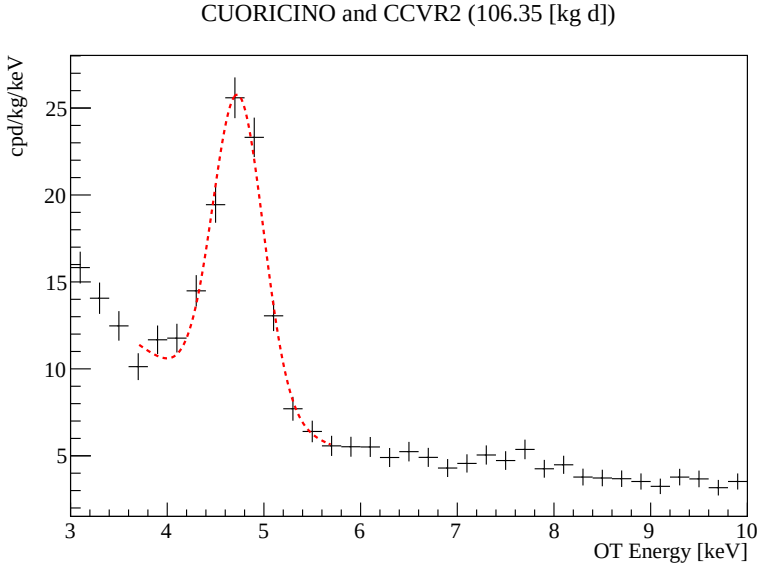

Figure 5.8: Result of the fit of the 4.7 keV peak in the combined CCVR2 & CUORICINO spectrum.

The procedure to determine local energy resolution for the CUORE-0 low-energy data differs from the one used for the previous experiments. Since the CUORE-0 low energy data are "noisier" than those of previous experiments, and with an energy threshold at ∼10 keV, we are unable to see the 4.7 keV peak, which requires another method to determine the local energy resolution of the detector. Instead, the CUORE-0 low-energy (M2) calibration data (figure 5.9 and 5.10) are used to fit the X-ray peak at 27.38 keV. The term M2 refers to multiplicity 2 events, when two bolometers trigger events within a narrow time frame (100 ms). A flat background and a gaussian, with mean energy at approximately 27.38 keV, are used to fit the spectrum in the 25 - 30 keV range, as shown in figure 5.11. For the 22 channel spectrum, it is possible to fit the two nearby peaks, at 27.38 keV and 31.11 keV, with two gaussian functions with the same variance and with a flat background in the 22 to 36 keV region (figure 5.12) to obtain the local energy resolution. However the second peak is not as well defined as the first, so the energy resolution obtained when fitting the double peak is larger (2.26 keV compared to 1.93 keV FWHM) than that obtained by fitting only the single peak at 27 keV. The energy resolution used from

this point on, for both the 11 channel and 22 channel CUORE-0 spectra, will be those obtained with a single peak fit. Table 5.3 contains the energy, standard deviation, and the FWHM of the 27.38 keV peak for each CUORE-0 data set.

Table 5.3: CUORE-0 calibration (M2) spectrum fit results of 27.38 keV peak.

Data set	Energy [keV]	Std. Dev. [keV]	FWHM [keV]
CUORE-0 (11 Chan.)	27.6222	0.682734	1.60784
CUORE-0 (22 Chan.)	27.5137	0.818378	1.92728

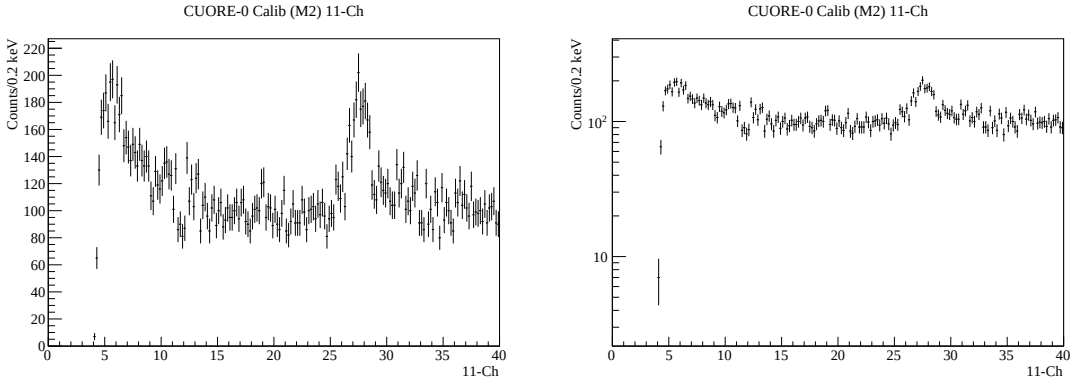

(a) Linear (b) Semi-Log

Figure 5.9: CUORE-0 (M2) low-energy calibration data from 0 - 40 keV for the 11 channel data set.

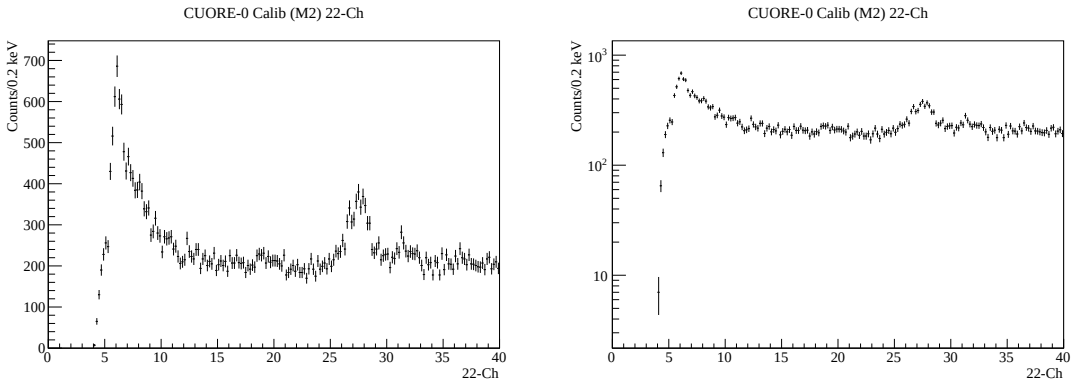

(a) Linear (b) Semi-Log

Figure 5.10: CUORE-0 (M2) low-energy calibration data from 0 - 40 keV for the 22 channel data set.

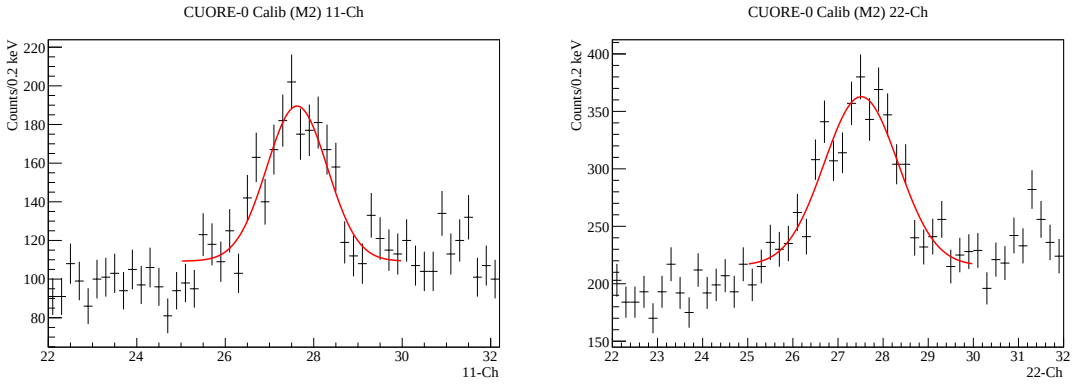

(a) (b)

Figure 5.11: CUORE-0 (M2) 27.38 keV peak for (a) the 11 channel and (b) the 22 channel spectra.

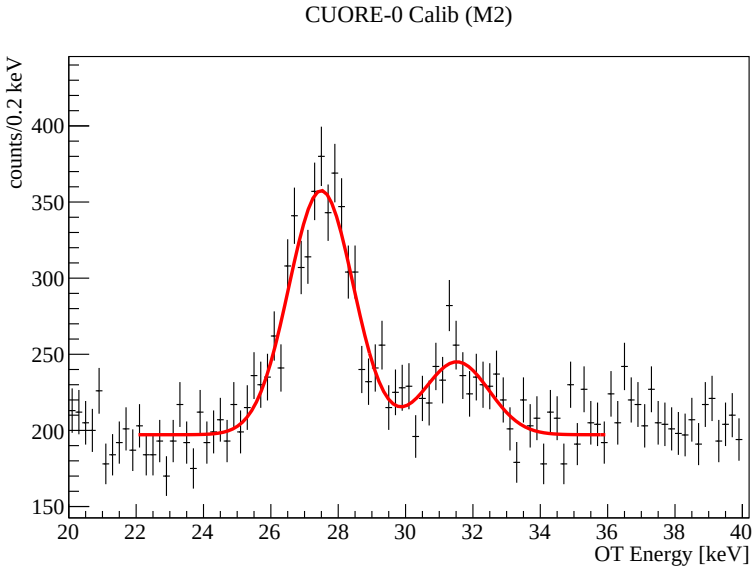

Figure 5.12: Result of the fits to 27.38 and 31.11 keV peaks in CUORE-0 (M2) calibration spectrum.

5.4 Background Models

Once the detector energy resolution was established, a background fit was preformed in the axion-energy region of interest. In the case of CCVR2 and CUORICINO, a single background function was used for both the 6.4 and 14.4 keV axion searches searches. A function composed of an exponential and a gaussian were used to fit the CCVR2 and CUORICINO data, as well as the combined CCVR2 & CUORICINO

spectra in the (5-18)-keV range. For the most part, the background in this region is fit by an exponential function; however, since the 6.4 keV axion peak is so close to the tail of the 4.7 keV peak, a gaussian is also included in the fit. The energy, standard deviation, and amplitude of the gaussian are fixed using the fit parameters from the aforementioned local 4.7 keV peak, and only the exponential parameters are free. This leads to a better fit in the nearby 6.4 keV region, and affects very little the fit in the 14.4 keV region. Previously, the CCVR2 and CUORICINO background (5-18)-keV function was composed of two exponential functions as well as the fixed gaussian functions, but the results of the fit are almost identical to the fit using a single exponential function and a fixed gaussian function. Therefore, for simplicity, only one exponential was used to model the background. Since CUORE-0 is only sensitive to the 14.4 keV axion due to a higher detector energy threshold, a single exponential is used to fit the background in the (11-18)-keV range.

5.5 Experimental search for solar axions at 6.4 and 14.4 keV

To determine the number of axion events that could be hidden in the background, a likelihood function was computed comprising the previously established background function (with all parameters fixed), along with an assumed gaussian function at an energy of 6.4 keV or 14.4 keV. In the case of CCVR2 and CUORICINO, the standard deviation of the axion signal was determined from the fit of the 4.7 keV peak. For CUORE-0, the standard deviation of the axion signal is determined from the fit of the 27.38 keV peak in the M2 spectrum of the calibration data. These axion searches were preformed independently of one another, and in both cases only the amplitude of the assumed axion peak is free. The counts in the 6.4 keV peak were used to place a bound on the dimensionless axion electron coupling constant g_{ae}. The counts in the 14.4 keV peak were used to place a bound on the product of the effective axion-nucleon coupling and axion-electron coupling constant $|g_{aN}^{eff} \times g_{ae}|$.

The likelihood analysis used in this work is based on a Monte-Carlo procedure. A series of new spectra is generated by choosing new values for each experimental data point by fluctuating its value using its Poisson probability distribution. This was repeated typically 10,000 times. The best-fit values from fitting each of the 10,000 trial spectra were computed. The plot of the number of times a best fit value occurs versus the best-fit values, is in fact a numerically computed maximum-likelihood (MLH) function. From this function one can compute the most probable value under a peak, for example, and confidence levels on central values as well as the confidence values of the limits. For each random "experiment," a fit of the simulated axion peak was performed, while the background function remained identical to the fit of the original spectrum. For each random background iteration, after the fit of the axion peak, the gaussian amplitude and the axion rate are added to their respective histograms. The axion rate is found by integrating both the axion likelihood function and the fitted background, about the axion peak energy, and taking the difference.

At the end of each Monte Carlo cycle, the signal amplitude and axion rate distributions are then fit with gaussians to extract the mean and standard deviation. The mean value from the gaussian fit is the estimated maximum likelihood value, and the standard deviation is used to place upper bounds on the amplitude and rate to a desired confidence level. In this analysis a 90% CL and 95% CL upper bounds are established for comparison with other experiments. Using the gaussian amplitudes from the MLH functions, 90% CL, and 95% CL, bounds are plotted together with the original energy spectrum and the background fit. The results of the Monte Carlo analysis are shown in the tables below.

6.4 keV axion search

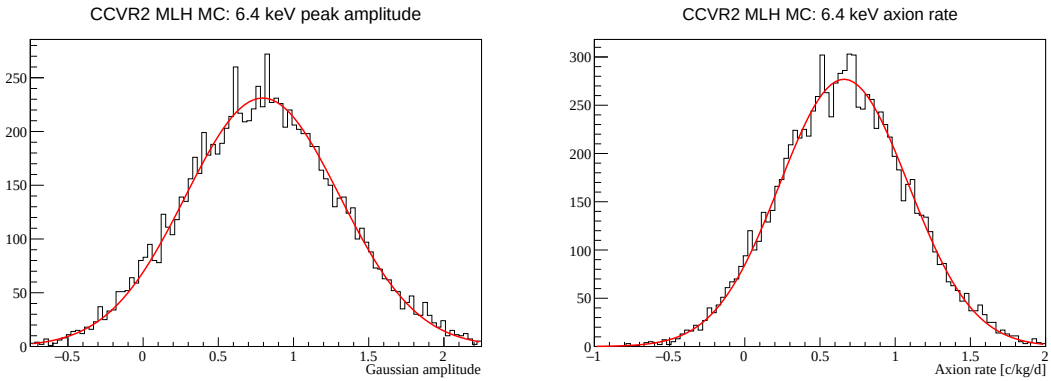

(a) Amplitude (b) Rate

Figure 5.13: Monte Carlo likelihood distribution of the 6.4 keV axion amplitude and rate [c/d/kg] for CCVR2. See the spectrum in figure 5.14.

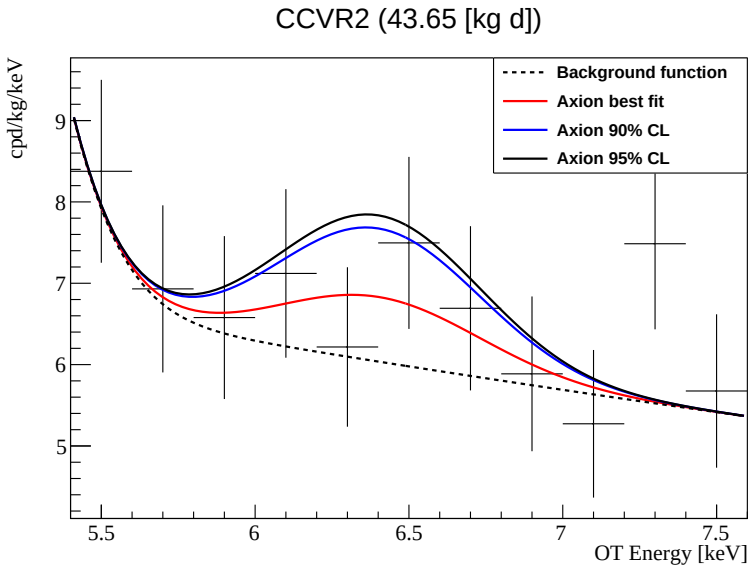

Figure 5.14: CCVR2 best fit (MLH) of the assumed 6.4 keV peak with 90% CL and 95% CL gaussian peaks.

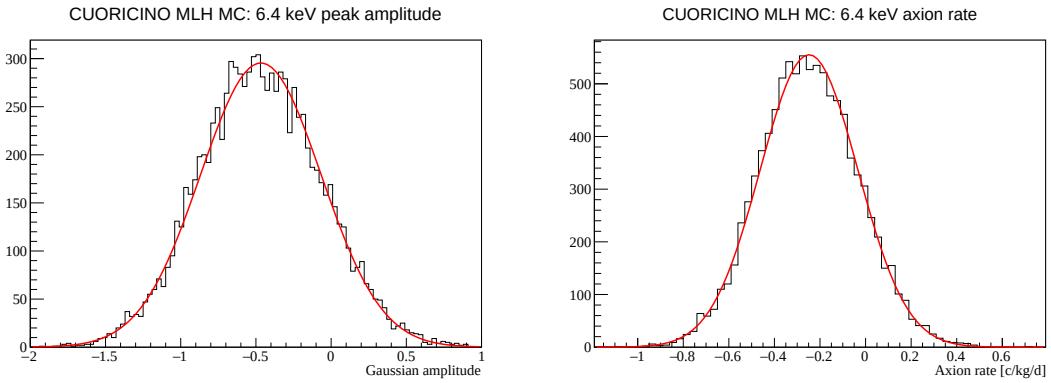

(a) Amplitude (b) Rate

Figure 5.15: Monte Carlo likelihood distribution of the 6.4 keV axion amplitude and rate [c/d/kg] for CUORICINO. See the spectrum in figure 5.16.

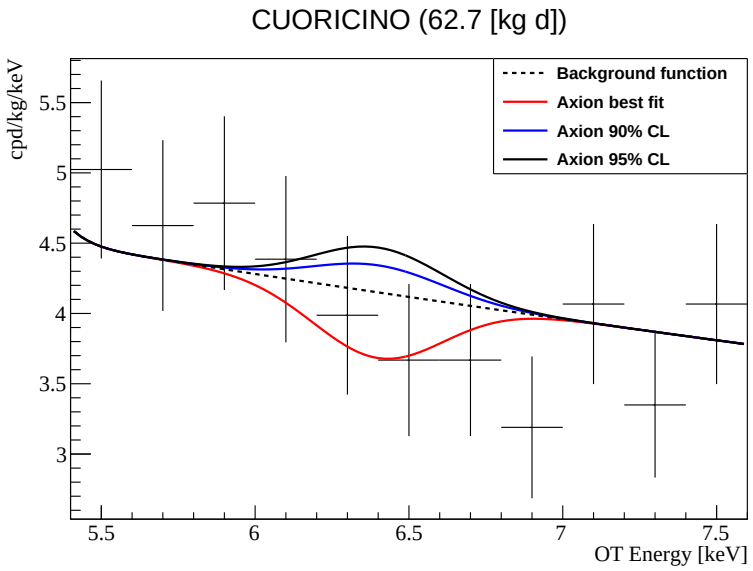

Figure 5.16: CUORICINO best fit (MLH) of the assumed 6.4 keV peak with 90% CL and 95% CL gaussian peaks.

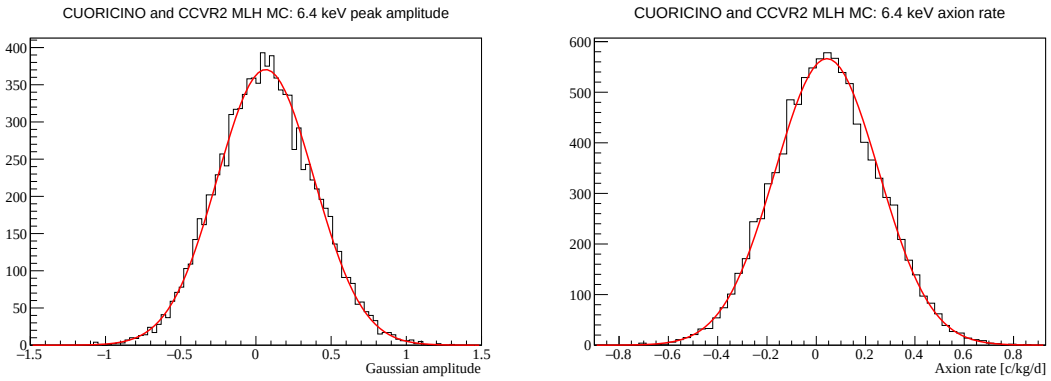

(a) Amplitude (b) Rate

Figure 5.17: Monte Carlo likelihood distribution of the 6.4 keV axion amplitude and rate [c/d/kg] for CUORICINO & CCVR2. See the spectrum in figure 5.18.

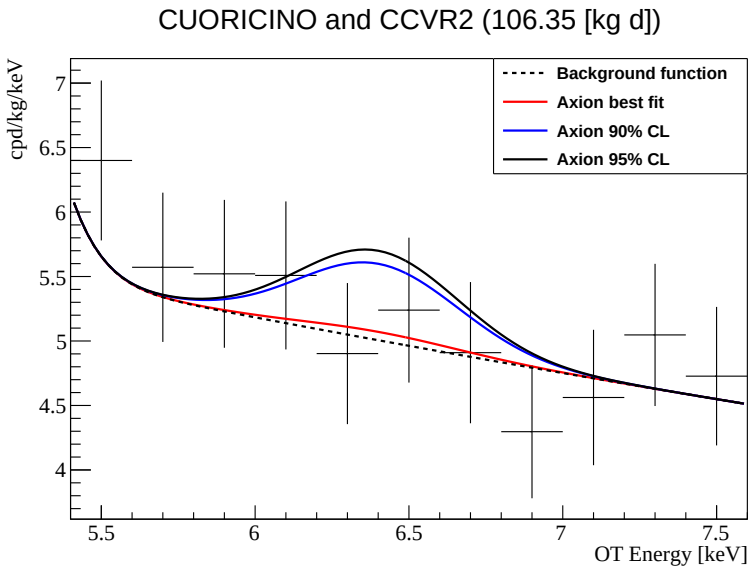

Figure 5.18: Combined CCVR2 and CUORICINO best fit (MLH) of the assumed 6.4 keV peak with 90% and 95% gaussian peaks.

Table 5.4: Monte Carlo MLH bounds for gaussian amplitude of the 6.4 keV axion.

Data set	Mean	CL 90%	CL 95%	Std. Dev.
CCVR2	0.794765	1.63662	1.79783	0.511767
CUORICINO	-0.467318	0.192639	0.319013	0.401189
Combined	0.064768	0.592899	0.694031	0.321052

Table 5.5: Monte Carlo MLH bounds for the 6.4 keV axion rate [c/kg/d].

Data set	Mean	CL 90%	CL 95%	Std. Dev.
CCVR2	0.659918	1.36488	1.49987	0.428548
CUORICINO	-0.248128	0.104633	0.172183	0.214444
Combined	0.043151	0.389399	0.455702	0.210485

14.4 keV axion search

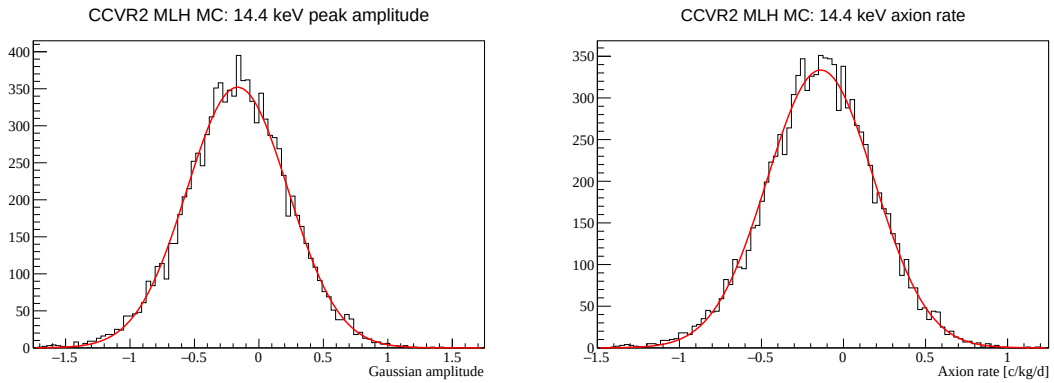

(a) Amplitude (b) Rate

Figure 5.19: Monte Carlo likelihood distribution of the 14.4 keV axion amplitude and rate [c/d/kg] for CCVR2. See the spectrum in figure 5.20.

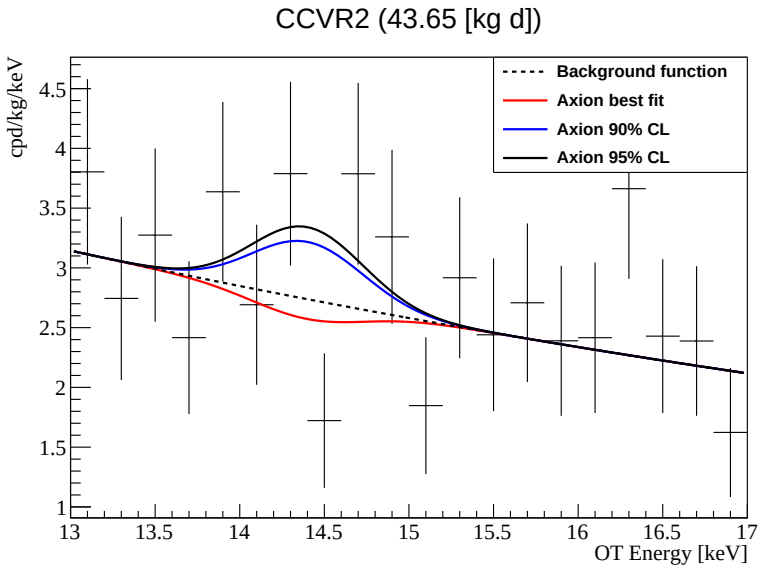

Figure 5.20: CCVR2 best fit of the assumed 14.4 keV peak with 90% CL and 95% CL gaussian peaks.

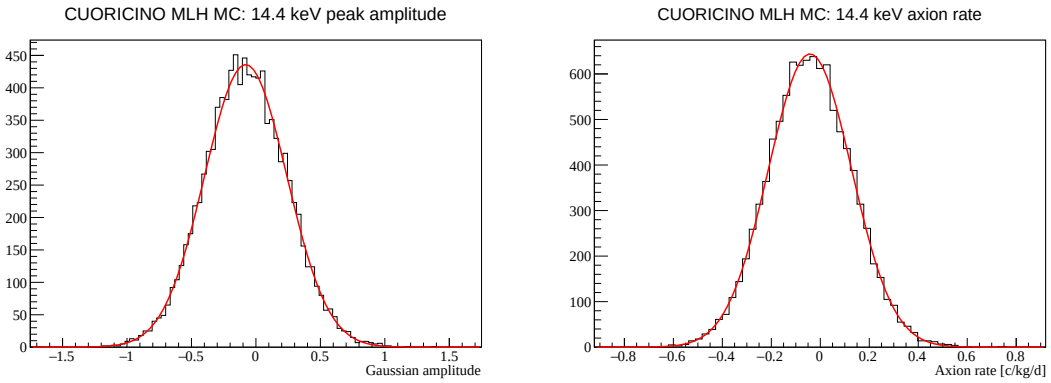

(a) Amplitude (b) Rate

Figure 5.21: Monte Carlo likelihood distribution of the 14.4 keV axion amplitude and rate [c/d/kg] for CUORICINO. See the spectrum in figure 5.22.

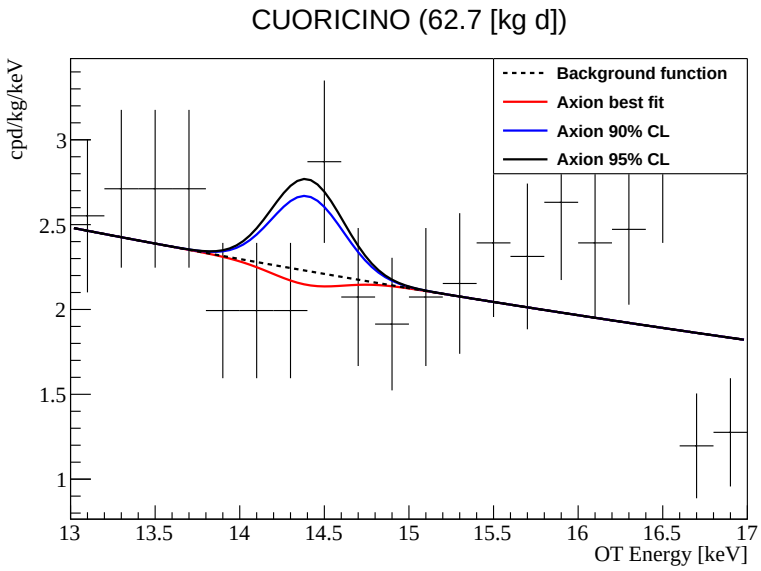

Figure 5.22: CUORICINO best fit of the assumed 14.4 keV peak with 90% CL and 95% CL gaussian peaks.

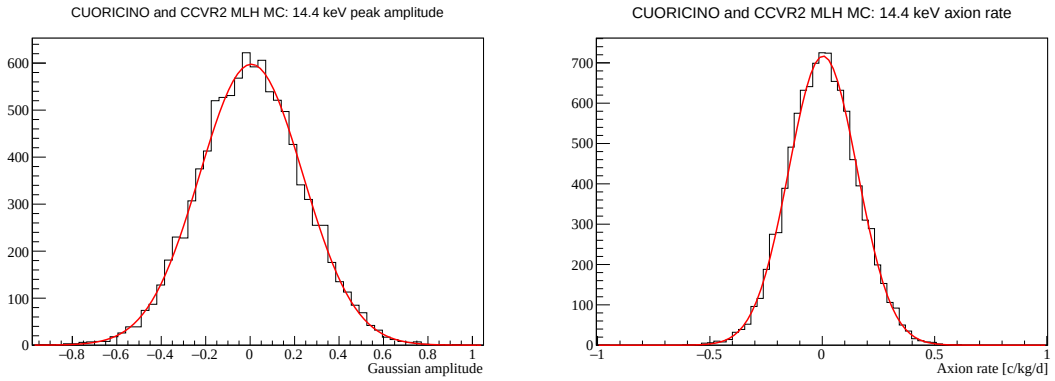

(a) Amplitude (b) Rate

Figure 5.23: Monte Carlo likelihood distribution of the 14.4 keV axion amplitude and rate [c/d/kg] for CUORICINO & CCVR2. See the spectrum in figure 5.24.

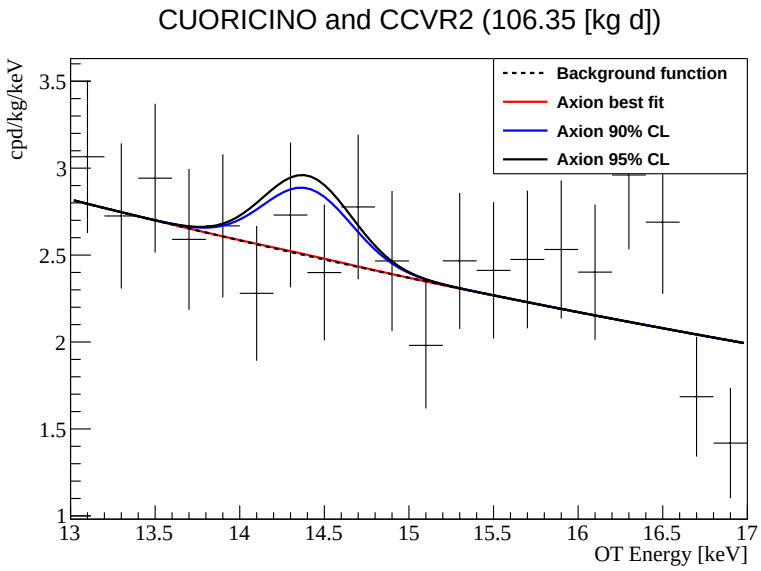

Figure 5.24: Combined CCVR2 and CUORICINO best fit of the assumed 14.4 keV peak with 90% CL and 95% CL gaussian peaks.

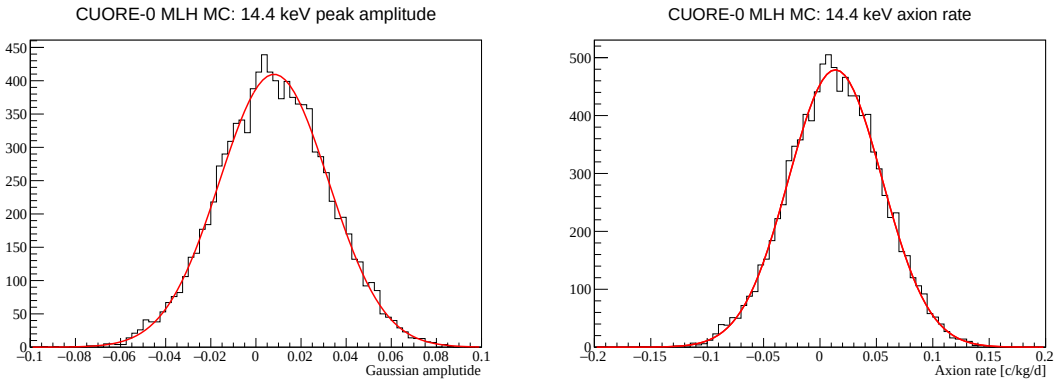

(a) Amplitude (b) Rate

Figure 5.25: Monte Carlo likelihood distribution of the 14.4 keV axion amplitude and rate [c/d/kg] for CUORE-0 (11-channels).

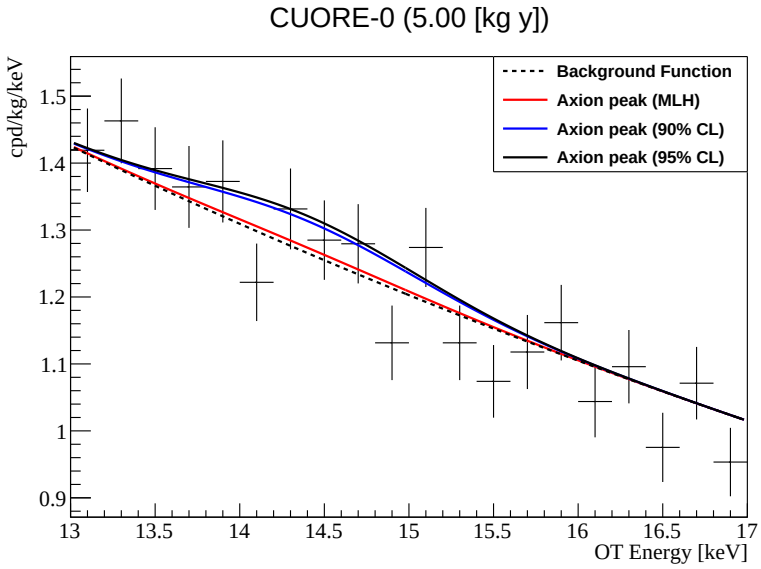

Figure 5.26: CUORE-0 (11-Ch) best fit of the assumed 14.4 keV peak with 90% CL and 95% CL gaussian peaks.

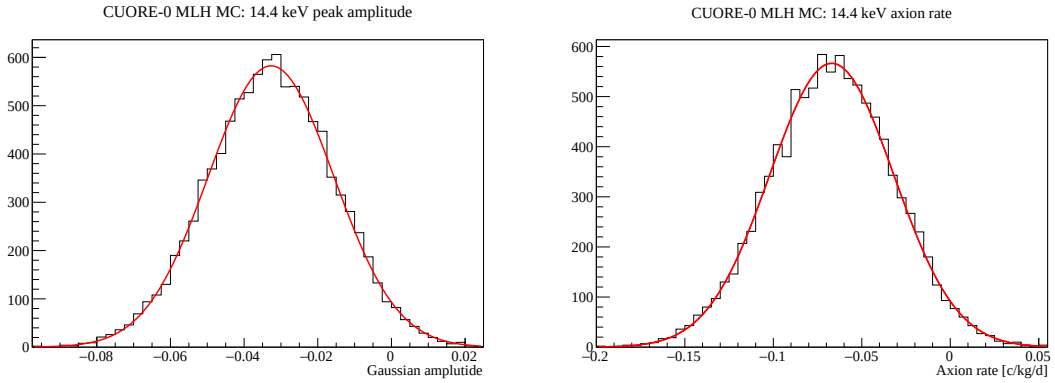

(a) Amplitude (b) Rate

Figure 5.27: Monte Carlo likelihood distribution of the 14.4 keV axion amplitude and rate [c/d/kg] for CUORE-0 (22-channels).

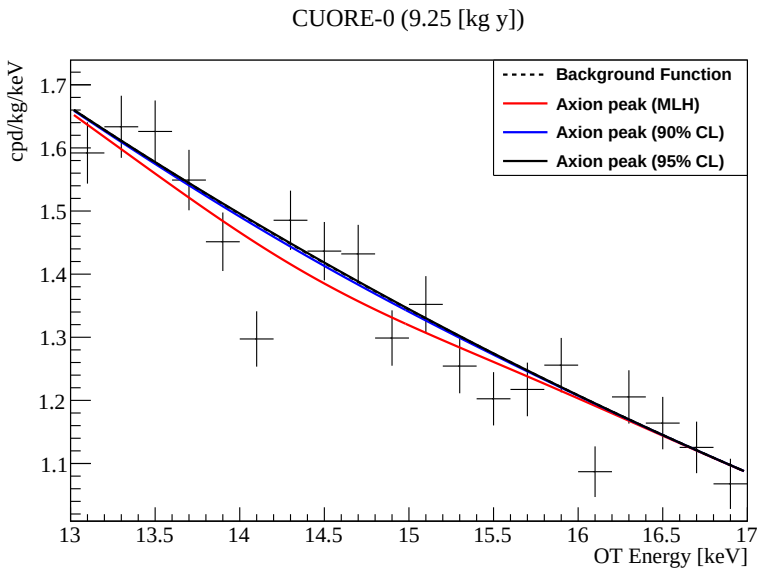

Figure 5.28: CUORE-0 (22-Ch) best fit of the assumed 14.4 keV peak with 90% CL and 95% CL gaussian peaks.

Table 5.6: Monte Carlo MLH bounds for the 14.4 keV axion gaussian amplitude.

Data set	Mean	90% CL	95% CL	Std. Dev.
CCVR2	-0.166183	0.479429	0.603056	0.392469
CUORICINO	-0.0792775	0.445467	0.54595	0.318994
Combined	0.00519769	0.387843	0.461115	0.232611
CUORE-0 (11-Ch)	0.00804026	0.0479025	0.0555357	0.0242324
CUORE-0 (22-Ch)	-0.0326892	-0.00461656	0.000759053	0.0170654

Table 5.7: Monte Carlo MLH bounds on the 14.4 keV axion rate [c/kg/d].

Data set	Mean	90% CL	95% CL	Std. Dev.
CCVR2	-0.139488	0.395826	0.498333	0.325419
CUORICINO	-0.0420365	0.237476	0.291	0.169917
Combined	0.00337636	0.2541	0.302111	0.152416
CUORE-0 (11-Ch)	0.0136453	0.0818636	0.0949267	0.0414701
CUORE-0 (22-Ch)	-0.0669917	-0.00927506	0.00177706	0.0350861

5.6 Axion search results

The expected number axioelectric of absorption events is given by:

$$counts = \epsilon \; N \; t \; \Phi_a \; \sigma_{ae}, \tag{5.1}$$

where ϵ is the efficiency of the detector, N is the number of target nuclei, t is the live time of the experiment, Φ_a is the solar axion flux, and σ_{ae} is the axioelectric absorption cross section. The detector efficiency for CUORE-TeO_2 bolometers is $\epsilon \simeq 1$. Since each experiment considered deals with the same detector material (TeO_2) it is advantageous to express the product of the target nuclei and live time in terms of the number of target nuclei per kg, n, and experimental exposure, η, in $kg \cdot d$. In this way the target nuclei per kg is the same for all TeO_2 detectors and only the exposure changes depending on the experiment being analyzed. Making the substitution, $N \cdot t = n \cdot \eta$, equation 5.1 becomes:

$$counts = \epsilon \; n \; \eta \; \Phi_a \; \sigma_{ae}. \tag{5.2}$$

The flux at 6.4 keV due to ABC reactions was specifically calculated for this analysis by Javier Redondo [66] and is given in equation 5.3. The 14.4 keV solar axion flux, of relativistic axions, from the M1 transition of ^{57}Fe was given by the CAST collaboration [19], and is given in equation 5.4.

$$\begin{aligned} \phi_a(6.4\ keV) &= g_{ae}^2 \left(4.7 \times 10^{33}\ cm^{-2} s^{-1}\right) \\ &= g_{ae}^2 \left(4.06 \times 10^{38}\ cm^{-2} d^{-1}\right) \end{aligned} \tag{5.3}$$

$$\begin{aligned}\phi_a(14.4\ keV) &= \left(g_{aN}^{eff}\right)^2 (4.56 \times 10^{23}\ cm^{-2}s^{-1}) \\ &= \left(g_{aN}^{eff}\right)^2 (3.94 \times 10^{28}\ cm^{-2}d^{-1}) \end{aligned} \tag{5.4}$$

In this section, the axioelectric absorption cross section of TeO_2 is calculated using equation 4.24 for relativistic solar axions with an energy of 6.4 keV and 14.4 keV respectively. For relativistic axions with energies of 6.4 keV and 14.4 keV interacting with a TeO_2 detector via the axioelectric effect, the absorption cross sections are:

$$\sigma_{ae}(6.4\ keV) = g_{ae}^2\ (8.55 \times 10^{-4})\ \sigma_{pe}(6.4\ keV) \tag{5.5}$$

$$\sigma_{ae}(14.4\ keV) = g_{ae}^2\ (4.33 \times 10^{-3})\ \sigma_{pe}(14.4\ keV) \tag{5.6}$$

At the energy of 6.4 keV, the photo-electric cross section of tellurium is 493.868622 cm^2g^{-1} and the cross section of oxygen is 21.6770248 cm^2g^{-1}. The photo-electric cross section of tellurium, at an energy of 14.4 keV, is 55.3361 $cm^2\ g^{-1}$ and the cross section of oxygen is 1.6252 $cm^2\ g^{-1}$ [92]. The total photo-electric cross sections of TeO_2 at 6.4 keV and 14.4 keV are therefore 537.223 cm^2g^{-1} and 58.5865 cm^2g^{-1} respectively. Even though the cross section of oxygen is considerably smaller than that of tellurium, at both of the considered energies ($\sim$ 25 and $\sim$ 35 times smaller, respectively), it is included in the cross section calculations for completeness. The cross sections are then converted from units of cm^2g^{-1} to $cm^2\ (TeO_2)^{-1}$, using the molar mass M of TeO_2 (159.6 g/mol) and Avogadro's number N_A ($6.022 \times 10^{23}\ mol^{-1}$).

$$\begin{aligned}\sigma_{pe}(6.4keV) &= 537.223\ cm^2g^{-1}\left(\frac{M}{N_A}\right) \\ &= 1.42 \times 10^{-19} cm^2 (TeO_2)^{-1} \end{aligned} \tag{5.7}$$

$$\begin{aligned}\sigma_{pe}(14.4keV) &= 58.5865\ cm^2g^{-1}\left(\frac{M}{N_A}\right) \\ &= 1.55 \times 10^{-20} cm^2 (TeO_2)^{-1} \end{aligned} \tag{5.8}$$

Inserting the value from equation 5.7 into equation 5.5, and the value from equation 5.8 into equation 5.6, the axioelectric cross section of a TeO_2 molecule, at 6.4 keV

and 14.4 keV respectively, can be expressed in terms of a numerical factor and the axion-electron coupling constant g_{ae}.

$$\sigma_{ae}(6.4keV) = g_{ae}^2(1.22 \times 10^{-22})cm^2(TeO_2)^{-1} \tag{5.9}$$

$$\sigma_{ae}(14.4keV) = g_{ae}^2(6.72 \times 10^{-23})cm^2(TeO_2)^{-1} \tag{5.10}$$

The two remaining values needed are: the number of TeO_2 molecules per kilogram, and the exposure of the experiment being analyzed. The number of TeO_2 nuclei per kilogram is $n = 3.77 \times 10^{24}\ TeO_2\ kg^{-1}$ and the total exposure for each experiment in $kg \cdot d$ is given in table 5.1. At this point we can use the axion rates (per unit mass) to some desired CL, that were established with the Monte Carlo code, in terms of the relevant axion couplings, and in the context of the DFSZ axion model, the PQ symmetry breaking scale and the axion mass. First, the results for the 6.4 keV axion search are discussed followed by those of the 14.4 keV search.

Comparing the expected number of axion absorption events in equation 5.2 to the experimental bound on the actual number of counts, we place upper bounds on axion coupling to normal matter. In particular, from the 6.4 keV axion search, we place an upper bound on the axion-electron coupling (g_{ae}) alone, because both the production and detection methods each involve a factor of the axion-electron coupling squared. By comparing the fourth root of the ratio of the bound on experimental counts to theoretically expected number of counts at 6.4 keV, we place a bound on the axion-electron coupling constant. This equation was used for both CUORICINO and CCVR2, simply by changing the exposure and experimental upper limits of axion candidate events, and by leaving the constants as one numerical value. The upper bound on g_{ae} is then:

$$g_{ae} \leq \left[\frac{counts(CL)}{\epsilon \cdot \eta \times 1.87 \times 10^{41}\ (c \cdot kg^{-1} \cdot d^{-1})}\right]^{1/4}, \tag{5.11}$$

where η represents exposure in $[kg \cdot d]$ and $counts(CL)$ is the maximum experimental number of candidate events at a the desired CL. Using equation (5.11), bounds on

the axion-electron coupling constant were derived from CCVR2, CUORICINO, and the combined CCVR2 and CUORICINO data.

Table 5.8: Experimental bounds on the axion-electron coupling constant (ϵ =1).

Data set	$g_{ae}(90\%CL) \leq$	$g_{ae}(95\%CL) \leq$
CCVR2	$5.20\times\ 10^{-11}$	$5.32\times\ 10^{-11}$
CUORICINO	$2.73\times\ 10^{-11}$	$3.10\times\ 10^{-11}$
Combined	$3.80\times\ 10^{-11}$	$3.95\times\ 10^{-11}$

The upper limit on the 6.4 keV axion rate can also be used to derive a bound on the PQ-scale, f_a (equation 5.12), or the axion mass m_a (equation 5.13). These bounds are considered in the DFSZ invisible axion model for S = 0.5 and z = 0.56.

$$f_a \geq \left[\frac{\epsilon \cdot \eta \times 1.56 \times 10^{26}\ (c \cdot kg^{-1} \cdot d^{-1})}{counts(CL)}\right]^{1/4}\ GeV \tag{5.12}$$

$$m_a \leq \left[\frac{9.4 \times counts(CL)}{\epsilon \cdot \eta\ (c \cdot kg^{-1} \cdot d^{-1})}\right]^{1/4}\ eV \tag{5.13}$$

The CUORICINO spectrum yields the best upper bound on g_{ae}, and therefore also gives the best bounds on f_a (table 5.9) and m_a (table 5.10). To avoid rounding errors in obtaining the numerical factor in eq 5.12, the bound on f_a was computed directly using the bound on the axion electron coupling constant:

$$g_{ae} \equiv \frac{m_e(GeV)}{3 \cdot f_a} = \frac{1.7 \times 10^{-4}\ GeV}{f_a}. \tag{5.14}$$

The conversion between the PQ symmetry breaking scale and the axion mass is straightforward (equation 4.3).

Table 5.9: Experimental bounds on the PQ-scale (f_a [GeV]) from the 6.4 keV axion rates (ϵ =1).

Data set	$f_a(90\%CL)$[GeV] $\geq$	$f_a(95\%CL)$[GeV] $\geq$
CCVR2	$3.27\ \times 10^6$	$3.20\ \times 10^6$
CUORICINO	$6.23\ \times\ 10^6$	$5.48\times\ 10^6$
Combined	$4.47\times\ 10^6$	$4.30\times\ 10^6$

Table 5.10: Experimental bounds on the axion mass (m_a [eV]) from the 6.4 keV axion rates (ϵ =1).

Data set	$m_a(90\%CL)$[eV] $\leq$	m_a[eV](95%CL) $\leq$
CCVR2	1.83	1.88
CUORICINO	0.963	1.09
Combined	1.34	1.40

For the 14.4 keV solar axion search from the M1 transition of ^{57}Fe, the axion is produced via a nuclear process which involves the square of an effective axion-nucleon coupling constant. The detection method also relies on the axio-electric effect, so there is also a factor of the square of the axion-electron coupling constant. By comparing the expected ratio of the number of candidate events at 14.4 keV, to the experimental upper limit (at some confidence level), we are able to place an experimental bound on the product of the axion-electron coupling and the effective axion-nucleon coupling $|g_{ae} \times g_{aN}^{eff}|$:

$$|g_{ae} \times g_{aN}^{eff}| \leq \left[\frac{counts(CL)}{\epsilon \cdot \eta \times 9.98 \times 10^{30}\ (c \cdot kg^{-1} \cdot d^{-1})}\right]^{1/2}. \tag{5.15}$$

This is the general formula that we apply to various experimental data sets to obtain a bound, where the number of experimental counts and exposure differ. In some cases, the detector efficiencies may also vary, but for the following results the value $\epsilon = 1$ is assumed.

Table 5.11: Experimental bounds on the product of the effective axion-nucleon and axion-electron coupling by experiment (ϵ =1).

Data set	$\lvert g_{ae} \times g_{aN}^{eff} \rvert$ (90%CL) $\leq$	$\lvert g_{ae} \times g_{aN}^{eff} \rvert$ (95%CL) $\leq$
CCVR2	1.99×10^{-16}	2.23×10^{-16}
CUORICINO	1.54×10^{-16}	1.71×10^{-16}
Combined	1.60×10^{-16}	1.74×10^{-16}
CUORE-0 (11-Ch)	9.06×10^{-17}	9.75×10^{-17}
CUORE-0 (22-Ch)		1.33×10^{-17}

The upper limit on the 14.4 keV axion rate can be used to derive a bound on the

PQ-scale f_a (eq 5.16) or on the axion mass m_a (eq 5.17).

$$f_a \geq \left[\frac{\epsilon \cdot \eta \times 5.35 \times 10^{21}\ (c \cdot kg^{-1} \cdot d^{-1})}{counts(CL)}\right]^{1/4}\ GeV \tag{5.16}$$

$$m_a \leq \left[\frac{2.77 \times 10^5 \times counts(CL)}{\epsilon \cdot \eta\ (c \cdot kg^{-1} \cdot d^{-1})}\right]^{1/4}\ eV \tag{5.17}$$

Again, to avoid rounding errors in obtaining the numerical factor in eq 5.16, the bound on f_a was computed directly by using the bound on the product of the axion-electron and effective axion-nucleon coupling constants:

$$f_a \geq \left[\frac{2.31 \times 10^{-5}}{|g_{ae} \times g_{aN}^{eff}|}\right]^{1/2}\ GeV \tag{5.18}$$

Table 5.12: Experimental bounds on the PQ-scale (f_a [GeV]) from the 14.4 keV axion rate (ϵ =1).

Data set	$f_a(90\%CL)$[GeV] $\geq$	$f_a(95\%CL)$[GeV] $\geq$
CCVR2	3.41 $\times 10^5$	3.22 $\times 10^5$
CUORICINO	3.87 $\times$ 10^5	3.68$\times$ 10^5
Combined	3.80 $\times$ 10^5	3.64$\times$ 10^5
CUORE-0 (11-Ch)	5.05 $\times$ 10^5	4.87 $\times$ 10^5
CUORE-0 (22-Ch)		1.31 $\times$ 10^6

Table 5.13: Experimental bounds on the axion mass (m_a [eV]) from the 14.4 keV axion rate (ϵ =1).

Data set	$m_a(90\%CL)$[eV] $\leq$	m_a[eV]$(95\%CL)$ $\leq$
CCVR2	17.6	18.6
CUORICINO	16.0	16.8
Combined	15.8	16.5
CUORE-0 (11-Ch)	11.9	12.3
CUORE-0 (22-Ch)		4.58

5.7 Projection to CUORE

To determine the sensitivity that CUORE would have to observe an axion signal at 6.4keV the null result of the axion search was projected to the scale of CUORE

after five years of live time using the CUORICINO data set. Since the CUORE-0 threshold is above 6.4 keV, a conservative estimate is made with CUORICINO data. The assumed exposures for CUORE at 6.4 keV is that half of the total 988 TeO_2 bolometers (494) would have energy thresholds of 5 keV or lower. Additionally, the scaled CUORE spectra are reduced by an additional factor, defined as the ratio of the expected CUORE background in the $0\nu\beta\beta$ decay ROI, to the measured background in the $0\nu\beta\beta$ decay ROI for CUORICINO. The expected DBD background for CUORE is 0.01 c/kg/y/keV, and the DBD background for CUORICINO was 0.2 c/kg/y/keV.

For the projected 6.4 keV solar axion search with CUORE, an upper limit of 8.02×10^{-4} $c/kg/d$ was determined at 90 % CL. This translates in to an upper bound of $g_{ae} \leq 8.09 \times 10^{-12}$ (90% CL) for the axion-electron coupling constant, and a lower bound of $f_a \geq 2.10 \times 10^7$ GeV (90% CL) for the axion decay constant in the DFSZ axion model. As mentioned previously, a value of S = 0.5 was used for the flavor-singlet axial vector matrix element. A summary of the results is given in table 5.14.

Table 5.14: Projected sensitivity of CUORE to observe 6.4 keV solar axions from the results of CUORICINO

	90% CL	95% CL
Rate $[c/kg/d] \leq$	8.02063×10^{-4}	9.55973×10^{-4}
$g_{ae} \leq$	8.09×10^{-12}	8.46×10^{-12}
$f_a\ [GeV] \geq$	2.1×10^7	2.01×10^7
$m_a\ [eV] \leq$	0.286	0.299

Fake events were added to the scaled up CUORE background spectra in the axion-energy region of interest. These events were smeared by a gaussian distribution about the axion energy with the established detector energy resolution of the experiment. The background spectra of the CUORICINO experiment, scaled to CUORE, with fake axion signal corresponding to an assumed value of f_a are shown in figure 5.30. The projected spectrum with no events added is also shown, for a side-by-side comparison.

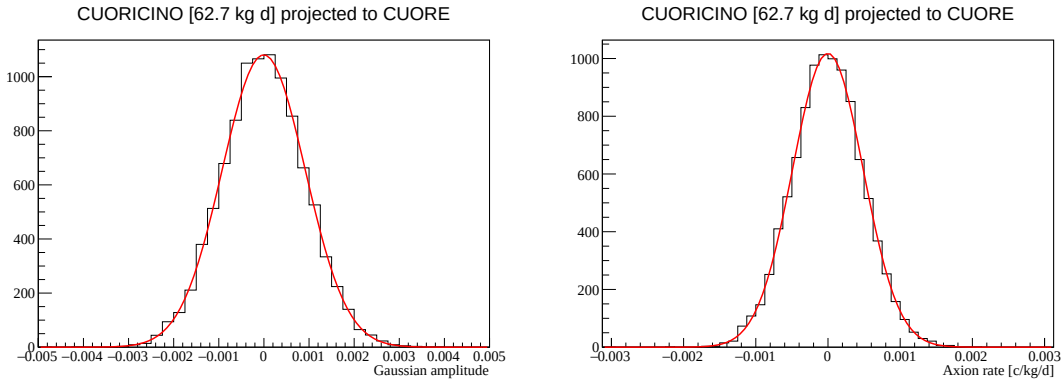

(a) Amplitude (b) Rate

Figure 5.29: Monte Carlo likelihood function of the 6.4 keV axion amplitude and rate [c/d/kg] for CUORE-0 projected to CUORE.

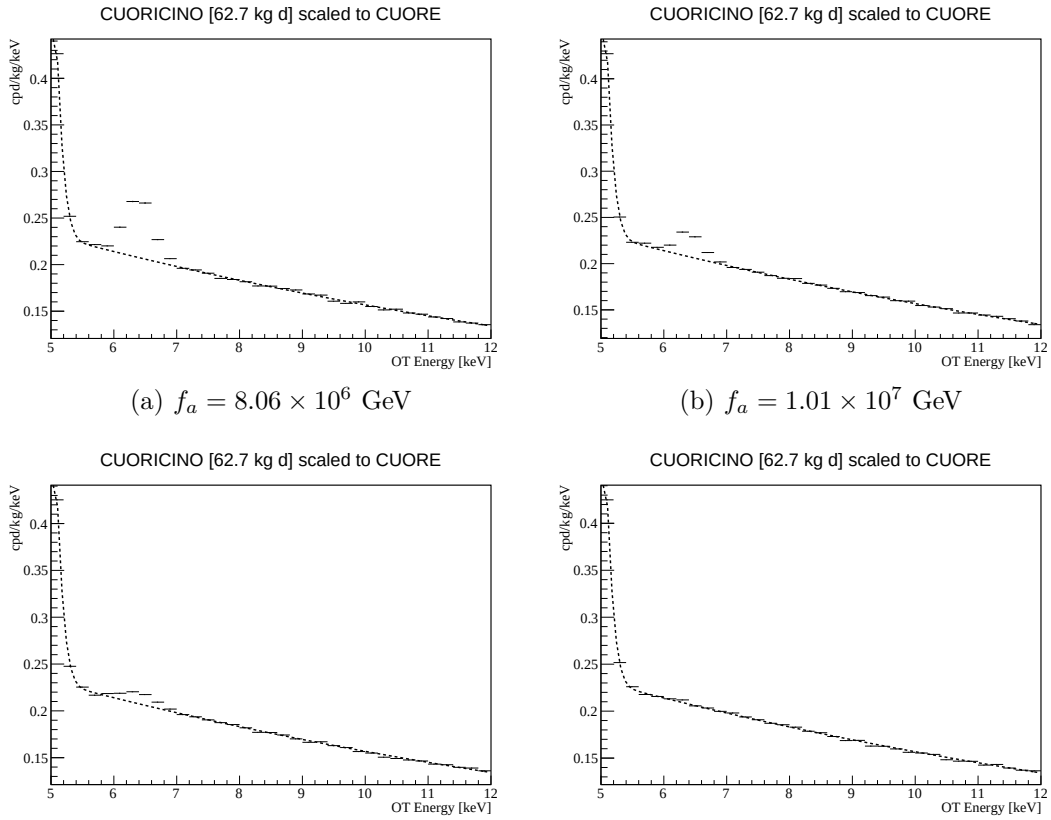

(a) $f_a = 8.06 \times 10^6$ GeV (b) $f_a = 1.01 \times 10^7$ GeV

(c) $f_a = 1.21 \times 10^7$ GeV (d) No seeded events

Figure 5.30: Random CUORICINO background spectra scaled to CUORE, with fake axion signal corresponding to an assumed value of f_a. The projected spectrum with no events is also shown.

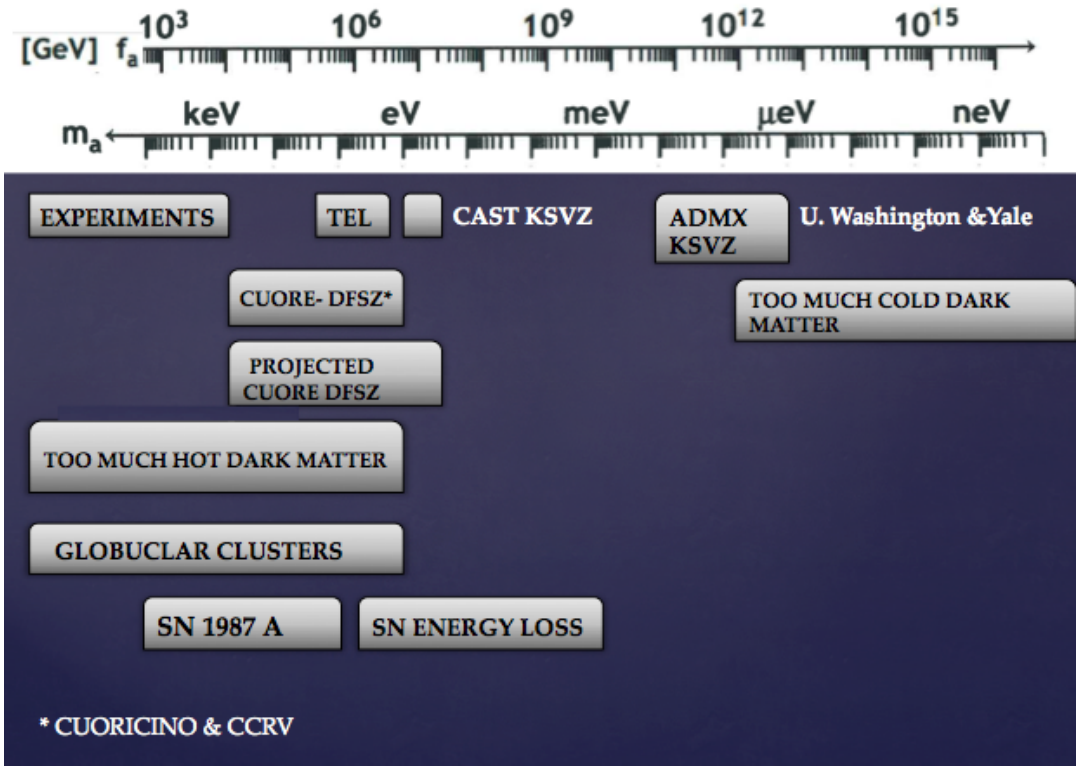

Figure 5.31: Limits on axion mass and decay constant of this work (in the DFSZ axion model) and the projection to CUORE.

To put the final results of the axion search in perspective, results from other experiments are given below in terms of f_a:

- The previously published analysis of the CCVR2 experiment [13] gives an upper bound for the 14.4 keV axion rate as ≤ 0.58 c/d/kg (95% CL). In the DFSZ axion model, the PQ symmetry breaking scale bound is then $f_a \geq 3.12 \times 10^5$ GeV (95% CL), corresponding to an axion mass of $m_a \leq 19.2$ eV. These bounds are comparable to the bounds on CCVR2 from the present analysis.

- The CAST collaboration also considered the product of the axion-electron and axion photon couplings [40], from bremsstrahlung, Compton scattering, and axio-recombination (ABC) processes. This resulted in a bound of $|g_{a\gamma} \times g_{ae}| \leq 8.1 \times 10^{-23}$ GeV^{-1} at a 95% CL. In DFSZ axion model this corresponds to $f_a \geq 4.16 \times 10^7$ GeV (95% CL).

- The EDELWEISS-II [24] bound on the axion-electron coupling constant is $g_{ae} \leq 2.56 \times 10^{-11}$ (95% CL), which corresponds to a $f_a \geq 6.64 \times 10^6$ GeV at a 95% CL (DFSZ).

- The best bound on the axion decay constant (DFSZ model), from this present analysis, is obtained with the CUORICINO experiment; $f_a \geq 5.48 \times 10^6$ GeV at a 95% CL (DFSZ).

Experimental results in terms of axion coupling constants:

- Edelweiss: $g_{ae} \leq 2.56 \times 10^{-11}$ (95% CL)
- Edelweiss: $|g_{a\gamma} \times g_{ae}| \leq 4.70 \times 10^{-17}$ (95% CL)
- CUORICINO: $g_{ae} \leq 3.1 \times 10^{-11}$ (95% CL)
- CUORE-0: $|g_{a\gamma} \times g_{ae}| \leq 6.75 \times 10^{-18}$ (95% CL)
- XMASS: $g_{ae} \leq 5.40 \times 10^{-11}$ (90% CL)
- XENON100: $g_{ae} \leq 7.7 \times 10^{-12}$ (90% CL)
- CUORE projection: $g_{ae} \leq 8.5 \times 10^{-12}$ (95% CL)

5.8 Conclusion

In this dissertation we report on the first search for solar axions from atomic transitions in the solar core. In addition, a search for the 14.4 keV axion from the ground state transition in ^{57}Fe in the sun was also performed using the axioelectric effect in TeO_2 bolometers in the CUORE-0 experiment. Both axion searches are performed in the scope of the DSFZ invisible-axion model. The detectors are $5\times5\times5$ cm^3 crystals operated at about 10 mK at the Laboratori Nazionali del Gran Sasso in Assergi, Italy. Analyses of CCVR2, CUORICINO and CUORE-0 data were preformed using a low

energy trigger, optimized to reduce the energy threshold of the detector. For the search of the 6.4 keV axion, from the atomic K-shell transition in Fe, an upper limit of $1.72\times10^{-1}\ c\cdot kg^{-1}\cdot d^{-1}$ is established at 95% C.L. with the CUORICINO data, which translates into lower bounds $f_a \geq 5.48\times10^6$ GeV 95% C.L. (DFSZ model) on the Peccei-Quinn symmetry-breaking scale, for a value of S = 0.5 for the flavor-singlet axial vector matrix element. This bound can be expressed in terms of axion mass as $m_a \leq 1.09$ eV at 95% C.L. (DFSZ).

For the search of the 14.4 keV axion, from the M1 transition of thermally excited ^{57}Fe in the solar core, an upper limit of $9.49\times10^{-2}\ c\cdot kg^{-1}\cdot d^{-1}$ is established at 95% C.L., with the 11-channel CUORE-0 data, which translates into lower bounds $f_a \geq 4.87\times10^5$ GeV 95% C.L. (DFSZ) on the Peccei-Quinn symmetry-breaking scale, for a value of S = 0.5 of the flavor-singlet axial vector matrix element. Again, this bound can be expressed in terms of axion mass as $m_a \leq 12.3$ eV at 95% C.L. (DFSZ). When considering the 22-channel CUORE-0 data a lower bound of $f_a \geq 1.31\times10^6$ GeV 95% C.L. (DFSZ) on the Peccei-Quinn symmetry-breaking scale, is established. This bound can be expressed in terms of axion mass as $m_a \leq 4.58$ eV at 95% C.L. (DFSZ).

Regardless of which of the two CUORE-0 data sets are considered the CUORICINO bound on the 6.4 keV axion rate gives a much stronger constraint since it relies on only one axion coupling constant. For the CUORE experiment, it is imperative that every effort is made to reduce the detector low-energy threshold to allow for a 6.4 keV axion search. Conservative projections of the CUORE sensitivity, from CUORICINO, gives $f_a \geq 2.01\times10^7$ GeV in the DFSZ axion model (95% CL).

Bibliography

[1] C. E. Aalseth, F. T. Avignone, et al. "IGEX ^{76}Ge neutrinoless double-beta decay experiment: Prospects for next generation experiments". In: *Phys. Rev. D* 65 (2002), p. 092007.

[2] C. E. Aalseth et al. "Comment on "Evidence for neutrinoless double beta decay"". In: *Mod. Phys. Lett. A* 17 (2002), p. 1475.

[3] A. I. Abazov et al. "Search for neutrinos from sun using the reaction $^{71}\mathrm{Ga}(\nu_e, e^-)^{71}\mathrm{Ge}$". In: *Phys. Rev. Lett.* 67 (1991), p. 3332.

[4] L.F. Abbott and P. Sikivie. "A cosmological bound on the invisible axion". In: *Physics Letters B* 120 (1983), p. 133.

[5] M. Agostini et al. "Results on Neutrinoless Double-β Decay of ^{76}Ge from Phase I of the GERDA Experiment". In: *Phys. Rev. Lett.* 111 (2013), p. 122503.

[6] Q. R. Ahmad et al. "Measurement of the Rate of $\nu_e + d \rightarrow p + p + e^-$ Interactions Produced by ^8B Solar Neutrinos at the Sudbury Neutrino Observatory". In: *Phys. Rev. Lett.* 87 (2001), p. 071301.

[7] J. B. Albert et al. "Search for Majorana neutrinos with the first two years of EXO-200 data". In: *Nature* 510 (2014), p. 299.

[8] C. Alduino et al. "Analysis techniques for the evaluation of the neutrinoless double-β decay lifetime in ^{130}Te with the CUORE-0 detector". In: *Phys. Rev. C* 93 (2016), p. 045503.

[9] A. Alessandrello. "A search for neutrinoless double beta decay of ^{130}Te with a thermal detector". In: *Physics Letters B* 285 (1992), p. 176.

[10] A. Alessandrello et al. "A new search for neutrinoless $\beta\beta$ decay with a thermal detector". In: *Physics Letters B* 335 (1994), p. 519.

[11] A. Alessandrello et al. "Improvements in 130Te double beta decay search with cryogenic TeO2 array detectors". In: *Nuclear Physics B - Proceedings Supplements* 48 (1996), p. 238.

[12] F. Alessandria et al. “CUORE crystal validation runs: Results on radioactive contamination and extrapolation to CUORE background”. In: *Astroparticle Physics* 35 (2012), p. 839.

[13] F. Alessandria et al. “Search for 14.4 keV solar axions from M1 transition of ^{57}Fe with CUORE crystals”. In: *JCAP* 1305 (2013), p. 007.

[14] F. Alessandria et al. “Sensitivity of CUORE to Neutrinoless Double-Beta Decay”. In: (2011). arXiv: `1109.0494 [nucl-ex]`.

[15] F. Alessandria et al. “Validation of techniques to mitigate copper surface contamination in CUORE”. In: *Astroparticle Physics* 45 (2013), p. 13.

[16] K. Alfonso et al. “Search for Neutrinoless Double-Beta Decay of ^{130}Te with CUORE-0”. In: *Phys. Rev. Lett.* 115 (2015), p. 102502.

[17] E. Andreotti et al. “^{130}Te neutrinoless double-beta decay with CUORICINO”. In: *Astroparticle Physics* 34 (2011), p. 822.

[18] E. Andreotti et al. “The low radioactivity link of the CUORE experiment”. In: *Journal of Instrumentation* 4 (2009), P09003.

[19] S. Andriamonje et al. “Search for 14.4-keV solar axions emitted in the M1-transition of ^{57}Fe nuclei with CAST”. In: *JCAP* 0912 (2009), p. 002.

[20] P. Anselmann et al. “Solar neutrinos observed by GALLEX at Gran Sasso.” In: *Physics Letters B* 285 (1992), pp. 376–389.

[21] M. Apollonio et al. “Limits on neutrino oscillations from the CHOOZ experiment”. In: *Physics Letters B* 466 (1999), p. 415.

[22] T. Araki et al. “Measurement of Neutrino Oscillation with KamLAND: Evidence of Spectral Distortion”. In: *Phys. Rev. Lett.* 94 (2005), p. 081801.

[23] R. Ardito et al. “CUORE: A Cryogenic underground observatory for rare events”. In: (2005). arXiv: `hep-ex/0501010 [hep-ex]`.

[24] E. Armengaud et al. “Axion searches with the EDELWEISS-II experiment”. In: *JCAP* 1311 (2013), p. 067.

[25] C. Arnaboldi, G. Pessina, and E. Previtali. “A programmable calibrating pulse generator with multi-outputs and very high stability”. In: *IEEE Transactions on Nuclear Science* 50 (2003), p. 979.

[26] C. Arnaboldi et al. “A programmable multichannel antialiasing filter for the CUORE experiment”. In: *Nuclear Instruments and Methods in Physics Research Section A: Accelerators, Spectrometers, Detectors and Associated Equipment* 617 (2010), p. 327.

[27] C. Arnaboldi et al. “Production of high purity TeO_2 single crystals for the study of neutrinoless double beta decay”. In: *Journal of Crystal Growth* 312 (2010), p. 2999.

[28] C. Arnaboldi et al. “Results from a search for the $0\nu\beta\beta$-decay of ^{130}Te”. In: *Phys. Rev. C* 78 (2008), p. 035502.

[29] C. Arnaboldi et al. “The front-end readout for CUORICINO, an array of macro-bolometers and MIBETA, an array of μ-bolometers”. In: *Nuclear Instruments and Methods in Physics Research Section A: Accelerators, Spectrometers, Detectors and Associated Equipment* 520 (2004), p. 578.

[30] C. Arnaboldi et al. “The programmable front-end system for CUORICINO, an array of large-mass bolometers”. In: *IEEE Transactions on Nuclear Science* 49 (2002), p. 2440.

[31] D. R. Artusa et al. “Initial performance of the CUORE-0 experiment”. In: *The European Physical Journal C* 74 (2014), p. 2956.

[32] K. Asakura et al. “Search for double-beta decay of 136Xe to excited states of 136Ba with the KamLAND-Zen experiment”. In: *Nuclear Physics A* 946 (2016), p. 171.

[33] M. Auger et al. “Search for Neutrinoless Double-Beta Decay in ^{136}Xe with EXO-200”. In: *Phys. Rev. Lett.* 109 (2012), p. 032505.

[34] S. Aune et al. “Solar axion search with the CAST experiment”. In: *Proceedings, 34th International Conference on High Energy Physics (ICHEP 2008): Philadelphia, Pennsylvania, July 30-August 5, 2008*. 2008.

[35] F. T. Avignone III et al. “Search for axions from the 1115-keV transition of ^{65}Cu”. In: *Phys. Rev. D* 37 (1988), p. 618.

[36] *Axio-electric effect*. URL: `http://www.ph.ed.ac.uk/sites/default/files/legacy/axio-electric.jpg`.

[37] C. A. Baker et al. “Improved Experimental Limit on the Electric Dipole Moment of the Neutron”. In: *Phys. Rev. Lett.* 97 (2006), p. 131801.

[38] J. Barea, J. Kotila, and F. Iachello. "Nuclear matrix elements for double-β decay". In: *Phys. Rev. C* 87 (2013), p. 014315.

[39] V. Barger, Danny Marfatia, and Adam Tregre. "Neutrino mass limits from SDSS, 2dFGRS and WMAP". In: *Physics Letters B* 595 (2004), p. 55.

[40] K. Barth et al. "CAST constraints on the axion-electron coupling". In: *JCAP* 1305 (2013), p. 010.

[41] L. Baudis et al. "Limits on the Majorana Neutrino Mass in the 0.1 eV Range". In: *Phys. Rev. Lett.* 83 (1999), p. 41.

[42] A. I. Belesev et al. "The search for an additional neutrino mass eigenstate in the 2-100 eV region from 'ĂŸTroitsk nu-mass'ĂŹ data: a detailed analysis". In: *Journal of Physics G: Nuclear and Particle Physics* 41 (2014), p. 015001.

[43] C. L. Bennett et al. "The Microwave Anisotropy Probe Mission". In: *The Astrophysical Journal* 583 (2003), p. 1.

[44] *Beta Decay*. URL: `https://en.wikipedia.org/wiki/Beta_Decay`.

[45] *Beta Decay*. URL: `https://kjende.web.cern.ch/kjende/en/betadecay.htm`.

[46] F. Boehm et al. "Final results from the Palo Verde neutrino oscillation experiment". In: *Phys. Rev. D* 64 (2001), p. 112001.

[47] C. Brofferio et al. "Electrical characterization of the low background Cu-PEN links of the CUORE experiment". In: *Nuclear Instruments and Methods in Physics Research Section A: Accelerators, Spectrometers, Detectors and Associated Equipment* 718 (2013), p. 211.

[48] Jr. C. L. Cowan and F. Reines. "The Neutrino". In: *Nature* 178 (1956), p. 446.

[49] Jr. C. L. Cowan et al. "Detection of the Free Neutrino: A Confirmation". In: *Science* 124 (1956), p. 103.

[50] Matthew Colless et al. "The 2dF Galaxy Redshift Survey: spectra and redshifts". In: *Monthly Notices of the Royal Astronomical Society* 328 (2001), p. 1039.

[51] Raymond Davis. "Solar Neutrinos. II. Experimental". In: *Phys. Rev. Lett.* 12 (1964), pp. 303–305.

[52] R.L. Davis. “Cosmic axions from cosmic strings”. In: *Physics Letters B* 180 (1986), p. 225.

[53] A. V. Derbin et al. “Constraints on the axion-electron coupling constant for solar axions appearing owing to bremsstrahlung and the compton process”. In: *JETP Letters* 95 (2012), pp. 339–344.

[54] A. V. Derbin et al. “Constraints on the axion-electron coupling for solar axions produced by a Compton process and bremsstrahlung”. In: *Phys. Rev. D* 83 (2011), p. 023505.

[55] S. Di Domizio, F. Orio, and M. Vignati. “Lowering the energy threshold of large-mass bolometric detectors”. In: *Journal of Instrumentation* 6 (2011), P02007.

[56] Michael Dine and Willy Fischler. “The not-so-harmless axion”. In: *Physics Letters B* 120 (1983), p. 137.

[57] Michael Dine, Willy Fischler, and Mark Srednicki. “A simple solution to the strong CP problem with a harmless axion”. In: *Physics Letters B* 104 (1981), p. 199.

[58] G. Drexlin et al. “Current direct neutrino mass experiments”. In: *Advances in High Energy Physics* 2013 (2013), p. 293986.

[59] K. Eguchi et al. “First Results from KamLAND: Evidence for Reactor Antineutrino Disappearance”. In: *Phys. Rev. Lett.* 90 (2003), p. 021802.

[60] K. Eguchi et al. “High Sensitivity Search for $\overline{\nu}_e$’s from the Sun and Other Sources at KamLAND”. In: *Phys. Rev. Lett.* 92 (2004), p. 071301.

[61] Amand Faessler, Vadim Rodin, and Fedor Šimkovic. “Nuclear matrix elements for neutrinoless double-beta decay and double-electron capture”. In: *Journal of Physics G: Nuclear and Particle Physics* 39 (2012), p. 124006.

[62] Dong-Liang Fang et al. “Neutrinoless double-β decay of deformed nuclei within quasiparticle random-phase approximation with a realistic interaction”. In: *Phys. Rev. C* 83 (2011), p. 034320.

[63] Manuela A Fehr, Mark Rehkämper, and Alex N Halliday. “Application of MC-ICPMS to the precise determination of tellurium isotope compositions in chondrites, iron meteorites and sulfides”. In: *International Journal of Mass Spectrometry* 232 (2004), p. 83.

[64] Ferruccio Feruglio, Alessandro Strumia, and Francesco Vissani. "Neutrino oscillations and signals in β and $0\nu2\beta$ experiments". In: *Nuclear Physics B* 637 (2002), p. 345.

[65] E. Fiorini and T.O. Niinikoski. "Low-temperature calorimetry for rare decays". In: *Nuclear Instruments and Methods in Physics Research* 224 (1984), p. 83.

[66] Javier Redondo to Frank Avignone. Private Communication.

[67] Y. Fukuda et al. "Evidence for Oscillation of Atmospheric Neutrinos". In: *Phys. Rev. Lett.* 81 (1998), pp. 1562–1567.

[68] W. H. Furry. "On Transition Probabilities in Double Beta-Disintegration". In: *Phys. Rev.* 56 (1939), p. 1184.

[69] A. Gando et al. "Limit on Neutrinoless $\beta\beta$ Decay of ^{136}Xe from the First Phase of KamLAND-Zen and Comparison with the Positive Claim in ^{76}Ge". In: *Phys. Rev. Lett.* 110 (2013), p. 062502.

[70] A. Gando et al. "Search for Majorana Neutrinos Near the Inverted Mass Hierarchy Region with KamLAND-Zen". In: *Phys. Rev. Lett.* 117 (2016), p. 082503.

[71] E. Gatti and P. F. Manfredi. "Processing the signals from solid-state detectors in elementary-particle physics". In: *La Rivista del Nuovo Cimento (1978-1999)* 9 (1986), p. 1.

[72] M. Goeppert-Mayer. "Double Beta-Disintegration". In: *Phys. Rev.* 48 (1935), p. 512.

[73] Paolo Gorla. "Optimization of the CUORE detector performance". PhD thesis. Milano, Italia, 2005.

[74] W. C. Haxton and K. Y. Lee. "Red-giant evolution, metallicity, and new bounds on hadronic axions". In: *Phys. Rev. Lett.* 66 (1991), p. 2557.

[75] F T Avignone III, G S King III, and Yu G Zdesenko. "Next generation double-beta decay experiments: metrics for their evaluation". In: *New Journal of Physics* 7.1 (2005), p. 6.

[76] Yoshizumi Inoue et al. "Search for sub-electronvolt solar axions using coherent conversion of axions into photons in magnetic field and gas helium". In: *Physics Letters B* 536 (2002), p. 18.

[77] Igor G Irastorza. *The International Axion Observatory IAXO. Letter of Intent to the CERN SPS committee*. Tech. rep. CERN-SPSC-2013-022. SPSC-I-242. Geneva: CERN, 2013.

[78] David B. Kaplan. "Opening the axion window". In: *Nuclear Physics B* 260 (1985), p. 215.

[79] Jihn E. Kim. "Light pseudoscalars, particle physics and cosmology". In: *Physics Reports* 150 (1987), p. 1.

[80] Jihn E. Kim. "Weak-Interaction Singlet and Strong CP Invariance". In: *Phys. Rev. Lett.* 43 (1979), p. 103.

[81] H. V. Klapdor-Kleingrothaus and I. V. Krivosheina. "The evidence for the observation of $0\nu\beta\beta$ decay: The identification of $0\nu\beta\beta$ events from the full spectra". In: *Mod. Phys. Lett. A* 21 (2006), p. 1547.

[82] H. V. Klapdor-Kleingrothaus et al. "Evidence for neutrinoless double beta decay". In: *Mod. Phys. Lett. A* 16 (2001), p. 2409.

[83] H.V. Klapdor-Kleingrothaus et al. "Data acquisition and analysis of the ^{76}Ge double beta experiment in Gran Sasso 1990-ĂŞ2003". In: *Nuclear Instruments and Methods in Physics Research Section A: Accelerators, Spectrometers, Detectors and Associated Equipment* 522 (2004), p. 371.

[84] H.V Klapdor-Kleingrothaus et al. "Search for neutrinoless double beta decay with enriched ^{76}Ge in Gran Sasso 1990-2003". In: *Physics Letters B* 586 (2004), p. 198.

[85] J. Kotila and F. Iachello. "Phase-space factors for double-β decay". In: *Phys. Rev. C* 85 (2012), p. 034316.

[86] Ch. Kraus et al. "Final results from phase II of the Mainz neutrino mass search in tritium beta decay". In: *The European Physical Journal C* 40 (2005), p. 447.

[87] D. M. Lazarus et al. "Search for solar axions". In: *Phys. Rev. Lett.* 69 (1992), p. 2333.

[88] Ettore Majorana. "Teoria simmetrica dell'elettrone e del positrone". In: *Il Nuovo Cimento (1924-1942)* 14 (1937), p. 171.

[89] L. Meitner and W. Orthmann. "*Ü*ber eine absolute Bestimmung der Energie der prim*ä*ren /*beta*-Strahlen von Radium E". In: 60 (1930), p. 143.

[90] J. Menendez et al. “Disassembling the nuclear matrix Elements of the neutrinoless $\beta\beta$ decay”. In: *Nuclear Physics A* 818 (2009), p. 139.

[91] Shigetaka Moriyama et al. “Direct search for solar axions by using strong magnetic field and X-ray detectors”. In: *Physics Letters B* 434 (1998), p. 147.

[92] *Mucal on the web*. URL: `http://www.csrri.iit.edu/mucal.html`.

[93] *Neutron electric dipole moment*. URL: `https://en.wikipedia.org/wiki/Neutron_electric_dipole_moment`.

[94] *Nuclear Decay and Conservation Laws*. URL: `http://philschatz.com/physics-book/contents/m42633.html`.

[95] *Odkrycie neutrina*. URL: `http://www.fuw.edu.pl/~neutrina/neutrino_elektr.html`.

[96] R. D. Peccei and Helen R. Quinn. “Constraints imposed by CP conservation in the presence of pseudoparticles”. In: *Phys. Rev. D* 16 (1977), p. 1791.

[97] R. D. Peccei and Helen R. Quinn. “CP Conservation in the Presence of Pseudoparticles”. In: *Phys. Rev. Lett.* 38 (1977), p. 1440.

[98] S Pirro et al. “Present status of MI-BETA cryogenic experiment and preliminary results for CUORICINO”. In: *Nuclear Instruments and Methods in Physics Research Section A: Accelerators, Spectrometers, Detectors and Associated Equipment* 444 (2000), p. 71.

[99] John Preskill, Mark B. Wise, and Frank Wilczek. “Cosmology of the invisible axion”. In: *Physics Letters B* 120 (1983), p. 127.

[100] H. Primakoff. “Photo-Production of Neutral Mesons in Nuclear Electric Fields and the Mean Life of the Neutral Meson”. In: *Phys. Rev.* 81 (1951), p. 899.

[101] V. Radeka and N. Karlovac. “Least-square-error amplitude measurement of pulse signals in presence of noise”. In: *Nuclear Instruments and Methods* 52 (1967), p. 86.

[102] G G Raffelt. “Axions-motivation, limits and searches”. In: *Journal of Physics A: Mathematical and Theoretical* 40 (2007), p. 6607.

[103] S. Rahaman et al. “Double-beta decay Q values of ^{116}Cd and ^{130}Te”. In: *Physics Letters B* 703 (2011), p. 412.

[104] P. K. Rath et al. "Uncertainties in nuclear transition matrix elements for $\beta^+\beta^+$ and $\varepsilon\beta^+$ modes of neutrinoless positron double-β decay within the projected Hartree-Fock-Bogoliubov model". In: *Phys. Rev. C* 87 (2013), p. 014301.

[105] Javier Redondo. "Solar axion flux from the axion-electron coupling". In: *JCAP* 1312 (2013), p. 008.

[106] Matthew Redshaw et al. "Masses of ^{130}Te and ^{130}Xe and Double-β-Decay Q Value of ^{130}Te". In: *Phys. Rev. Lett.* 102 (2009), p. 212502.

[107] *Research: Neutrinoless Double Beta Decay*. URL: `http://www.ecap.physik.uni-erlangen.de/nexo/research.shtml`.

[108] A. Ringwald. "Axions and Axion-Like Particles". In: *Proceedings, 49th Rencontres de Moriond on Electroweak Interactions and Unified Theories*. 2014, p. 223.

[109] Tomás R. Rodríguez and Gabriel Martínez-Pinedo. "Energy Density Functional Study of Nuclear Matrix Elements for Neutrinoless $\beta\beta$ Decay". In: *Phys. Rev. Lett.* 105 (2010), p. 252503.

[110] N. D. Scielzo et al. "Double-β-decay Q values of ^{130}Te, ^{128}Te, and ^{120}Te". In: *Phys. Rev. C* 80 (2009), p. 025501.

[111] M.A. Shifman, A.I. Vainshtein, and V.I. Zakharov. "Can confinement ensure natural CP invariance of strong interactions?" In: *Nuclear Physics B* 166 (1980), p. 493.

[112] P. Sikivie. "Experimental Tests of the "Invisible" Axion". In: *Phys. Rev. Lett.* 51 (1983), p. 1415.

[113] J. H. Smith, E. M. Purcell, and N. F. Ramsey. "Experimental Limit to the Electric Dipole Moment of the Neutron". In: *Phys. Rev.* 108 (1957), p. 120.

[114] *Spontaneous Decay of Nuclei*. URL: `http://physics-database.group.shef.ac.uk/phy303/phy303-4.html`.

[115] Mark Srednicki. "Axion couplings to matter: (I). CP-conserving parts". In: *Nuclear Physics B* 260 (1985), p. 689.

[116] *Standard Model*. URL: `https://en.wikipedia.org/wiki/standard_model`.

[117] Jouni Suhonen and Osvaldo Civitarese. "Review of the properties of the $0\nu\beta^-\beta^-$ nuclear matrix elements". In: *Journal of Physics G: Nuclear and Particle Physics* 39 (2012), p. 124005.

[118] Max Tegmark et al. “Cosmological parameters from SDSS and WMAP”. In: *Phys. Rev. D* 69 (2004), p. 103501.

[119] Steven Weinberg. “A New Light Boson?” In: *Phys. Rev. Lett.* 40 (1978), p. 223.

[120] F. Wilczek. “Problem of Strong P and T Invariance in the Presence of Instantons”. In: *Phys. Rev. Lett.* 40 (1978), p. 279.

[121] Guang Yang. “Neutrino mass hierarchy determination at reactor antineutrino experiments”. In: *Proceedings, 12th Conference on the Intersections of Particle and Nuclear Physics (CIPANP 2015): Vail, Colorado, USA, May 19-24, 2015*. 2015.

[122] Yu.G Zdesenko, F.A Danevich, and V.I Tretyak. “Has neutrinoless double β decay of ^{76}Ge been really observed?” In: *Physics Letters B* 546 (2002), p. 206.

[123] A. R. Zhitnitsky. “On Possible Suppression of the Axion Hadron Interactions. (In Russian)”. In: *Sov. J. Nucl. Phys.* 31 (1980), p. 260.